Transient heat load studies on tungsten using a pulsed millisecond laser in a high-flux plasma environment

G.G. van Eden

Utrecht University

under supervision of:
Greg De Temmerman (DIFFER)

formal supervisor:
Pedro Zeijlmans van Emmichoven (DIFFER/UU)

August 21, 2013

Universiteit Utrecht

DIFFER
Dutch Institute for
Fundamental Energy Research

Abstract

Gaining control of the lifetime of plasma-facing components in the ITER divertor is of paramount importance to the successful operation of this machine. By their transient nature, Edge-Localised-Modes (ELMs) can be hazardous for the divertor at high pulse numbers. To be able to study the thermal resilience of tungsten (W) under such loads, ELMs have been replicated by exposing targets to pulsed millisecond laser pulses and an ITER-relevant hydrogen plasma simultaneously. Besides, studies of the thermal response of pristine W and targets pre-exposed to deuterium- and helium plasmas to a pulsed laser are conducted.

A reduction of the melting threshold compared with loading to plasma and laser sequentially has been confirmed. The onset of melting on individual grains is observed for loading at a heat load parameter of 32.2 MJ m^{-2} $s^{-1/2}$ and base temperature of 240 °C and at F_{HF} = 25.2 MJ m^{-2} $s^{-1/2}$ at 450 °C where the average peak temperature was well below the melting threshold of tungsten, indicating local reduced heat conductivity of the surface. Finally, a change in ΔT between first and last pulse up to 7% during plasma exposure over the course of 100 pulses is measured. For a sample containing blisters and bubbles in the near surface, the relative change in ΔT was found to 30% at F_{HF} = 15.1 MJ m^{-2} $s^{-1/2}$ and T_{base} = 600 °C. It is expected that plasma presence gives rise to a synergistic effect causing changes in thermal response of the surface during laser loading.

For pristine samples in absence of plasma, a correction for increased absorptivity at 1064 nm due to surface roughening, obtained from ellipsometry measurements, is accounted resulting in significant increase of ΔT with the succession of pulses for heat loads >36.2 MJ m^{-2} $s^{-1/2}$, indicating a local reduction in surface power handling capabilities of the target material.

The average arithmetic roughness parameter was found to change as a function of peak temperature >1100 °C and is only dependent on pulse number above this temperature threshold. Similarly, growth of grains linearly with increasing temperature was evidenced for temperatures >1500 °C and was found to occur even after single ms pulse.

Transient heat loads studies performed on helium-induced W led to the observation that the thickness of the so-called nanofuzz is reduced linearly proportional to the applied heat load. Complete removal of the nanostructures is only observed upon loading at F_{HF} <32.8 MJ m^{-2} $s^{-1/2}$. Due to enhanced absorptivity of the fuzz layer, peak temperatures higher than those on pristine samples are measured. Loading of 10.000 pulses at moderate heat load parameter caused the formation of a dense crack network without the occurrence of melting, still keeping the fuzz largely intact. In general, cracking was absent for targets exhibiting a base temperature above DBTT for all conditions applied.

A reduction of W power handling capabilities with progressing ELM number for certain conditions as obtained in this thesis, could be problematic for ITER since predicting the lifetime of PFCs becomes increasingly complicated.

Contents

1 Introduction **3**
- 1.1 The potential of nuclear fusion . . . 3
- 1.2 Divertor challenges . . . 4
  - 1.2.1 ELM simulations . . . 5
  - 1.2.2 Synergistic effects of transient heat loads and plasma presence . . . 6
- 1.3 Problem statement . . . 6

2 Theory **8**
- 2.1 Properties of tungsten . . . 8
- 2.2 Various temperature regimes . . . 8
- 2.3 Tungsten thermal shock impact resistance . . . 9
- 2.4 Laser induced surface heating . . . 10
- 2.5 Melt layer evolution model . . . 10

3 Experimental setup **11**
- 3.1 Tungsten specifications and sample preparation . . . 11
- 3.2 Magnum-PSI . . . 11
- 3.3 LASAG and laser injection system . . . 13
- 3.4 Diagnostics . . . 14
  - 3.4.1 Thomson scattering . . . 14
  - 3.4.2 Infrared thermography . . . 14
- 3.5 Post mortem analysis methods . . . 15
  - 3.5.1 Scanning electron microscopy . . . 15
  - 3.5.2 Reflectivity measurements . . . 15
  - 3.5.3 Laser profilometry . . . 16

4 Pulsed laser heating **17**
- 4.1 Change of laser energy absorption due to surface roughening . . . 17
- 4.2 Surface morphology . . . 19
  - 4.2.1 SEM results . . . 19
  - 4.2.2 Surface roughening . . . 22
  - 4.2.3 Recrystallization kinetics . . . 25
- 4.3 Power handling . . . 25
- 4.4 Conclusions and discussion . . . 28

5 Laser loading on plasma-exposed samples **30**
- 5.1 Deuterium exposed samples . . . 30
- 5.2 Helium exposed samples . . . 33
  - 5.2.1 Surface morphology . . . 35
  - 5.2.2 Power handling . . . 41
- 5.3 Conclusions and discussion . . . 42

6 Simultaneous hydrogen plasma and pulsed laser exposure **44**
6.1 Surface morphology . . . 45
6.1.1 SEM results . . . 45
6.1.2 Recrystallization kinetics . . . 47
6.2 Power handling - synergistic effects . . . 51
6.3 Conclusions and discussion . . . 53

7 Final conclusion **55**
7.1 Comparison of damage . . . 55
7.2 Implications for ITER . . . 57

8 Outlook **59**
8.1 Change of decay time . . . 59
8.2 Thermal response of low-temperature He-induced W surface . . . 59
8.3 Simultaneous He plasma and laser loading . . . 59
8.4 Synergistic effects . . . 60
8.4.1 Blister/bubble formation . . . 60
8.4.2 Investigating fluence effects . . . 60

A Shallow melting experiments **61**

Chapter 1

Introduction

1.1 The potential of nuclear fusion

Our modern world has become fully dependent on large scale energy availability. Since the 19th century, the planet is kept running by a growing demand for electricity. As we now start to see the depletion of fossil fuels and the destroying consequences of their exploitation, the call for a large-scale sustainable alternative is growing every day. Although being a long and difficult way, nuclear fusion technology could provide an answer to this.

When a gas species is heated, atomic nuclei and their orbiting electrons become separated. This ionized gas is sometimes called the fourth state of matter: plasma. Compressing a hot plasma containing light atoms brings the constituents close enough to fuse which releases large amounts of energy. As stars like our sun produce their energy via nuclear fusion, achieving this on earth on a large time-scale could easily be called the ultimate, inexhaustible solution to our energy problem. However, although the fundamentals of fusion are well understood, the realization of electricity from nuclear fusion is of immense challenge from an engineering perspective. In order to reach ignition, i.e. a conditions in which the generated heat from fusion products is sufficient to maintain the temperature of the plasma against all losses without external power input, the so-called Lawson criterion needs to be met. This is: the product of plasma density (n_e) and confinement time (τ_e) needs to exceed a certain value. In stars, strong gravitational fields give rise to high densities. Those are obviously lacking on earth. A more useful expression further contains the temperature (T), which reads in the case of deuterium-tritium (D-T) reactions: $n_e T \tau_e \geq 10^{21}\, keV s m^{-3}$. Since this triple product is relatively low in the case of D-T reactions, this mixture is favourable in achieving fusion. As can be inferred from the inequality, one needs to maximize confinement time and temperature of the plasma in order to meet the requirements for fusion on our planet.

The best understood fusion devices are torus-shaped magnetic confinement devices called tokamaks. By means of strong magnetic fields, the burning plasma is confined within the vacuum vessel and heated up to 150 million degrees Celsius which cause deuterium and tritium to fuse. The first tokamak that will generate more power than is needed to sustain the plasma is currently under construction: ITER. This experimental device, which is named after its Latin meaning as 'the way', is designed to generate 500 MW of energy from an average input power of 50 MW in relatively long pulses lasting 300-500 seconds [1]. Building ITER is a crucial step in showing the feasibility of fusion as a reliable large-scale energy source. Operation is scheduled from 2020 onwards.

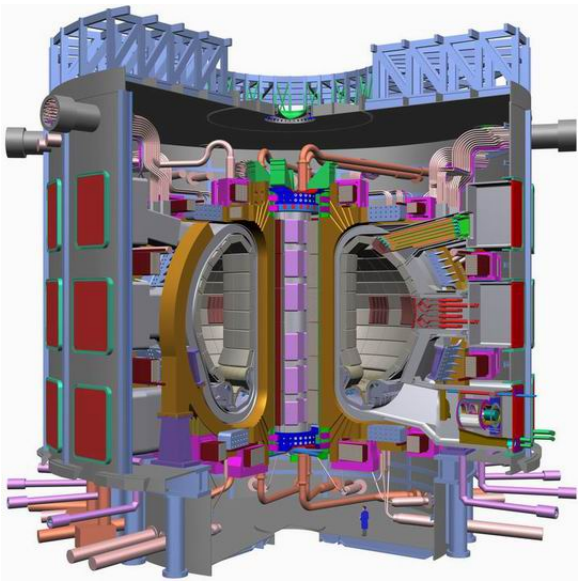

Figure 1.1: Schematic drawing of ITER [1]. A cross-section of the donut-shaped vacuum vessel containing the hot plasma is visible.

1.2 Divertor challenges

Although the hot plasma is detained from the vessel wall through magnetic confinement, fusion products and excess power produced from the plasma have to be exhausted in the divertor region. Being responsible for exhausting waste from the plasma core without releasing impurities into it, whilst being subject to enormous heat- and particle fluxes, this component is one of the most critical elements in ITER. A design sketch of the planned ITER divertor is shown in figure 1.2. The

Figure 1.2: ITER divertor: one of the key components of the ITER machine. Designed to extract heat, reaction products and impurities from the core plasma. This component is located at the lower rim of the vacuum vessel containing the plasma [1].

plasma facing components (PFCs) of the divertor are situated at the intersection of the magnetic field lines that guide high-energy plasma particles from the scrape-off layer towards the exhaust system. The PFC targets are water cooled by means of internal copper-zirconium tubes. Transient heat loads caused by plasma instabilities in a tokamak such as vertical displacement events (VDEs), disruptions and so-called edge localized modes (ELMs) cause strong thermal stresses and enhanced erosion of the divertor PFCs. These transient effects are superimposed on the existing steady state heat load striking the divertor section. This leads to a list of requirements for the materials of choice for this component: excellent thermal conductivity, strength and ductility, thermal shock and thermal fatigue resistance, structural stability at elevated temperatures and stability of those properties under heavy neutron irradiation [2]. Besides, changes in hydrogen retention as a

consequence of damage caused by neutron impact needs to be as low as possible.

Tungsten has been chosen for the PFCs in the ITER divertor because of its high melting point, low tritium retention and low sputtering yield. Although many challenging issues are to be solved, this candidate seems the strongest in fulfilling the list of requirements to serve as the divertor material of choice for ITER. Cycling between various temperature regimes during transients, from brittleness at low temperatures to recrystallization and melting/evaporation at elevated temperatures, is schematically depicted in figure 1.3. Thermal response of tungsten is discussed in more detail in the next section.

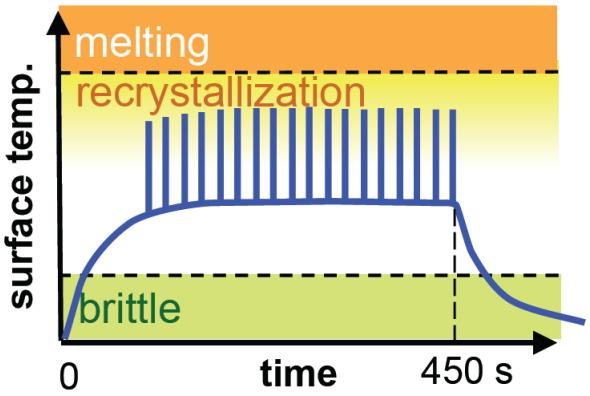

Figure 1.3: Typical operational window of tungsten during ELMs. As a response to thermal loads, tungsten behaves in a brittle way at low temperatures. During each transient, the surface temperature crosses the recrystallization temperature, hereby affecting material properties. For even higher temperatures, transients can lead to melting and even evaporation of the divertor material. *Source: Lecture notes G. De Temmerman.*

1.2.1 ELM simulations

Edge-Localized-Modes (ELMs) and disruptions can lead to unacceptable levels of erosion of the ITER divertor [3] and therefore require thorough understanding of plasma-wall-interactions in this regime. When a tokamak runs in H-mode, a rising pressure gradient that builds up just inside the separatrix is released during the ELM instability and releases energy and particles into the scrape-off-layer in very short timescales (<0.5 ms). Especially the so-called type-I ELMs are of great concern for the ITER divertor because of their transient nature and high energy loss from the core plasma (up to 6% of the stored energy [4]) that is deposited on the divertor in a millisecond timescale. Besides the harsh circumstances, the large number of expected ELMs and their frequency require fatigue-resistant properties for the divertor plates. For each ITER discharge (duration 400 s), ELMs within a frequency range of 1-25 Hz are expected. Before replacement of the divertor armor material, the plates are expected to endure $> 10^6$ ELMs. During such events, the peak power flux on the divertor is in the range of 1-10 GW m^{-2} [5].

During operation in fusion devices, the microstructure of the surface of the PFM layer will be significantly affected. With this, all thermal properties for which tungsten is the material of choice are altered. Focus on resilience of tungsten to the combination of thermal shock loads, thermal fatigue and steady state plasma wall interaction are under strong investigation. As is shown by Loewenhoff et al., tungsten material degradation depends on the number of applied pulses, the power density and the heat load during steady state (surface temperature). It is shown that the lifetime of tungsten PFMs is significantly decreased due to surface cracking under certain combinations of these parameters [6].

Besides, erosion rates of the ITER divertor targets, understanding of melt layer losses and stability is crucial. As the divertor material is in direct contact with the plasma, poor behaviour

limits successful operation of the fusion plasma. Thorough understanding of the divertor surface behaviour under transient heat- and particle loads is therefore of major importance.

Since studies of tungsten target response to ELM loads in the ITER-regime are not yet fully reproducible, several simulation methods are applied to study specific conditions. Examples of these are thermal shock tests in electron beam facility JUDITH, thermal cycling experiments in GLADIS [7], pulsed laser experiments in NAGDIS-II [8] and PISCES-A [9], and plasma guns in QSPAs [10]. Although plasma guns and pulsed plasma systems are capable of replicating ELMs most realistically due to simultaneous particle and heat transfer, pulsed laser and electron guns allow for perfect control over pulse energy, duration and achieving high pulse numbers. Although electron beam loading may have to deal with effects related to volumetric heating whereas the photon penetration depth in the case of laser loading is negligible, no qualitative differences in damage behaviour and damage threshold for tungsten after ELM-like thermal shock tests performed in the electron beam device JUDITH-1 and pulsed Nd:YAG laser are found [11]. The compatibility of these two simulation methods allows for a direct comparison of results provided by these distinct methods.

1.2.2 Synergistic effects of transient heat loads and plasma presence

As a large part of the ITER divertor will be equipped with tungsten armor, this material was investigated thoroughly under several loading conditions. Strong surface morphology modifications such as blistering [12] and helium-induced nanostructures [13] are observed when tungsten targets are exposed to a high-flux plasma environment.

Driven by ELM hazards, transient heat load studies from either electron guns or laser irradiation have shown to induce melting, enhance erosion, and lead to the formation of thermal shock crack networks and surface modifications of tungsten [9]. Also, enhanced damage effects have been observed for transient heat loads on samples pre-exposed by a high flux hydrogen plasma [11] [14].

While many experiments around the world simulate either the steady state or transient flux, few do so simultaneously. Especially these experiments are of great value since enhanced damage to target materials due to synergistic effects between plasma and transient heat/particle loads are expected compared to the case of transient heat loads or steady-sate plasma solely. Among others, this is shown in PISCES-A where plasma-material interactions were studied by applying a pulsed laser to reach ELM-like heat loads on top of a steady state plasma comparable to that of a large tokamak in normal operation. Enhanced tungsten erosion effects are explained by bursting of gas-filled bubbles and self-sputtering due to the ionization of tungsten atoms in the near surface plasma [9]. Besides effects on tungsten, strongly enhanced surface damage due to combined effect of hydrogen plasma exposure and surface heating by nanosecond laser pulses on rhodium surfaces are observed [15]. On the other side, self shielding effects caused by the detached plasma could account for counteraction in damage development of the target materials during ELMs [16].

1.3 Problem statement

In this thesis, heat load studies on tungsten using a powerful pulsed millisecond laser are described. A variety of loading conditions such as simultaneous plasma presence and irradiation of plasma pre-exposed samples have been investigated in order to study synergistic effects. The central questions is:

How does plasma exposure modify the behaviour of tungsten during intense thermal loading?

Thermal loading is performed by applying a pulsed millisecond laser. This pulse duration better mimics actual ELM duration than in the case of a nanosecond pulse as in previous work. Besides laser loading of targets pre-exposed to a helium plasma, the effects of simultaneous hydrogen plasma presence and transients are benchmarked by comparing results of the two conditions

separately. In addition, evolution of thermal properties of tungsten related to power handling are monitored over large numbers of pulses (>5000). To summarize, the key issues addressed in this thesis are:

- Time-evolution studies of tungsten power handling capabilities exposed to transient heat loads.
- Mapping the damage effects of pre-exposed samples to both deuterium and helium plasma.
- Evidencing synergistic effects on damage creation.
- Mapping the damage thresholds as function of loading conditions in the case of simultaneous plasma and pulsed laser loading.

To be able to systematically investigate damage caused by separate components of our setup, results of laser only irradiation, laser loading on pre-exposed targets to hydrogen and helium plasma and simultaneous laser and hydrogen plasma exposure were separately obtained and will be presented likewise in this thesis.

In the next chapter, a theoretical background that will be used as a reference in later chapters, is provided. The experimental methods are discussed in chapter 3, along with specifications of the components and a description of the applied analysis methods. In order to benchmark created damage due to several specific loading conditions, surface modifications in pristine tungsten targets due to laser impact only are described in chapter 4. Irradiation of targets pre-exposed to a deuterium- and helium plasma and simultaneous plasma and laser are discussed in chapters 5 and 6 respectively. In the final chapters, conclusions are drawn based on a comparison of damage from the different loading methods and the implications for ITER are discussed.

Chapter 2

Theory

2.1 Properties of tungsten

Tungsten has atomic number 74 and is most commonly found in its body-centered cubic (bcc) crystalline form. Besides amorphous tungsten, two other crystallographic configurations can exist. Those configurations are metastable and convert to bcc-structure when heated above 600-700 °C [17]. Due to strong covalent bonds formed between the 5d electrons, tungsten exhibits the highest melting point (3422 °C), lowest vapor pressure and the highest tensile strength among the pure metals. Also, tungsten has excellent heat transfer properties and exhibits the lowest coefficient of thermal expansion.

2.2 Various temperature regimes

In order to understand the physics governing tungsten material reaction to high thermal fluxes, several processes can be distinguished by temperature. When subjected to tensile stresses, tungsten behaves in a brittle manner at low temperatures. Above a certain temperature threshold, called the ductile-to-brittle transition temperature (DBTT), this behavior changes. The DBTT lies in the range of 200-300 °C which depends on mechanical, structural, and chemical conditions[17]. Since this threshold value is rather high compared to other metals, W is notoriously hard to process. The low temperature brittleness is attributed to weak grain boundaries which easily leads to intergranual cracking when below DBTT. Transgranular cracking can also occur, depending on the deformation history, purity and stress state.

Another important threshold parameter governing several processes is the recrystallization temperature: 1300-1500 °C. When heated above this temperature, the structure of tungsten is altered due to grain growth, hereby causing changes in its thermal properties. With this, the DBTT is increased which in turn reduces strength and hardness. In general: smaller grains lead to greater strength (fine-grain strengthening). The zone in which recrystallization takes place is determined by the temperature gradient. This, in turn, depends on the heat penetration depth that scales with the square root of the heat pulse duration.

The material most drastically alters during a phase transition. When heated above them melting point of 3422 °C, tungsten enters the liquid phase. Further heating leads to significant evaporation. Since temperature gradients in the PFM are the key parameter indicating the thermal shock behavior, the base temperature has a profound influence on this. The heat load impacting the surface during transient heating causes plastic deformation. During cool down, stresses are developed. By increasing the bulk temperature, too large plastic deformation between the heated surface and cooler base can be avoided which prevents the material from brittle crack formation.

As a consequence of a large number of transient heat loads, the material can be additionally damaged due to fatigue effects that start to play a role over time. These processes are hardening

and recrystallization [2]. Since a hardened material has a higher resistance to plastic deformation, the material's ability to withstand the periodic plastic deformation is degraded over time.

2.3 Tungsten thermal shock impact resistance

During transient events, all energy is disposed in a limited volume near the loaded surface. The penetration depth of these thermal shocks events roughly scale with the square root of the pulse duration. This leads to steep temperature gradients up to several thousand degrees Celsius on a micrometer length scale. Since the material strength is lowered at the surface compared to the bulk, compressive stresses are formed at the surface due to thermal expansion. For high thermal shocks, this can lead to permanent deformation (roughening) of the surface. During cool down, tensile stresses can be sufficient to initiate crack formations perpendicular to the surface. The mechanism described here is illustrated in figure 2.1 for the case of electron beam loading. Although the penetration depth of electrons is much larger than that of photons, the effect is similar to the case of pulsed laser loading. The mechanics of those processes is heavily depending on the grain

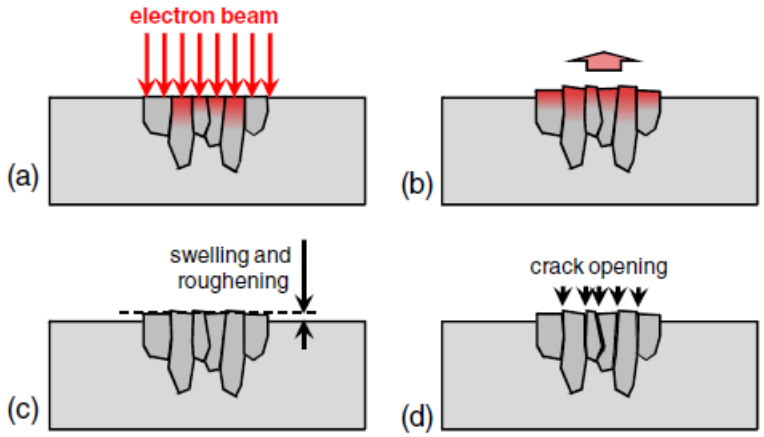

Figure 2.1: Illustration of tungsten thermal shock response: local shallow heating (a), roughening due to thermal expansion (b), permanent deformation upon cool-down (c) and accumulation of tensile stresses during cool-down that initiate crack formation perpendicular to the surface (d).

structure of the surface plane. Grains oriented parallel to the surface increase strength although they could lead to delamination which on its turn can lead to local overheating and subsequently melting [2]. For recrystallized materials, crack formation is strongly enhanced due to grain growth. Crack orientation is affected by recrystallization processes likewise.

The threshold energy to reach melting decreases for higher base temperatures. During cool down, the melted layer resolidifies in a recrystallized state showing a columnar grain structure [2]. In this dynamics, the base temperature is of leading importance. Brittle crack formation will not take place for elevated temperatures (above DBTT) [18]. When the base temperature is above this threshold and when evaporation losses can be neglected, a smooth melt layer will be formed. For increased energy densities, this is layer will be unstable: melted material is ejected from the crater region and resolidifies forming a rim shape around it [18]. The next stage for further increased energies is boiling resulting in ejecting of metallic droplets.

In order to make a direct comparison with heating methods used in other studies, heat loads will be expressed using the so-called heat load parameter $P\sqrt{t}$, expressed in MJ m^{-2} $s^{-1/2}$. This parameter scales linearly with the temperature difference of the impacting heat load:

$$P\sqrt{t} = \frac{1}{2}\sqrt{\pi K c_p \rho}\Delta T \tag{2.1}$$

In this formula, K, c_p and ρ represent heat conductivity, heat capacity and density respectively. Evidently, when those parameters drastically change, as in the case of the formation of for instance a melt layer, strong temperature gradients can occur for lower incident powers which lead to material degradation.

2.4 Laser induced surface heating

Depending on the smoothness of the tungsten surface, wavelength of the laser light and angle of incidence, the radiation energy is partly absorbed by the material. For an infrared laser operating at 1064 nm, the theoretical reflectance (R) in vacuum for perpendicular incidence for a pristine tungsten sample is 0.60254, as obtained from the Fresnel equations [19]. From this, the absorbed radiation fraction $1-R$ is converted into heat which penetrates deeper in the material by diffusion.

For a square laser pulse of duration t_p, the temperature rise at the surface (ΔT) due to this power flux (q) can be expressed using the following 1D model [20]:

$$\Delta T = T_s(t_p) - T_0 = q\frac{2\sqrt{t_p}}{\sqrt{\pi K \rho C_v}} \tag{2.2}$$

in which T_0 represents bulk temperature and K, c and ρ represent thermal conductivity, specific heat and density respectively.

When radial and axial (i.e. perpendicular to surface) diffusion is taken into account, the following expression gives the heat transfer for a square energy flux on the surface at radial position (r) and depth (z) after a time (t) [20]:

$$\begin{aligned} T(r,z,t) - T_0 = \int_0^\infty d\lambda [\frac{I}{2K\lambda} BesselJ[0, r\lambda] BesselJ[1, a\lambda] \\ \times (e^{-z\lambda} Erfc[\frac{z}{\sqrt{\pi\alpha t}} - \sqrt{t\alpha}\lambda] - e^{z\lambda} Erfc[\frac{z}{\sqrt{\pi\alpha t}} + \sqrt{t\alpha}\lambda])] \end{aligned} \tag{2.3}$$

where $\alpha = \frac{K}{c\rho}$ represents heat diffusivity and a area of the impact zone. The following thermal properties are used for tungsten[17]: K = 177 W m^{-1} K^{-1}, c = 134 J kg^{-1} K^{-1}, ρ = 19.300 kg m^{-3}.

2.5 Melt layer evolution model

In order to model the expected thickness and existence duration of a melted tungsten layer, the 1D-model can be developed further. By using Neuman's solution to the differential equation of conduction of heat in a solid [20], thermal properties for liquid phase tungsten are combined with its thermal properties at room temperature [17]. By extracting the dimensionless number λ as the root of the following function

$$\frac{e^{-\lambda^2}}{erf(\lambda)} - \frac{K\sqrt{\alpha_m} T_m e^{-\frac{\lambda^2 \alpha_m}{\alpha}}}{K_m \sqrt{\alpha}(T_s(t) - T_m) erfc(\lambda\sqrt{\frac{\alpha_m}{\alpha}})} = \frac{\lambda L \pi^{\frac{1}{2}}}{c_2(T_s(t) - T_m)}, \tag{2.4}$$

the depth of the melt layer d_m as a function of time (t) and surface temperature T_s above melting temperature T_m can be determined using:

$$d_m(t) = 2\lambda\sqrt{\alpha_m t}. \tag{2.5}$$

In these equations, L represents the latent heat of fusion, c_p the heat capacity at room temperature, k the thermal conductivity and α the thermal diffusivity. The subscript m denotes the liquid (melted) phase of the material as opposed to the solid state (s).

Chapter 3

Experimental setup

The experiments described in this thesis were performed in the linear plasma generator Magnum-PSI at DIFFER, designed to study plasma-wall-interactions in ITER-like high-flux regimes. Laser experiments without plasma presence were conducted in the Target Exchange and Analysis Chamber (TEAC) of this machine whereas the simultaneous exposures were performed in the Target Chamber (TC). Pre-exposure of tungsten samples to a helium plasma was performed in Pilot-PSI, a small precursor of Magnum-PSI. Pulsed laser heating is done using an industrial LASAG microwave laser with millisecond pulse length. Sample preparation, the basic setup of Magnum-PSI and the LASAG laser and its coupling with the plasma device will be discussed hereafter. Following this section, used diagnostics and analysis methods are described.

3.1 Tungsten specifications and sample preparation

The tungsten samples used for all experiments described in this thesis are polycrystalline tungsten discs, manufactured by Plansee AG, Austria. The discs are cut from a rolled tungsten rod of 99.97 % purity and measure 30 mm in diameter with a thickness of 1 mm. Targets are polished to a mirror finish having roughness down to 0.05 μm with typical grain size of a few microns. Subsequently, the targets are ultrasonically cleaned in ethanol and acetone. In order to outgas and relieve stresses in the material, the targets where heated up to 1000 °C for 60 minutes by using temperature ramping of 1 °C per second.

3.2 Magnum-PSI

Magnum-PSI is a linear plasma device capable of producing a quasi steady-state high flux plasma. It consists of vacuum pumps, a source chamber, a target chamber surrounded by magnetic coils, a retractable target holder and an analysis chamber. A schematic overview of the entire machine is shown in figure 3.1. By applying a strong electric field in the source, the injected gas becomes ionized. Due to a pressure gradient between the source channel and the adjacent cylindrical target chamber, the high density plasma leaves the source. Although Magnum-PSI is capable of working with several gasses, only hydrogen is used for the simultaneous plasma and laser exposures. The source was operated using a DC current between 150-190 A and gas flow ranging 5.0-7.0 Pa m^3 s^{-1}. By switching on the magnets, an axial magnetic field (max. 0.47 - 1.88 T) is created that confines the plasma into a beam hitting the target (fig. 3.2). In this way, a particle flux in the order 10^{23} particles/m^2 is reached. The duration of the steady state plasma is limited by heating of the copper solenoids of the magnet. During plasma exposure, the targets are actively water-cooled. Samples are mounted on a copper heat sink having internal water channels. Between this and the tungsten sample, an interlayer of grafoil® having excellent heat transfer properties is positioned. For laser loading without simultaneous plasma, no cooling is applied. As will be discussed in greater detail

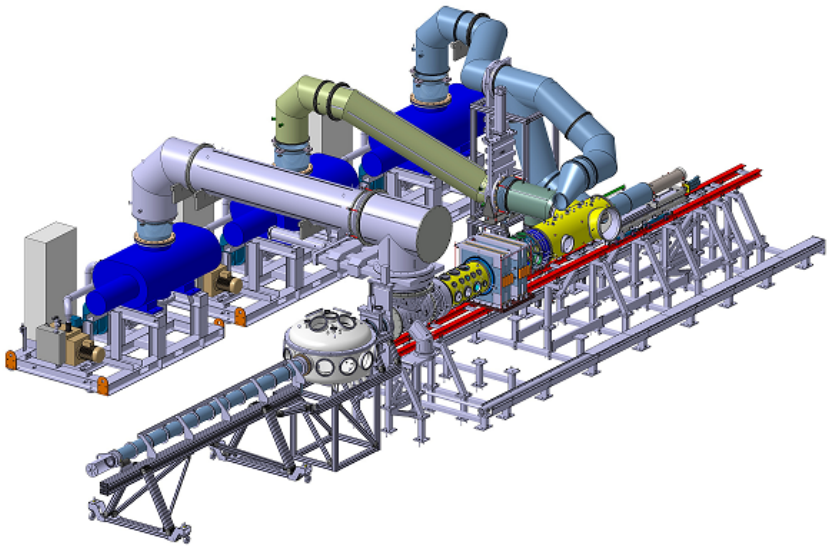

Figure 3.1: Overview of the linear high-flux plasma generator Magnum-PSI, capable of producing ITER-relevant plasma conditions. The main components of the machine are vacuum pumps, a target chamber surrounded by copper coils, a target exchange and analysis chamber (TEAC) and a retractable target holder and plasma source.

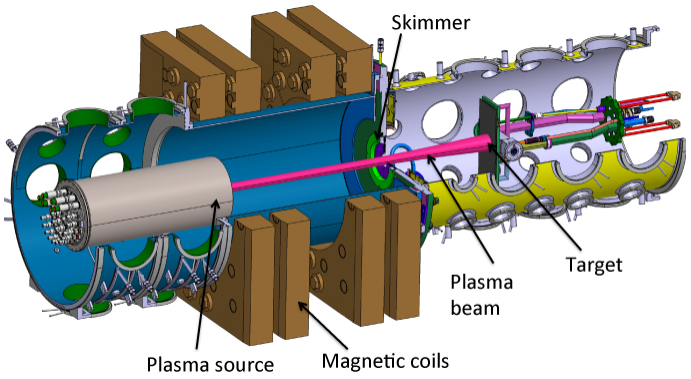

Figure 3.2: Close-up on target chamber of Magnum-PSI. Gas is ionized in the source and subsequently confined in a strong axial magnetic field produced by copper coils, yielding a high density plasma beam. Outside the magnetic region, a slightly expanding beam strikes the water-cooled target.

later on, the creation of steep heat gradients from active cooling largely affects heat penetration and after-pulse decay. All targets are mounted on a movable multiple target holder. By adjusting tilting angle and/or rotation multiple spots on the same targets can be irradiated (fig. 3.3).

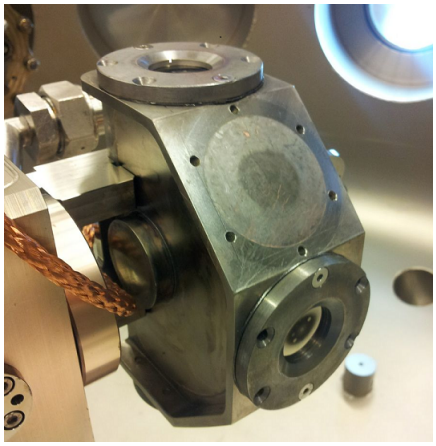

Figure 3.3: Movable multiple target holder of Magnum-PSI. Two samples (top and front) exposed to a helium plasma and subsequent pulsed laser loading can be seen. By adjusting tilting angle and rotation of the target holder by small amounts, several positions on one sample can be irradiated.

3.3 LASAG and laser injection system

In order to replicate transient heat pulses, a fibre-coupled Nd:YAG welding laser (LASAG FLS 352-302) is used. The input power ranges from 1-21 kW and a pulse duration of 1 ± 0.1 ms is applied. Besides, repetition rates of 10, 20 and 25 Hz were set. With these settings, surface heat loads suitable for realistic simulation of type-1 ELMs are achieved [5].

The fiber has a length of 35 m, diameter of 400 μm and allows for $83.5 \pm 0.5\%$ transmission. The spatial laser beam profile exiting the fiber is a flattened gaussian. This shape is maintained upon arrival at the target, based on analysis using the IR camera. The temporal profile is a nearly-square function, as can be inferred from figure 3.4 [21]. Next to transmission losses in the fiber, the

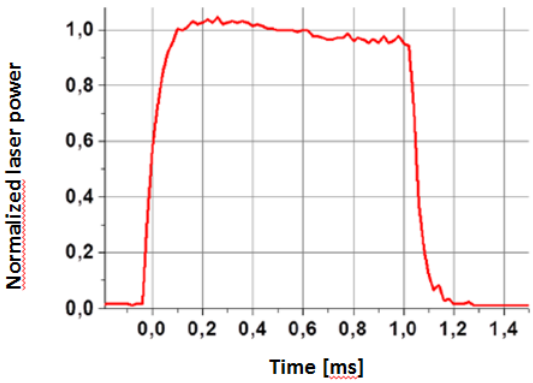

Figure 3.4: Temporal profile of LASAG laser beam

arriving laser beam power is furthermore decreased due to losses in the mirror, collimating lens and vessel window. For the simultaneous laser and plasma exposures performed in the Magnum target chamber, the total transmission is found to be $69 \pm 1\%$. For loading experiments in the TEAC, an initial transmission of $49 \pm 1\%$ and improved transmission of $66 \pm 1\%$ are found. A schematical overview of the TEAC injection system is shown in figure 3.5. The transmission values stated here are used in determining actual heat load parameters arriving at the target.

Achieving the smallest possible spot size is important to achieve high energy densities locally.

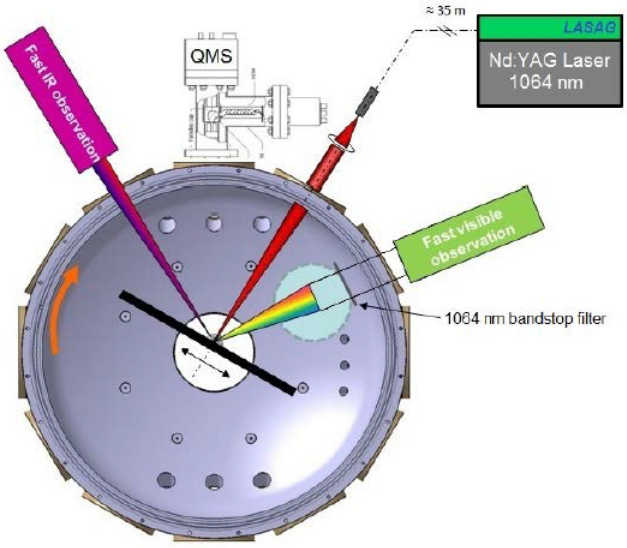

Figure 3.5: Schematic experimental setup of laser loading in TEAC

By using a visual alignment laser, the lens distance is varied in order to minimize the irradiation area. The spot size of the high power infrared laser is slightly different from this and is determined from taking the FWHM of the gaussian heat pulse that is obtained from IR camera processing. By integrating a 2D gaussian, the circular area with a radius of $\frac{1}{2}FWHM$ contains 0.5 of the entire volume. Therefore, the stored energy within the FWHM contains 50% of all input energy.

To summarize, the actual heat load arriving at the target is calculated by taking into account transmission losses in fiber and injection system (α_T), fraction of stored energy deposited within FWHM (α_{FWHM}), absorption at target (α_w), spot size (A) and set pulse duration (t):

$$F_{HF} = \alpha_T \alpha_{FWHM} \alpha_w \frac{E_{in}}{A\sqrt{t}}. \tag{3.1}$$

3.4 Diagnostics

3.4.1 Thomson scattering

Plasma parameters such as electron density (n_e) and electron temperature (T_e) are measured using incoherent Thomson scattering (TS). This technique is based on elastic scattering of electromagnetic radiation by charged particles. A pulsed Nd:YAG laser operating in second harmonic (532 nm) penetrates the plasma and is scattered in random directions. The scattered light is collected by an array of fibers yielding a radial distribution of plasma parameters. From this, a radial distribution of particle flux to the target can be derived assuming sonic velocity of the plasma ions at the entrance of the electrostatic sheath.

3.4.2 Infrared thermography

Infrared thermography is used for monitoring the evolution of induced heat from laser pulses and plasma heating at the target remotely. For this purpose, a fast infrared camera (FLIR SC7500MB) capable of measuring up to 10.000 kHz is applied. By setting integration times ranging from 10-200 μs and high frame rate, pulse evolution can be observed in great detail. In order to convert the raw data from collected infrared light emitted by the target into temperature, transmission of this diagnostic system and target emissivity needs to be known. The IR transmission through

the window of the vacuum vessel is assumed to be 90% and a temperature dependent emissivity calibration file (ranging from 27-3327 °C) is applied for data processing using a code written in IDL.

3.5 Post mortem analysis methods

Post-mortem analysis such as scanning electron imaging, laser profilometry, reflectophotometry and ellipsometry measurements are performed and briefly discussed hereafter.

3.5.1 Scanning electron microscopy

In order to examine surface modifications, Scanning Electron Microscope (SEM) images of magnifications up to 15.000X were obtained. Detailed grain size distribution and sub-grain modifications such as nanofuzz and blisters can be observed. SEM analysis is performed at IPP in Czech republic. An EVO MA 15 (Carl Zeiss, Germany) detector with LaB6 cathode and point resolution of 2 nm at 30 kV in high vacuum is used [22]. Besides, a detector for electron backscattered diffraction (EBSD detector e-Flash) is used to do phase microanalysis which yields a higher resolution allowing for detecting individual grains. Applied exposure conditions such as plasma parameters, pulse number and energy density of the laser are related to visual information obtained from SEM later in this thesis.

3.5.2 Reflectivity measurements

An essential aspect related to the performed experiments is to keep track of the exact energy density arriving at the target for subsequent laser pulses. Besides systematic errors such as variation in output energy of the laser itself and variation in pulse duration and spot size, the exact heat load parameter is influenced strongly by reflection at the sample surface. Incidence angle makes a negligible effect: the specular reflectivity changes only by 1 % within the range of applied incidence angles (10-45°), based on Fresnel theory.

The total reflectivity R equals the sum of both specular- and diffuse reflectivity: $R = R_s + R_d$. In case of surface modifications, R_s is lowered due to scattering. R_d is assumed to increase since light can be reflected multiple times within the irradiated area. The origin of surface modifications that give rise to changes in reflectivity can be distinguished in plasma-related and laser-induced modifications. Specular reflectivity for pristine W targets at 1064 nm is measured to be $62 \pm 2\%$. For plasma-exposed targets, specular reflectivity is found to be $56 \pm 1\%$ [14]. Besides this effect, Laser-induced modifications are gradually built up due to subsequent laser pulses. Estimating the change in reflectivity is therefore complex. Specular reflectivity in the wavelength range 300-800 nm at 40° angle of incidence is obtained from measurements using a Sentech SE850 ellipsometer performed by L. Marot in Basel, Switzerland and results are presented in the next chapter.

In order to estimate total reflectivity ($R_s + R_d$), ellipsometry measurements have been performed on several damaged spots of increasing roughening exposed to 100 laser pulses. By this method, a change of polarization of the incident light due to interaction with the sample material is measured. Since this technique is intensity independent, measurements are not influenced by diffuse reflectivity. By fitting data of an imaginary sample containing a certain level of roughening, the dielectric properties (n, k) of the material can be estimated. With this, total reflectivity can be calculated from the Fresnel equations describing the behaviour of light when moving between media of different refractive indices. Results on this are compared with direct specular reflectivity measurements as will be shown later.

By correcting for a change in laser beam reflectivity for applied conditions, and hence taking a variable heat load into account, power handling capabilities (i.e. the evolution of the laser pulse induced temperature increase) of the target material can be studied which is one of the main goals of this project.

3.5.3 Laser profilometry

Besides the qualitative information obtained from SEM imaging, quantitative determination of roughening is obtained from laser profilometry. In this way, numerical thresholds of roughening are related to loading conditions. The laser profilometer (Polaris from UBM Messtechnik GmbH) measures surface elevations of ± 500 μm with an accuracy up to 10 nm using the reflectivity of a 670 nm laser. Around the circular loaded area, a square surface of 2.2×2.2 mm is scanned with a lateral solution of 10μm in both the x- and y-direction. The roughness parameter (R_a) is defined as the arithmetic average of the deviation from the average height ($< z >$):

$$< z > = \frac{1}{MN} \sum_{m=1}^{M} \sum_{n=1}^{N} z(x_m, y_n) \tag{3.2}$$

$$R_a = \frac{1}{MN} \sum_{m=1}^{M} \sum_{n=1}^{N} |z(x_m, y_n) - < z > | \tag{3.3}$$

Chapter 4

Pulsed laser heating

To be able to investigate surface modifications and power handling of pristine tungsten due to laser impact only, both a scan on pulse number and power are performed. The results are used later to quantify the effect of plasma exposure on laser-induced surface damage. The temporal evolution of the surface temperature during the laser pulse is followed with high temporal resolution using the fast infrared camera. From this, qualitative information regarding heat transfer capabilities is gained. The applied loading conditions are summarized in table 4.1. Pulse duration and repetition rate are 1 ms and 10 Hz respectively.

experiment	**P [GW m^{-2}]**	**F$_{HF}$ [MJ m^{-2} $s^{-1/2}$]**	**pulse number**
pulse number scan	1.18	37.5	1
	1.18	37.5	10
	1.18	37.5	100
	1.18	37.5	1000
	1.18	37.5	5000
power scan	0.46	14.5	100
	0.69	21.7	100
	0.92	28.9	100
	1.14	36.2	100
	1.37	43.3	100

Table 4.1: Laser loading conditions on pristine W. Pulse duration is 1 ms in all cases. The applied pulse repetition rate is 10 Hz.

4.1 Change of laser energy absorption due to surface roughening

Based on measurements from ellipsometry and direct reflectance measurements using a spectrophotometer, a total reflectivity of 58% is found for pristine W surfaces. As the operation wavelength of the pulsed laser (1064 nm) is much higher than maximum roughness of the polished surface (∼10 nm), light reflectivity can be assumed to be almost exclusively specular and therefore governed by the Fresnel equations. As the surface gets roughened as a consequence of stored compressive stresses formed during thermal expansion, light is scattered several times within this area. Besides, due to thermal cycling, the microscopic irregularities at grain boundaries grow. This causes further scattering and multiple reflection. Specular reflectivity is decreased whereas reflection occurs more and more in a diffuse way as is depicted schematically in picture 4.1.

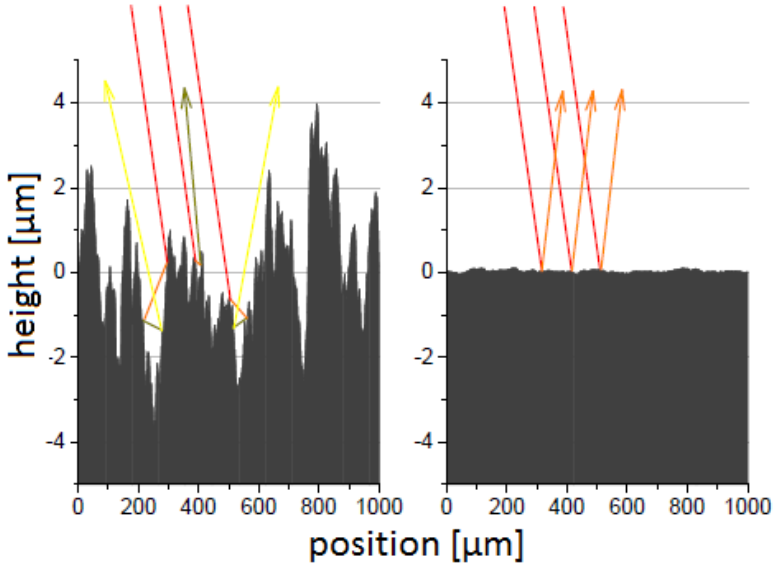

Figure 4.1: Reflection from a roughened- (l) and polished tungsten surface (r) [23]. As a consequence of partly diffuse reflectivity in the case of a roughened surface, light is reflected multiple times accounting for an enhanced absorption.

During each reflection, part of the energy carried by the light is absorbed. Specular reflectivity (for linearly polarized light) of W in the 300-800 nm range is obtained for a range of modified surfaces. For damaged areas subjected to 1, 10 and 5000 pulses, specular reflectivity is shown in 4.2a. As can be seen, for pulses at $F_{HF} = 35$ MJ m^{-2} $s^{-1/2}$, the reflectivity decreases progressively when the number of laser pulses increases. For the case of 5000 laser pulses, the surface is heavily damaged and R_s is negligible. At this site, large melted areas are observed by SEM as will be shown later. Besides, deep cracks are created. These effects account for impeding direct reflection.

Figure 4.2b shows that for a fixed number of 100 pulses, R_s decreases with increasing heat load parameter. A similar trend as in the case of increasing pulse number is observed here although R_s is not negligible in the case of highest applied heat load. It decreases down to ∼14% of the incoming intensity for points subjected to 100 pulses at $F_{HF} = 43.3$ MJ m^{-2} $s^{-1/2}$. However being a small difference, R_s for the area subjected to $F_{HF} = 43.3$ MJ m^{-2} $s^{-1/2}$ is higher than the area loaded to $F_{HF} = 36.2$ MJ m^{-2} $s^{-1/2}$. As is be observed from SEM images, the surface for this highest heat load seems far less roughened in the centre than in the case of 100 pulses of $F_{HF} = 36.2$ MJ m^{-2} $s^{-1/2}$. This is explained by a reordering of grains during the process of resolidification after transient melting.

Ellipsometry measurements were carried out yielding the local dielectric properties n and k at local laser damaged areas. From this, using Fresnel equations that describe the behaviour of light moving between media of different refractive indices, the total reflectivity is determined. Results are shown in figure 4.3. In general, the changes of total reflectivity are much less pronounced than the changes in R_s. For heat loads >15 MJ m^{-2} $s^{-1/2}$, total reflectivity seems to go down by about 12% relative to the initial pristine reflectivity. As R_s decreases by about 50% compared to the undamaged case, R_d must have been increased accordingly. This indicates a strong increase in surface roughness which will be confirmed by SEM analysis and laser profilometry shown in the next section. The two data points indicating R_{tot} at heat loads of 36.2 MJ m^{-2} $s^{-1/2}$ and 43.3 MJ m^{-2} $s^{-1/2}$ are again higher. The values for the fraction of absorbed energy as shown in figure 4.3, will be used later on for determining the actual heat load that penetrates the modified W surface.

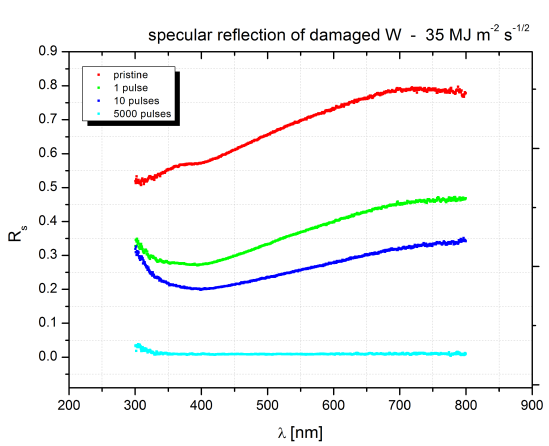

(a) R_s of pulse number scan

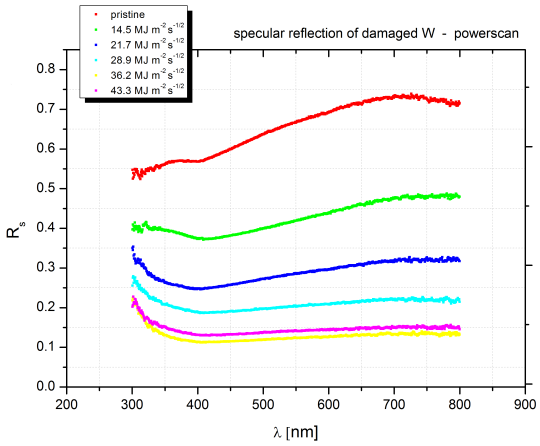

(b) R_s of power scan

Figure 4.2: Specular reflectivity measured using a spectrophotometer. Direct reflectivity of light for a range of wavelengths at the position of pristine and damaged W due to 1, 10 and 5000 pulses at 37.5 MJ m^{-2} $s^{-1/2}$ (a). Specular reflectivity from a range of heat loads for 100 pulses each (b).

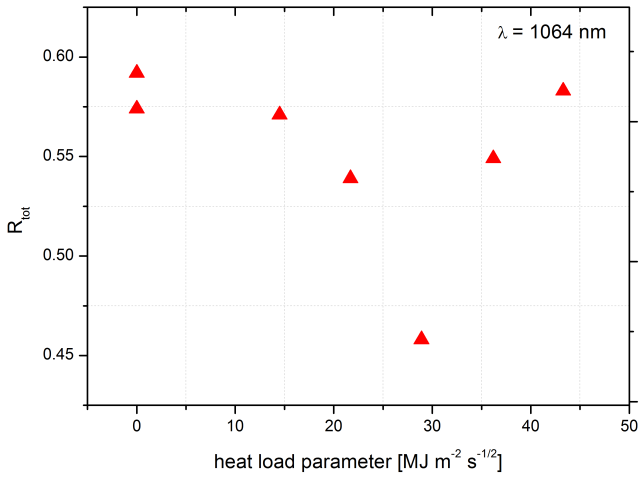

Figure 4.3: Total reflectivity at 1064 nm of affected laser spots from ellipsometry analysis. These locations where subjected to 100 laser pulses at heat loads as indicated on the x-axis.

4.2 Surface morphology

4.2.1 SEM results

SEM results of the pulse number scan ranging from 1 to 5000 pulses at 10 Hz and $F_{HF} = 37.5$ MJ m^{-2} $s^{-1/2}$, are presented in figures 4.4 to 4.8. A description of the observed surface morphologies is given. By an increasing number of consecutive pulses on a polished tungsten target of fixed power, a gradual increase of surface modifications such as grain growth, delamination of grains, melting and eventually cracking is observed. This indicates a metal fatigue effect that comes into play. At the applied laser power, the surface is heated up to ~2000 °C in 1 ms causing recrystallization and resizing of grains. Besides these effects, discontinuous melted areas within the irradiation spot are visible after 100 pulses and higher at $F_{HF} = 37.5$ MJ m^{-2} $s^{-1/2}$ which

grow with progressing pulse number. It is interesting to see that melting starts to occur for these high pulse numbers where the applied heat load on a pristine sample is far from sufficient to heat up near the melting threshold (3422 °C), based on theoretical predictions of the surface temperature during a transient for pristine W. Apparently, local over-heating sets in, indicating a local reduced thermal conductivity for the affected surface. This mechanism carries on gradually during the succession of pulses. As melting is not observed in the case of single pulse and 10 pulses, a melting threshold dependance on the number of shots seems to be present. For pulse numbers >1000, an increase in the melted surface area is accompanied by the formation of large cracks of typically 20 μm wide and 200 μm deep.

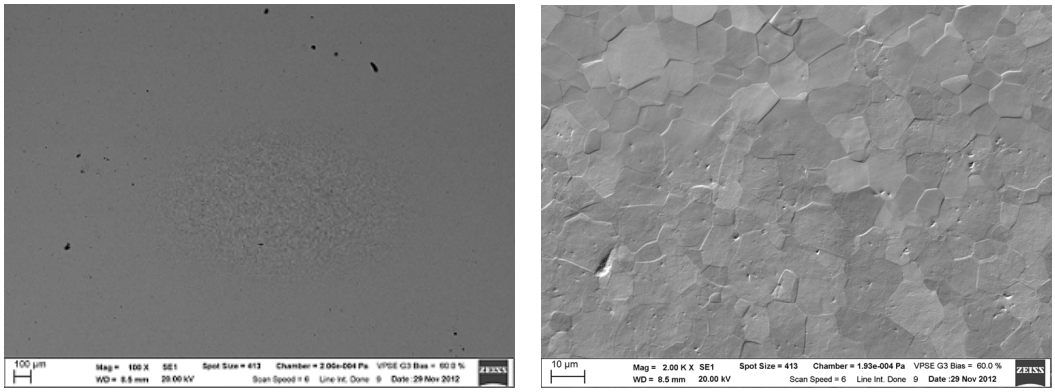

Figure 4.4: Surface morphology after a single pulse at $F_{HF} = 37.5$ MJ m^{-2} $s^{-1/2}$ performed at room temperature. Submicron scale roughening. The grain boundaries are more accentuated compared to the unexposed surface grains. A single pulse pushes the surface temperature well above the recrystallization threshold (∼1300 °C) which causes immediate recrystallization followed by grain growth. Grain size decreases radially outward from the center: ∼10 μm to ∼1 μm, where the latter is the original grain size.

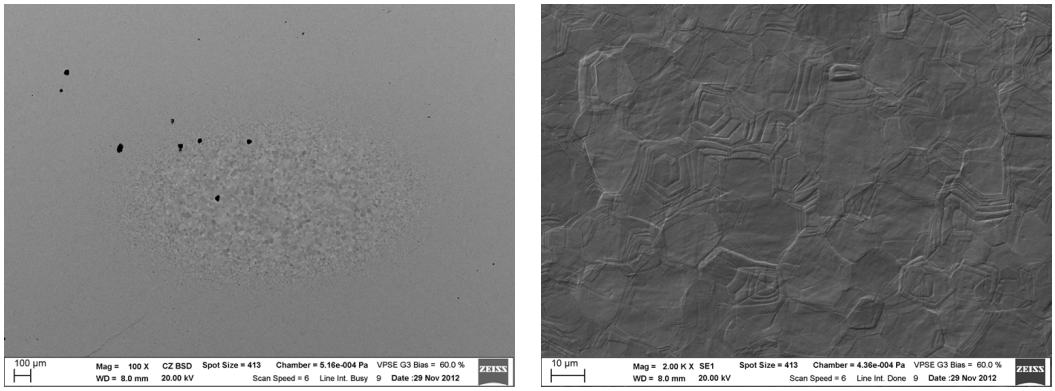

Figure 4.5: 10 pulses at $F_{HF} = 37.5$ MJ m^{-2} $s^{-1/2}$. Recrystallization and increase in grain size compared to single pulse loading but separate grains are clearly discernable. The grains show a pyramid shape: grains in decreasing size stapled on top of each other.

As the effect of pulse number for high laser energy is mapped out, surface morphologies for increasing laser power for 100 pulses each is shown in figures 4.9-4.13. For this number of pulses, no cracking is observed for any of the applied heat loads. However, the onset of melting is observed for heat loads >36 MJ m^{-2} $s^{-1/2}$ leading to a contiguous melt pool with large grains after loading at $F_{HF} = 43.3$ MJ m^{-2} $s^{-1/2}$. The average peak temperature measured in the centre of the loading areas were melting is observed is 2442±94 °C and 2690±90 °C respectively, again below

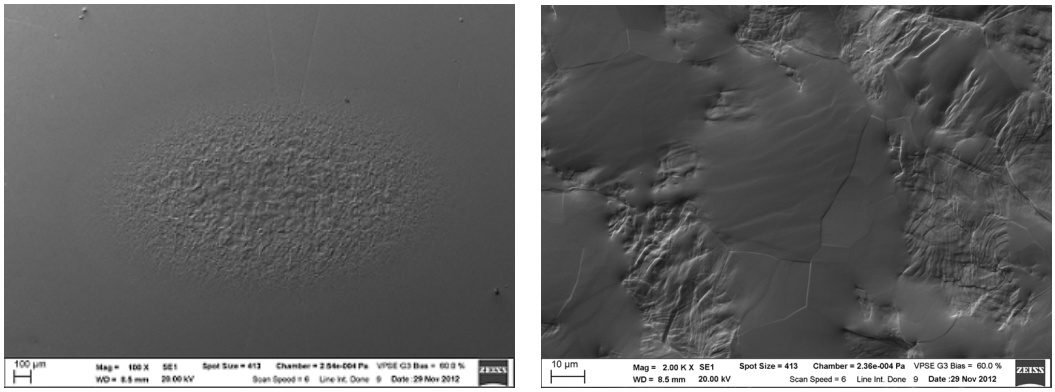

Figure 4.6: 100 pulses at $F_{HF} = 37.5$ MJ m^{-2} $s^{-1/2}$. Typical small-scale irregularities and discontinuous melted patches. The resolidified surface grains show clear boundaries whereas this is not visible in non-melted areas.

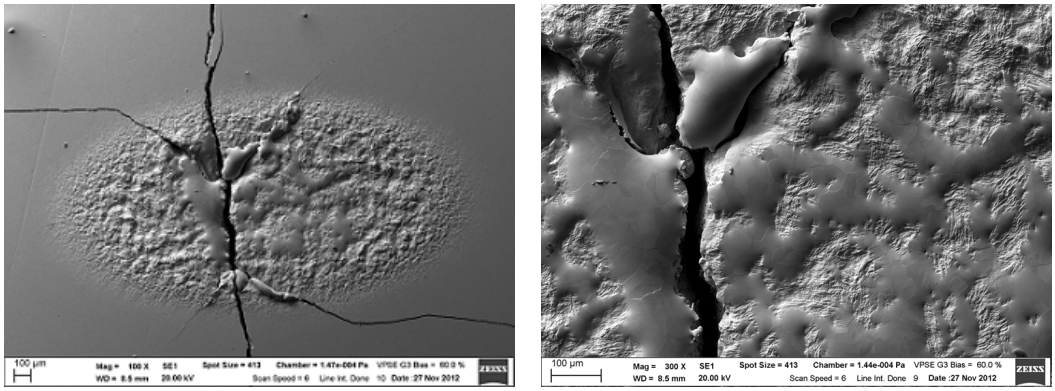

Figure 4.7: 1000 pulses at $F_{HF} = 37.5$ MJ m^{-2} $s^{-1/2}$. Heavily affected irradiation zone. Deep cracks with large extend originate in centre, surrounded by melted material. A large (500μm) contiguous melt pool can be observed. Smaller melted islands further out of centre. At the edge, ridges smoothly vanish with increasing distance from the centre.

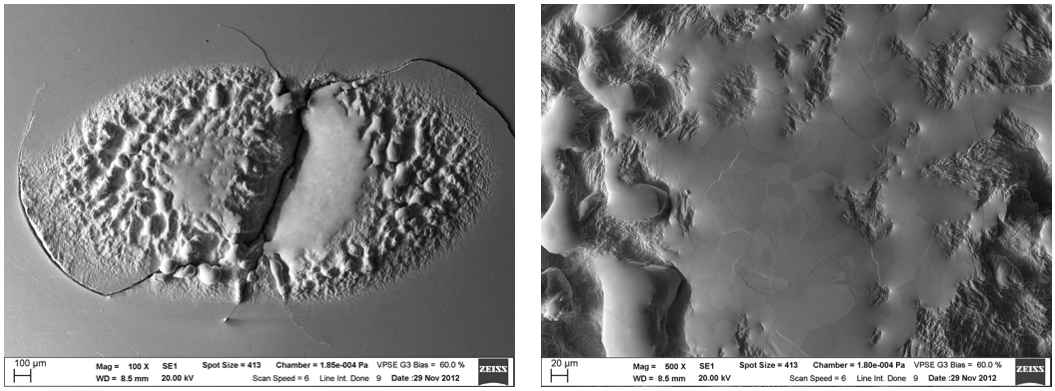

Figure 4.8: 5000 pulses at $F_{HF} = 37.5$ MJ m^{-2} $s^{-1/2}$. Nearly the entire surface shows melted features. A large deep melt pool next to a crack in the center and smaller 'blobs' of splashed material further out. Circular shaped cracks around the damaged area.

the W melting threshold of 3422 °C. The peak temperature is measured in the centre and spatial distances of about 1/4 of the FWHM of the heat pulse are resolved. As melting of individual grains start as an effect of local reduced thermal conductivity, these tiny spots are not resolved by the IR-camera which explains the apparent discrepancy between the visual evidence of the onset of melting and the recorded temperature.

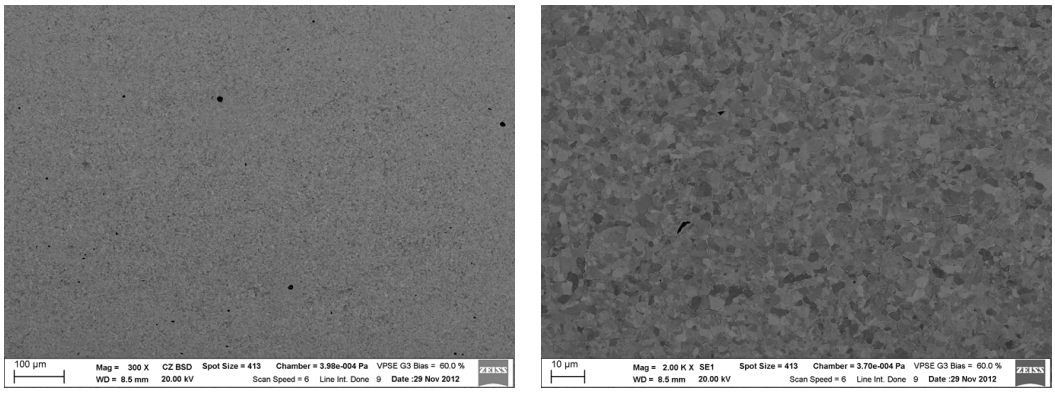

Figure 4.9: Surface morphology after 100 pulses at $F_{HF} = 14.5$ MJ m^{-2} $s^{-1/2}$. Barely discernable morphology changes at this loading condition. Grain boundaries are more accentuated in centre of irradiation zone, as is inferred from secondary electron emission images. Average peak temperature: 1040 °C.

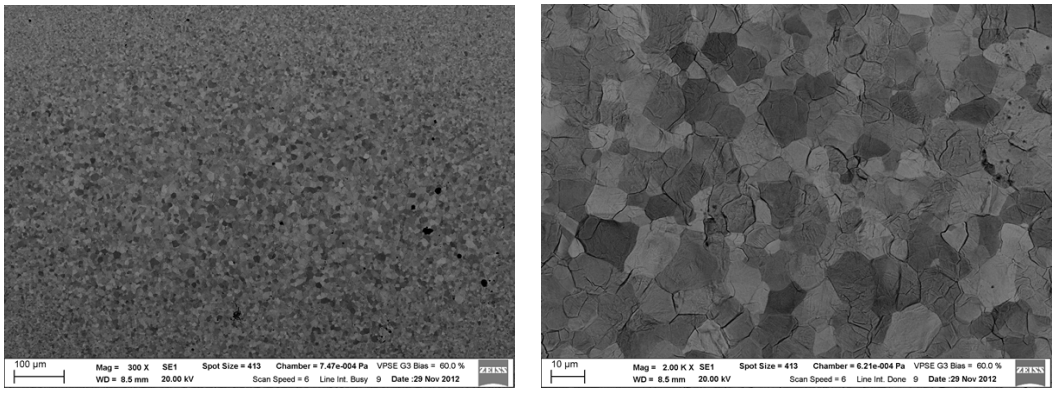

Figure 4.10: $F_{HF} = 21.7$ MJ m^{-2} $s^{-1/2}$, 100 pulses. Shallow roughening and growth of grains. Some grains seem delaminated. Average peak temperature: 1530 °C.

4.2.2 Surface roughening

The observation of increased surface roughening with applied heat load is quantified by the arithmetic roughness (R_a) defined by equation 3.3 obtained from laser profilometry. The results are

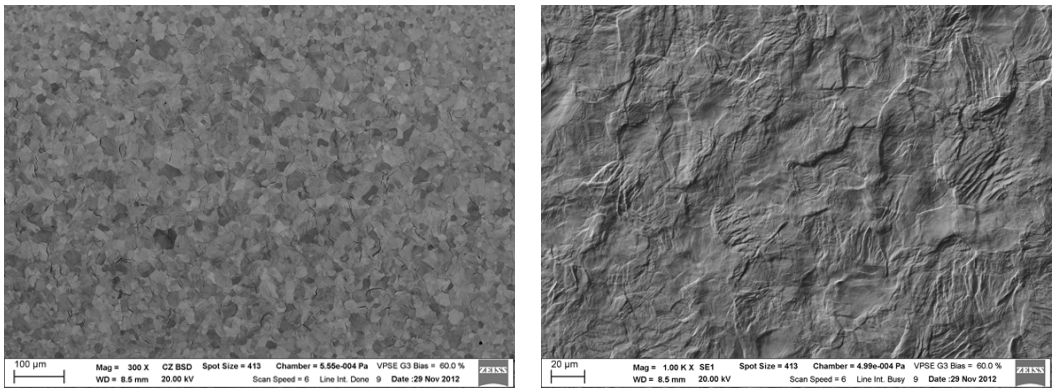

Figure 4.11: $F_{HF} = 28.9$ MJ m^{-2} $s^{-1/2}$, 100 pulses. Intermediate roughening. The grains seem to overlap more and show some scratch-like features. Average peak temperature: 2040 °C.

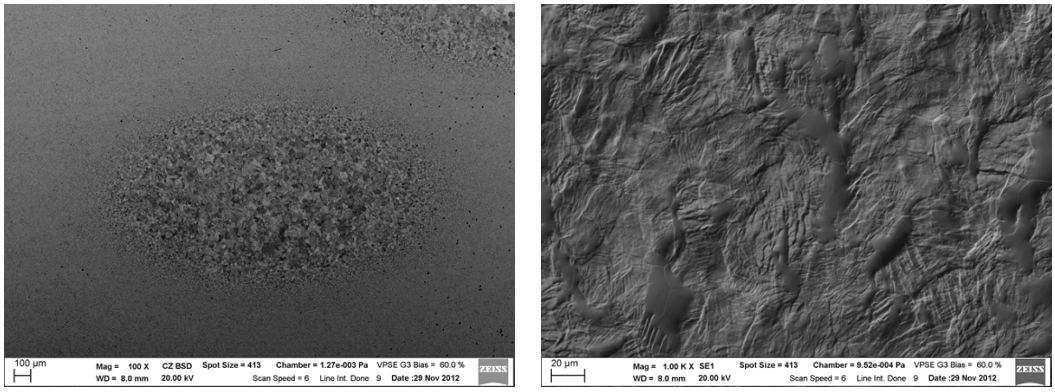

Figure 4.12: $F_{HF} = 36.2$ MJ m^{-2} $s^{-1/2}$, 100 pulses. Shallow but dense roughening. Shallow isolated melted spots. Large grains in centre found in additional pictures. Average peak temperature: 2480 °C.

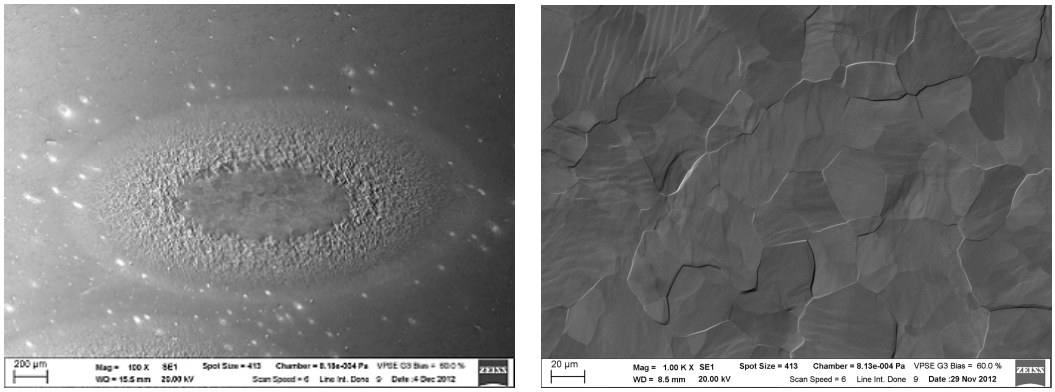

Figure 4.13: $F_{HF} = 43.3$ MJ m^{-2} $s^{-1/2}$, 100 pulses. Shallow, smooth, contiguous melt pool in center of irradiation zone. Protruding re-solidified parts are formed around it. Re-solidified grains in the centre are of much larger diameter than surrounding grains. Average peak temperature: 2730 °C.

shown in figure 4.14. For the exposed spots subjected to the power scan of 100 pulses, the mean roughness increases gradually with the laser pulse energy density. R_a increases drastically in the

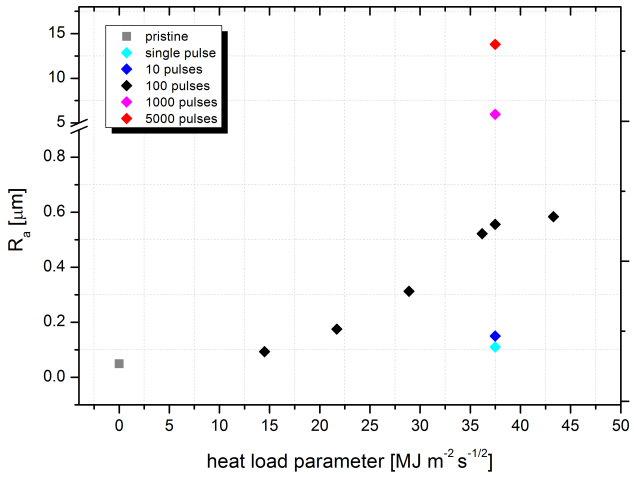

Figure 4.14: Mean roughness (R_a) of laser loaded area as function of pulse number and heat load parameter. In the case of 1000 and 5000 pulses, the average height deviation compared to the pristine surface is large due to formation of a melt pool as is inferred from SEM imaging.

case of 1000 and 5000 pulses. In the latter cases, large-scale melting occurs causing the formation of a melt pool in which material is pushed outwards. The depth of this extends more than 200 μm as is found from line profile observation (fig. 4.15). In the appendix section, the formation of a shallow melt layer due to simultaneous laser loading and plasma exposure at high base temperature is discussed more extensively.

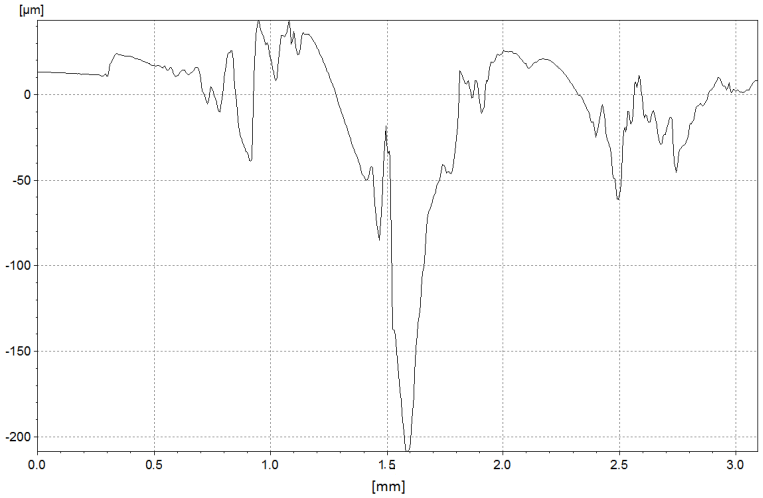

Figure 4.15: Line profile scan along the long axis of the ellipse-shaped laser loaded area subjected to 5000 pulses at $F_{HF} = 37.5$ MJ m^{-2} $s^{-1/2}$. The formation of a melt pool of depth >200 μm can be observed. Material is displaced towards the edges.

As R_a is a measure for the average deviation perpendicular to the surface from an imaginary plane representing the average surface level, the formation of cracks greatly increases this parameter even more as drastic vertical deviations are introduced.

4.2.3 Recrystallization kinetics

By measuring the average grain size from the SEM images (obtained using electron backscattering) in the centre of the modified surface, grain growth with both increasing pulse number and power density is observed. The average grain diameter versus loading conditions and average peak temperature are presented in figure 4.16. The peak temperatures as indicated are the average peak temperatures measured via IR thermography of all pulses applied on a single position. Besides an increase in the average grain size in the centre of the loaded zone, grains gradually decrease in size from the centre radially outwards in all cases. This reflects the gaussian shape of generated heat in the loaded area. The grain growth process seems to occur rather rapidly: within 1 ms (single pulse at $F_{HF} = 37.5$ MJ m^{-2} $s^{-1/2}$). By comparing the average grain size after encountering a single pulse with the effect after a high number of pulses, growth by roughly a factor 3 is found. Assuming recrystallization takes place during 1 ms due to each pulse (during cool-down phase, the surface temperature is still shortly above the recrystallization threshold), loading to 5000 pulses corresponds roughly to 5 seconds for the recrystallization followed by grain growth of this magnitude to occur.

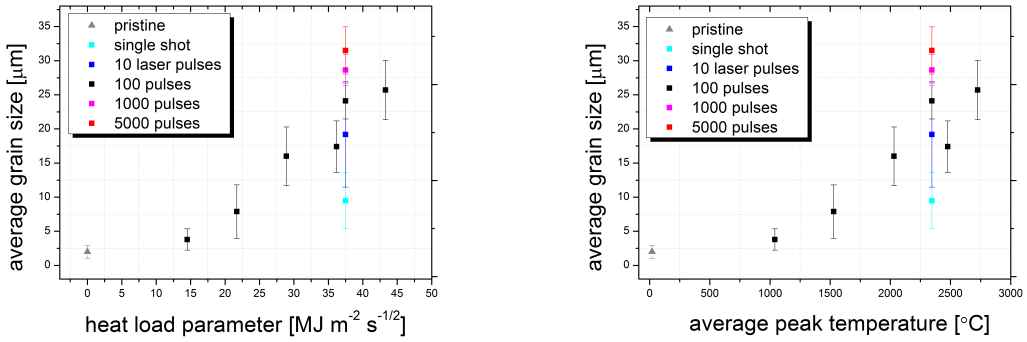

Figure 4.16: Average grain diameter versus laser heat load parameter (a) and average peak temperature (b) in the centre of loaded areas. Peak temperature is defined here as an average over all applied pulses on a single position. Grain growth is observed for temperatures >1500 °C and increases linearly with temperature and pulse number. Single pulse exposure (1 ms) leads to resizing of grains for heat loads >37.5 MJ m^{-2} $s^{-1/2}$.

4.3 Power handling

Peak temperatures reached during transient laser heating averaged over 100 pulses as measured via IR thermography are shown in figure 4.17. The black line in this graphs represents the expected peak temperature predicted by the 1D diffusion model 2.2 assuming a constant 0.5 absorptivity. This models gives the expected peak temperature generated at a pristine surface for a certain laser power and pulse duration where losses in the system as measured experimentally are taken into account. The FWHM of the laser spot is determined from IR images and used as further input. The experimental results seem to be in good agreement with the theoretical values although being slightly higher. This might be attributed to an enhanced absorptivity of the laser light as a consequence of increased roughening and uncertainties in the emissivity of the affected radiating surface. Furthermore, the peak temperature may increase with pulse number as will be discussed hereafter, hereby causing the average peak temperature to increase as well.

An increase in temperature rise per pulse (ΔT) with the succession of pulses is observed as is shown in figure 4.18 were the fractional temperature (i.e. peak temperatures averaged over 10 pulses divided by the average of the first 10) is monitored for increasing pulse number assuming

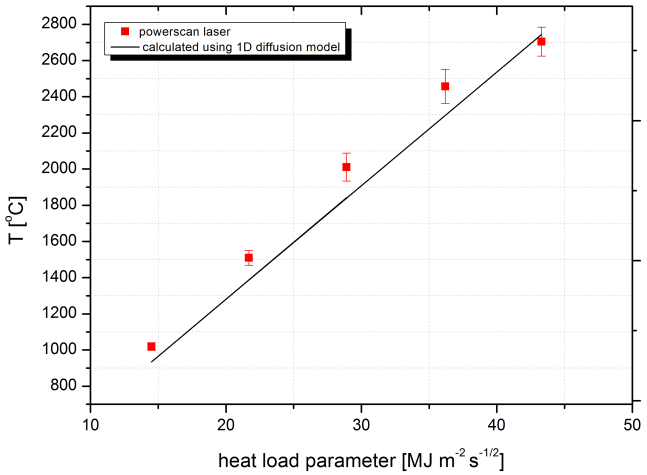

Figure 4.17: Averaged temperature increase of W at the centre of the laser spot measured by IR thermography. The black line represents the theoretical value of the transient temperature as found from the 1D diffusion model for heat loads as indicated. The spots size to determine the actual power density arriving at the target in this model is obtained from IR-images.

a constant energy absorptivity of 42%. As can be seen, the fractional temperature change caused

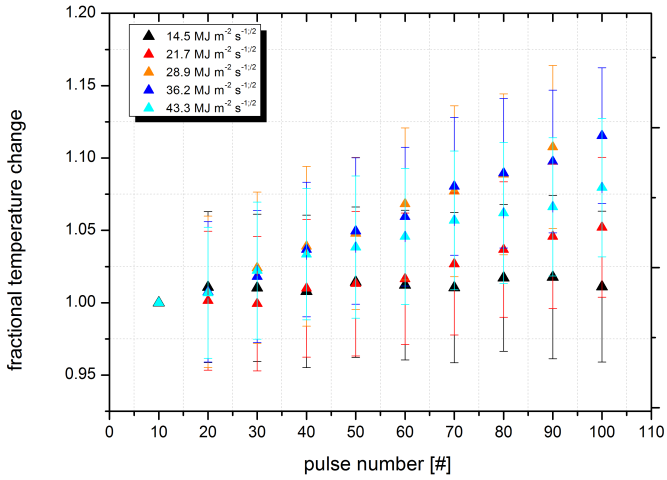

Figure 4.18: Fractional change of ΔT with pulse number during a power scan. The fractional change is defined as ΔT averaged over 10 pulses divided by the average ΔT of the first 10 pulses. A change for absorptivity is not accounted.

by subsequent transients exceeds 10% from initial pulses on the pristine surface over the course of 100 pulses for loading at $F_{HF} =$ 28.9 MJ m^{-2} $s^{-1/2}$ and $F_{HF} =$ 36.2 MJ m^{-2} $s^{-1/2}$. To determine whether this effect is caused by an increased energy absorption leading to an increased surface temperature or whether it is explained by a reduced power handling (i.e. changes in the thermal properties of the surface), the fractional temperature increased is corrected using the total reflectivity values for damaged tungsten obtained by ellipsometry measurements shown in figure

4.3. The results of this can be found in figure 4.19.

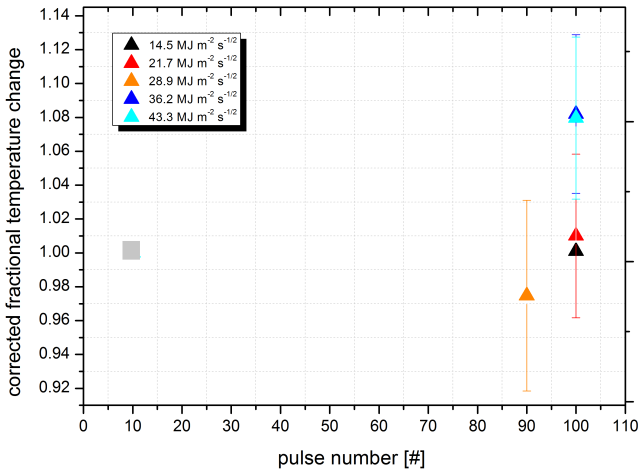

Figure 4.19: Fractional change in ΔT after exposing to 100 pulses. A correction for changes in absorptivity of the modified surface is applied on the experimental values shown in 4.18.

From this correction, it is found that the change in ΔT of the most dramatic case ($F_{HF} = 28.9$ MJ m^{-2} $s^{-1/2}$) can be attributed to gradual increase of laser energy. However, for the cases of $F_{HF} = 36.2$ MJ m^{-2} $s^{-1/2}$ and $F_{HF} = 43.3$ MJ m^{-2} $s^{-1/2}$, ΔT is increasing by more than 8% during the course of 100 pulses, indicating a reduced power handling capability of the tungsten surface. By comparing these results with surface morphologies shown in figures 4.12 and 4.13, the onset of melting and re-solidification processes at these loading conditions can be explained. Due to a reduced power handling, protruding grains at the surface (hot spots) get extra heated, hereby passing the melting threshold of ~3422 °C whereas the average surface temperature at the irradiated zone is below this: ~2450 °C in the case of $F_{HF} = 36.2$ MJ m^{-2} $s^{-1/2}$ and ~2700 °C for $F_{HF} = 43.3$ MJ m^{-2} $s^{-1/2}$ (see figure 4.17).

For high pulse numbers (>1000) and $F_{HF} = 37.5$ MJ m^{-2} $s^{-1/2}$, a steep increase in ΔT is observed for subsequent laser pulses. For the sample loaded at 1000 pulses (fig. 4.7), the peak temperature is found to increase 1600-2650 °C per laser pulse. For loading to 5000 pulses, this set and subsequent 4000-5000 pulses on the same position are shown in figure 4.20. The temperature evolution during pulse 1000-4000 is unfortunately not recorded due to wrong settings of the IR camera. Since the surface at this position is heavily damaged, specular reflectivity is negligible (fig. 4.2a) and ellipsometry could not be performed. Therefore, no value for the total reflectivity after applied loading is obtained and no correction is applied for increased absorptivity. From 1D model calculations, a relative increase in absorptivity of ~25 % between the 1st and last pulse would be needed to explain the behaviour shown in figure 4.20. This is a high number compared to the maximum relative change in absorptivity found in the powerscan (12 %). Therefore, a strong degradation of power handling due to cracks and severe roughening is likely to be causing the high surface temperatures. However, by examining the transient temperatures in figure 4.20, a saturation in ΔT is observable. As can be seen from SEM (fig. 4.8), the surface is heavily melted and eroded. The absorbed energy causes a phase transition into the liquid state and is converted into radiation which becomes more important at these elevated temperatures. The cool-down time (τ_e), which is defined as the time it takes before the peak temperature has decreased to a fraction $e^{-1} \approx 0.37$ of its maximum value, is increasing gradually with pulse number at this heat load. As opposed to this, τ_e is found constant in the case of applying 100 pulses.

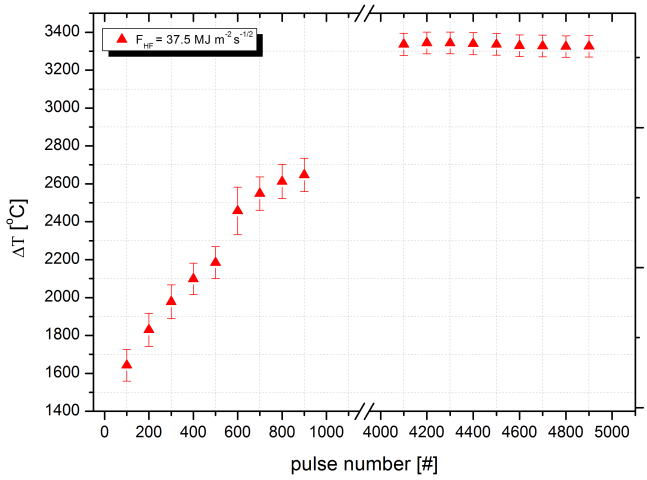

Figure 4.20: Temperature increase in centre of loaded area for subsequent laser pulses. The evolution between 1000 and 4000 pulses could not be displayed as a consequence of IR camera failure. A saturation in peak temperatures at the surface for pulse numbers above 4000 can be seen.

4.4 Conclusions and discussion

Temperature evolution and damage caused by laser loading on actively cooled pristine tungsten targets in absence of a plasma is assessed at heat loads of 14.5-43.4 MJ m^{-2} $s^{-1/2}$ (power density: 0.46-1.37 GW m^{-2}) and pulse numbers 1-5000. For heat loads >37.5 MJ m^{-2} $s^{-1/2}$ and $\geq$100 pulses, melting was observed. Cracking was only observed for $\geq$1000 pulses and is preceded by melting. The peak surface temperature during transients is linearly proportional to the heat load parameter of the applied laser pulses as is experimentally confirmed (fig. 4.17).

Likewise, grain growth is found to occur linearly with increasing heat load. Also, increased pulse number led to increased average grain size. Even for single pulse exposure, immediate recrystallization is observed, indicating that these processes occur on the microsecond timescale. The mean arithmetic roughness (R_a) showed similar trends although showed very large increase in the case of melted spots since material is displaced towards the edges.

Direct reflectivity of light of 300-800 nm decreases to 10% of the original reflection as pulse number and heat load increase. As the surface gets more roughened, light is increasingly reflected and scattered in a diffuse way. Ellipsometry measurements revealed a relative shift in total reflectivity at 1064 nm up to 12% compared to pristine reflectivity. By correcting the measured transient temperature increase per pulse (relative shift in ΔT compared to first pulse applied) by an increase in surface absorptivity at the damaged surface, a maximum rise in ΔT over the succession of 100 pulses up to 8% compared to the first pulse is found. This indicates reduced power handling capabilities of the W surface for heat loads >37.5 MJ m^{-2} $s^{-1/2}$. The same effect, although much stronger, is observed in the case of 5000 pulses. Due to severe roughening, melting and the occurrence of deep cracks (fig. 4.8), ellipsometry data could not be obtained at this damaged location and hence no correction for enhanced laser light absorptivity could be accounted. It is assumed that the presence of cracks are responsible for a strong increase in absorptivity since light can be trapped at such locations. By comparing the measured change in ΔT with the input power density that is necessary for this from the 1D model (eq. 2.2), a total absorptivity of 75 % would be needed. In that case, the affected spot would look very dark which is not the case. It is possible that this high absorptivity is reached within cracks (without being resolved by the IR-camera), causing severe melting around it as is indeed confirmed by SEM analysis. On the

other hand, areas within the damaged zone but of larger spatial distance from cracks are melted too, indicating local decreased power handling capabilities of the surface.

Although trends in temperature evolution are mapped out in the previous section with good reliability as the temperature evolution of a few fixed pixels is recorded over time, the absolute temperatures obtained from analyzing IR data is not in all cases. The IR camera operates using a filter which prevents the device from saturating during the transient. Peak temperatures are recorded accurately when using this but temperatures <200 °C are not, which limits proper recording in the lower temperature regime which is a problem when analyzing the cool-down shape below this temperature threshold. In the case of 1000 pulses, a temperature mismatch is found when comparing the peak temperatures with the temperatures from the power scan mentioned in figure 4.17 at equal laser power. In the analysis process, the temperature evolution is obtained by converting the photon count of a few collecting pixels on the camera positioned on a line to temperature of the emitting surface. The temperature during the first hundreds of pulses of a total of 1000 seem to low, indicating that these pixels are not properly aligned with the maximum of the heated surface. It may well be the case that the location at the sample representing the maximum temperature changes over time where the collecting pixels or positioned at a fixed location.

Besides, although temperature dependent emissivity values are used for temperature analysis, the influence of surface roughening on emissivity are not taken into account. Relative changes in emissivity for a recrystallized surface have been measured before, yielding only a few percent change after many pulses [24]. However, in the case of shallow melted region, this is unknown. An increased emissivity at the target would lead to an overestimation of surface temperature in the analysis which could explain the peak temperatures during laser loading to exceed the theoretical values (fig. 4.17).

A final remark is there to be made about determining the value of the heat load parameter arriving at the target. As the total energy stored in the laser pulse is divided by the area on the sample to which it is confined, it is proportional to the square of the spot radius, making this the main source of error. The FWHM of the heated area is measured with the IR camera. As the size of the heated surface above a certain temperature may increase due to reduced heat dissipation over time, so is the measured FWHM. In other words, the measured spot size may grow whereas the actual area of loading is not changed. Secondly, as the FWHM of the spot is typically 6-10 pixels, the gaussian shape of the applied heat pulse is represented in a rather coarse way. These factors together yield a maximum spot size error of 19%. For the heat load parameter, including uncertainties in fiber transmission, absorptivity and pulse duration, this means a fractional error of 28%. This value is the maximum fractional error and is different in each case. Error bars for heat load parameters mentioned are omitted for clarity.

The results presented in this chapter will be used as a benchmark when plasma conditions will be added to the system under investigation.

Chapter 5

Laser loading on plasma-exposed samples

The formation of irreversible surface modifications of tungsten exposed to a high flux plasma is known to alter its near surface. Surface damage may degrade the thermophysical properties which can lead to reduced power handling and therefore to a reduction in ELM resistance. Results on the interaction between damaged materials due to deuterium and helium plasmas and transient heat loads are presented in this chapter.

Typical changes in surface morphology after laser loading on samples exposed to a range of deuterium plasma fluences have been carried out by B. Hensen. His work is cited and processed in the next section in order to make comparisons with new data yielding a broader picture of damage creation by ELM loading.

5.1 Deuterium exposed samples

Before laser heating, the surface of samples pre-exposed to a deuterium plasma shows small, rough-shaped blisters for low fluences whereas large ($> 0.1\mu$m), smooth blisters are observed in case of high fluences [14]. Although burst blisters and mass loss through laser loading have not been found, swelling of already existing bubbles is observed. Changes in surface morphology after applying conditions as shown in figure 5.1 are assessed by SEM (fig. 5.2-5.3). A comparison between figures 5.2a and 5.3a which show samples exposed to a similar heat load parameter of ∼18 MJ m^{-2} $s^{-1/2}$ but a difference in fluence of one order of magnitude, reveals additional surface modification due to increased plasma fluence. Apart from roughening and irregularities between adjacent grains, expansion of blisters due to longer exposure duration can be seen. Surfaces loaded at F_{HF} >22.6 MJ m^{-2} $s^{-1/2}$ are roughened to such an extend that individual blisters could not be detected. Most surprising is the observation of cracking at $F_{HF} = 33.6$ MJ m^{-2} $s^{-1/2}$ after only 100 pulses where this did not occur for loading pristine samples. Only after exposing a pristine sample to a set of 1000 pulses at $F_{HF} = 37.5$ MJ m^{-2} $s^{-1/2}$, this effect was to be seen (4.7). Above this, again a fluence effect seems to play a role: no cracking is observed on the pre-exposed sample at $F_{HF} = 36.1$ MJ m^{-2} $s^{-1/2}$ (fig. 5.3d) but this did occur at a slightly lower heat load of 33.6 MJ m^{-2} $s^{-1/2}$ (fig. 5.3b) where the latter position endured a deuterium fluence which is ∼36% higher than the first position where cracking was absent.

Furthermore, when comparing loading at $F_{HF} = 28.2$ MJ m^{-2} $s^{-1/2}$ on a deuterium exposed sample (fig. 5.3e) to irradiation of a pristine sample at similar conditions (fig. 4.11), it can be seen that melting of individual grains sets in at lower applied density for the pre-exposed sample. A possible cause could be overheating of protruding grains or expanded blisters which are absent on the pristine sample.

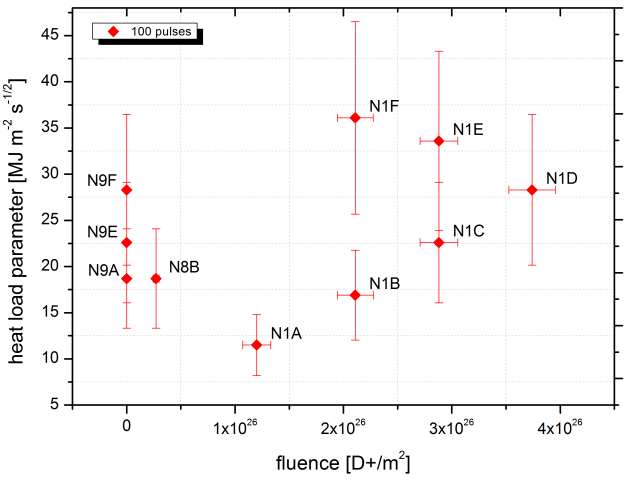

Figure 5.1: Assessed parameter space by B. Hensen. Targets were pre-exposed to a range of deuterium fluences and subsequently loaded to laser pulses. A small increase in surface modifications with fluence for a given laser heat load is identified.

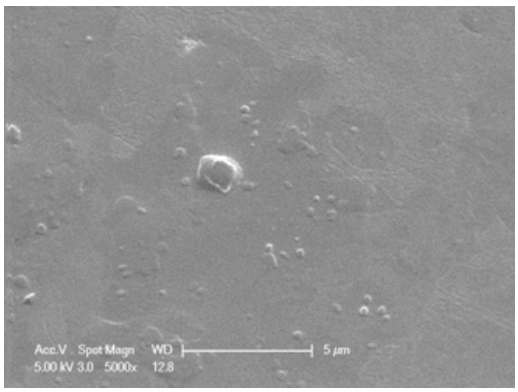

(a) Sample D-N8B. 100 pulses at $F_{HF} = 18.7$ MJ m^{-2} $s^{-1/2}$. Fluence: $2.71 \pm 0.27 * 10^{25}$ D^+/m^2.

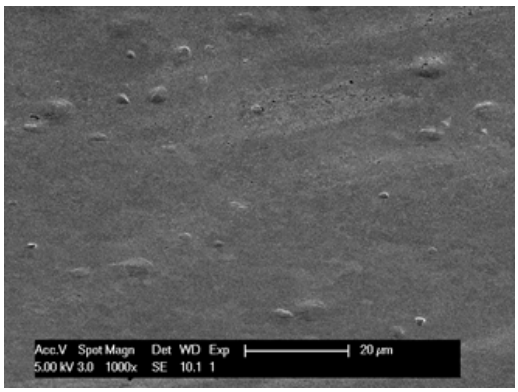

(b) Sample D-N1A. 100 pulses at $F_{HF} = 11.5$ MJ m^{-2} $s^{-1/2}$. Fluence: $1.20 \pm 0.13 * 10^{26}$ D^+/m^2.

Figure 5.2: SEM results of B. Hensen after loading of 100 laser pulses of low power densities on samples pre-exposed to a deuterium plasma with fluences as given. Image b shows blisters of increased size compared to image a, due to an increased fluence by factor 4. The power density of the laser is insufficient to cause roughening and blisters are maintained.

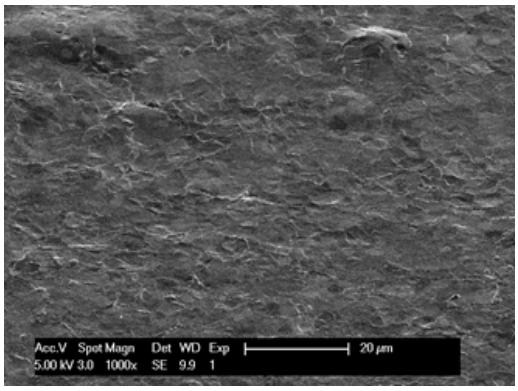

(a) Sample D-N1B. 100 pulses at $F_{HF} = 16.9$ MJ m^{-2} $s^{-1/2}$. Fluence: $2.11 \pm 0.17 * 10^{26}$ D^+/m^2.

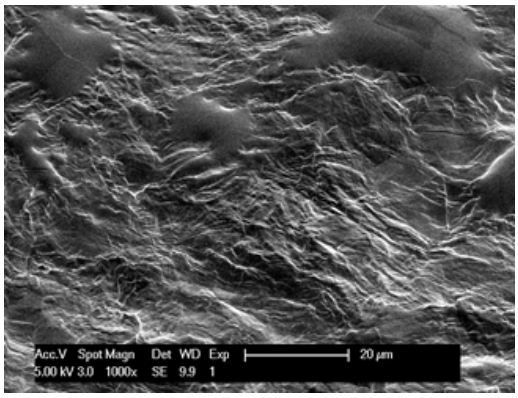

(b) Sample D-N1F. 100 pulses at $F_{HF} = 36.1$ MJ m^{-2} $s^{-1/2}$. Fluence: $2.11 \pm 0.17 * 10^{26}$ D^+/m^2.

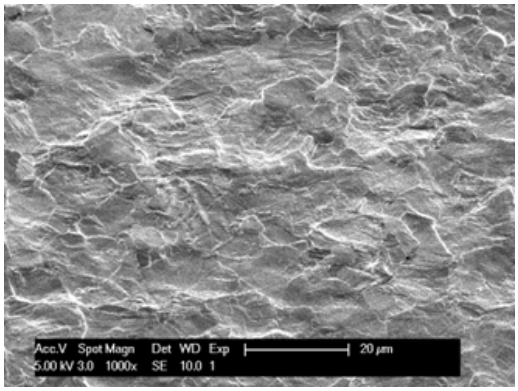

(c) Sample D-N1C. 100 pulses at $F_{HF} = 22.6$ MJ m^{-2} $s^{-1/2}$. Fluence: $2.88 \pm 0.17 * 10^{26}$ D^+/m^2.

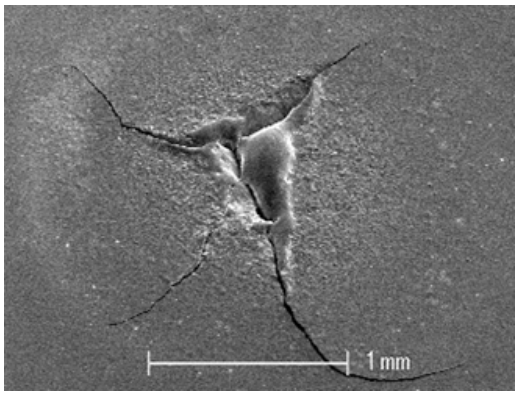

(d) Sample D-N1E. 100 pulses at $F_{HF} = 33.6$ MJ m^{-2} $s^{-1/2}$. Fluence: $2.88 \pm 0.17 * 10^{26}$ D^+/m^2.

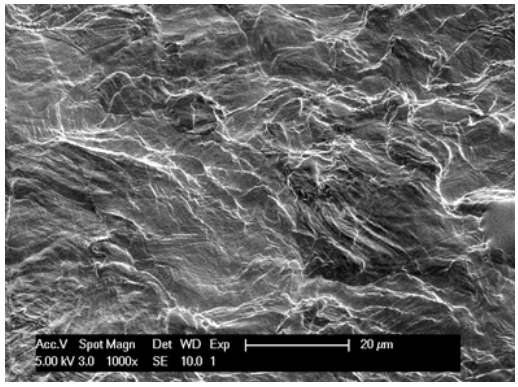

(e) Sample D-N1D. 100 pulses at $F_{HF} = 28.2$ MJ m^{-2} $s^{-1/2}$. Fluence: $3.74 \pm 0.22 * 10^{26}$ D^+/m^2.

Figure 5.3: SEM results of B. Hensen. Pulsed laser loading at $F_{HF} = 16.9$-33.6 MJ m^{-2} $s^{-1/2}$ on targets pre-exposed to deuterium fluences as indicated. Targets were held at room temperature during laser irradiation.

5.2 Helium exposed samples

Although blister formation in hydrogen plasmas is strongly reduced by temperatures typically above 700 °C, the formation of helium bubbles/holes continues due to strong interaction with lattice effects in tungsten [25]. By irradiating samples in Pilot-PSI, nanostructured layers of helium induced tungsten have been formed. The thermal response of such surfaces have been studied by applying laser heat loads on fuzz layers distinguished by exposed helium fluence and surface temperature during formation. The latter stage is executed by positioning the samples after helium exposure in the TEAC of Magnum-PSI.

The three samples investigated are exposed to a maximum fluence of $6.31 * 10^{26}$ He^+/m^2 at ∼1240 °C (He3), $9.97*10^{25}$ He^+/m^2 at ∼1123 °C (He4) and $8.42*10^{25}$ He^+/m^2 at ∼ 300 °C (He5). A bias potential of -38 V is applied on all samples. In the first two cases, the surface is visually black and surface reflectivity is reduced to almost zero. In the case of sample He5, due to low temperature during exposure, the surface did not differ visually from a pristine sample and 56 % reflection at λ=1064 nm is assumed. Both visual pictures of the loaded samples and SEM images of 50.000 times magnification are shown in figure 5.4. As a consequence of lower fluence experienced by sample He4, the formed nanostructures are less dense and slightly smaller than the structures on sample He3. The thickness of the fuzz layer is a function of exposure time while the typical size of the nanostructures is a function of surface temperature during plasma exposure [26]. Therefore, the thickness of the fuzz layer before laser impact is assumed to be largest on sample He3. The thickness evolution with laser power and pulse number is discussed in the next section.

Experimental data of laser loading on the low-temperature sample He5 is limited. The highest heat load applied on this surface is 17 MJ m^{-2} $s^{-1/2}$ which caused an averaged peak temperature over 100 pulses of ∼1440 °C. This temperature is much higher than predicted by the 1D diffusion model (eq. 2.2) which is 960 °C at this laser power when absorption of pristine tungsten of 44% is assumed. Further heat load studies at higher energy densities are to be done in order to investigate whether the creation of He bubbles in the near surface is causing such drastic change in thermal response compared to the case of pristine W.

The pre-exposed samples containing He-induced nanostructures were subjected to a range of transient heat loads. The applied pulse duration was 1 ms in all cases and base temperature of the samples was held at room temperature. An overview of the applied conditions can be found in table 5.1.

sample/position	P [GW m^{-2}]	F_{HF} [MJ m^{-2} $s^{-1/2}$]	pulse number
He3-N	0.27	8.6	100
He3-E	0.55	17.5	100
He3-SE	0.63	19.9	100
He3-S	1.11	35.2	100
He3-SW	0.61	19.4	1.000
He3-W	0.62	19.5	10.000
He4-NE	0.58	18.2	100
He4-N	0.71	22.5	100
He4-NW	1.01	31.8	100
He4-SE	1.04	32.8	100
He4-SW	0.49	15.5	1000
He4-W	0.51	16.2	10.000

Table 5.1: Laser loading conditions on sample He3 and He4. The first one contains a thick nanostructured layer due to helium irradiation. He4 has a similar nanostructured top surface although thinner.

It is expected that the formation of He-induced surface layers lead to reduced thermophysical properties and therefore to higher peak temperatures during transients. In contrast to loading of

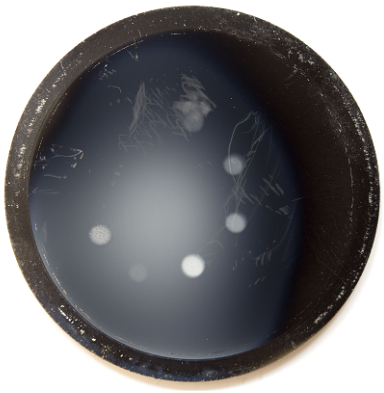

(a) Sample He3, containing damaged spots due to laser impact.

(b) Sample He4 with laser affected spots.

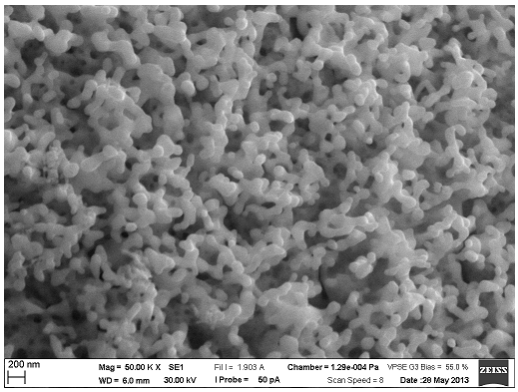

(c) Typical He-induced nanostructures on He3 at 50.000X magnification. Max. fluence: $6.31 * 10^{26}$ he+/m^2, T≈1240 °C.

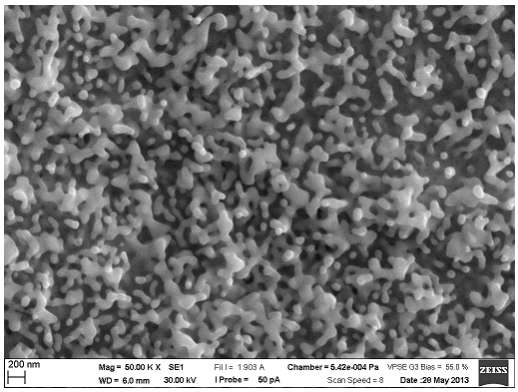

(d) Typical He-induced nanostructures on He4 at 50.0000X magnification. Max. fluence: $9.97 * 10^{25}$ he+/m^2, T≈1123 °C.

Figure 5.4: Visual pictures of laser loaded samples pre-exposed to helium plasma (a, b) and highly magnified SEM images showing He-induced nanostructures (c, d). The fuzz contained by sample He3 seems to be of denser nature and shows taller structures than the ones on sample He4. This is attributed to a lower fluence experienced by sample He4.

pristine samples, the first pulse seems to generate a much higher temperature than the subsequent pulses in the case of an already existing fuzz layer. The columnar He-induced tungsten fibres act as hot spots which causes a steep temperature gradient during loading and high peak temperature, especially for the first pulse where a fraction of the fibers might be annealed. Results on ΔT for both first pulse and pulses averaged versus heat load parameter are shown for sample He3 and He4 (fig. 5.18). For analysis purposes, a constant surface emissivity of 0.8 and unity absorptivity of the laser light is assumed. At this point, the change in emissivity with temperature and thickness of the fuzz layer is unknown. However, retention of the He-induced nanostructures upon laser loading is confirmed, which means that emissivity values for pristine W should not be used either. As the fuzz surface before laser loading is completely black and becomes brighter after applying laser pulses, absorptivity is likely to decrease with the succession of pulses. However, a decreasing thickness of the fuzz layer would lower its emissivity as more of pristine surface is approached. This factor would counter the surface temperature drop caused by decreased absorptivity.

Next to large differences in temperature caused by first and subsequent laser pulses, other differences compared to loading on a pristine surface can be pointed out. First of all, the average

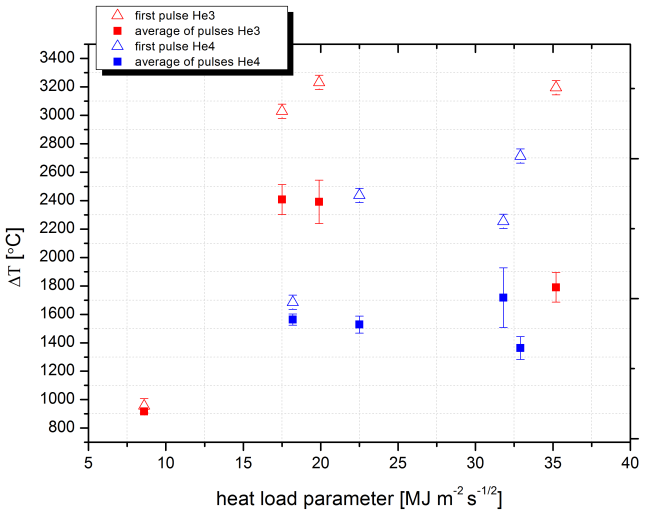

Figure 5.5: ΔT during laser loading for helium-induced tungsten samples. The first pulse generates a much higher surface temperature than subsequent pulses in all cases. Next to this, a saturation in ΔT with increasing heat load parameter is apparent. Absorption and emissivity change as the thickness of the fuzz layer gradually decreases with the succession of pulses, hereby affecting the temperature analysis.

peak temperatures are much higher in the case of a present fuzz layer as is found by comparing figures 4.17 and 5.18. Another interesting difference is the apparent saturation in absorbed power for the He-induced surface. The first pulse imposed on the surface seems to heat up the fuzz layer, ending in the same peak temperature range independent of input power for $F_{HF} > 17$ MJ m^{-2} $s^{-1/2}$ in the case of thick He-induced surface (He3) and for $F_{HF} > 22$ MJ m^{-2} $s^{-1/2}$ in the case of a thin modified surface (He4). The same effect is observed for the averaged subsequent laser pulses.

Next to uncertainties in the change of emissivity with pulse number, the size of the area which absorbs the laser energy is another aspect that complicates the picture. As fuzz can be viewed as a porous top surface of W, the collective area is largely increased compared to a smooth surface, being responsible for a lower power density at given laser power than in the case of a pristine surface without modifications. This is possibly the reason that high temperatures are reached on the fuzz surfaces without destroying the induced nanostructures. As the fuzz layer becomes thinner it is likely that the power density increases and than the disappearance of the layer is accelerated, but this is still to be confirmed experimentally. As initial absorptivity by the fuzz layer is set to unity, it is likely that this will decrease with the succession of pulses since the thickness of the fuzz is gradually reduced. This leads to a decreased actual heat load parameter arriving at the surface. This is further strengthened by the observation that the difference between first and subsequent pulses grows with increasing laser power density since fuzz is annealed to a larger extend (but not entirely removed), leading to decreased absorptivity and thus lower temperature at the target. As is said before, this factor is partly balanced by a reduction in emissivity which leads to a higher temperature.

5.2.1 Surface morphology

Changes in surface morphology of the thick He-induced surface after pulsed laser loading is assessed by SEM imaging. It is observed that the fuzz layer is retained upon laser loading in nearly all cases. However, sub-surface tungsten is found increasingly roughened in proportion to the applied heat load, keeping the columnar nanostructures intact. Only in the case of highest applied heat

load of $F_{HF} = 35.2$ MJ m^{-2} $s^{-1/2}$, fuzz is removed on some isolated areas of typically 10 μm, likely due to annealing (fig. 5.8). On such laser positions, the difference in temperature between the first and subsequent pulses is the largest of all (fig. 5.18). This anomaly is likely to be attributed to a large shift in emissivity from a fuzz surface (0.8) to roughened tungsten (∼0.2) and a drastic change in absorptivity which makes predicting of the actual peak temperature complex. As the W fuzz is partially removed, emissivity is lowered and the actual peak temperature shifts upwards, making the difference between first and later pulses smaller.

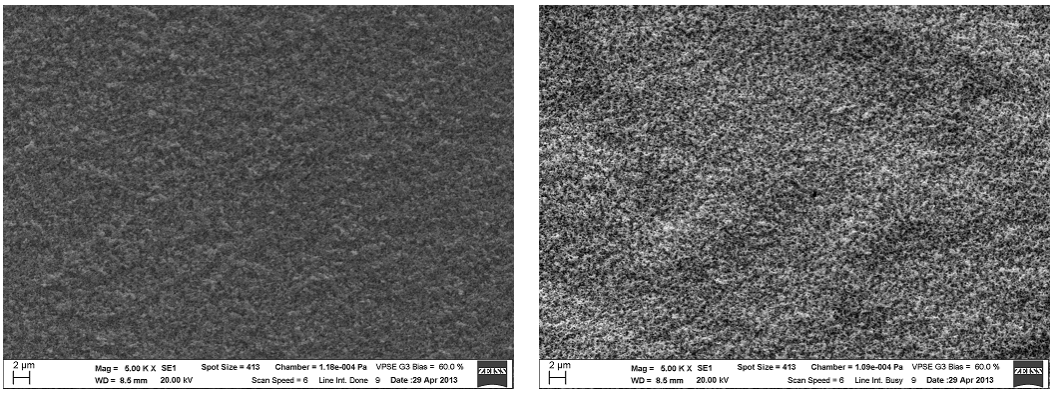

Figure 5.6: He3-N: $F_{HF} = 8.6$ MJ m^{-2} $s^{-1/2}$, 100 pulses. 5000X magnification (l). He3-E: $F_{HF} = 17.5$ MJ m^{-2} $s^{-1/2}$, 100 pulses. 5000X magnification (r).

From previous experiments, the evolution of thickness as function of exposure time at a given base temperature is determined [26]. Sample He3 was exposed for 700 s at an average temperature of 1240 °C yielding a fuzz thickness of ∼2.5 μm prior to laser loading according to this model.

The thickness evolution of the He-induced layer as function of applied heat load parameter is measured by making a depth profile scan along a line through the centre of the affected area by using laser profilometry. Results obtained from positions exposed to 100 pulses on sample He3 are shown in figure 5.9 and indicate a removal rate of fuzz which is linearly proportional to the applied heat load. No measurable changes in thickness of the fuzz layer is found upon loading at $F_{HF} = 8.6$ MJ m^{-2} $s^{-1/2}$. However, for loading at 17.5 MJ m^{-2} $s^{-1/2}$ and 19.9 MJ m^{-2} $s^{-1/2}$, a decrease in fuzz thickness of roughly 1-2 μm is found which is a removal rate of 50-80% relative to the fuzz thickness before laser impact. For the highest applied heat load on the fuzz layer, 35.2 MJ m^{-2} $s^{-1/2}$, removal down to ∼5 μm is measured which exceeds the estimated initial thickness. Complete removal of the nanostructures is revealed by SEM on isolated positions in the centre of this spot.

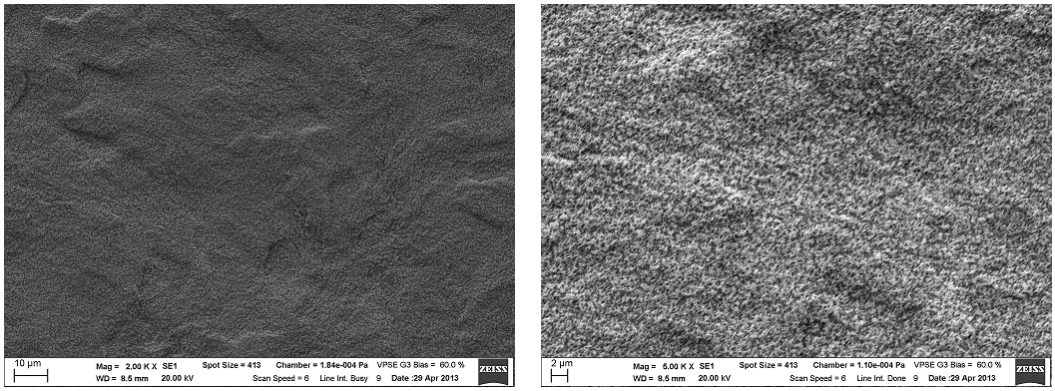

Figure 5.7: He3-SE: $F_{HF} = 19.9$ MJ m^{-2} $s^{-1/2}$, 100 pulses. 2000X and 5000X magnification.

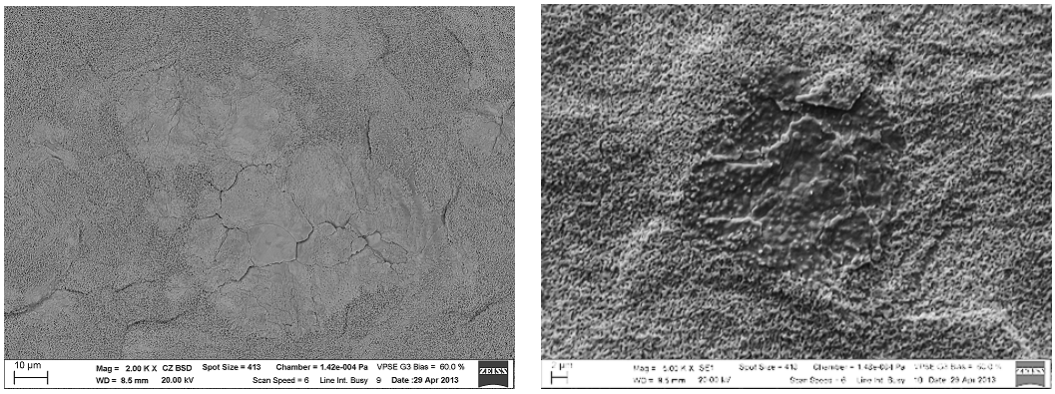

Figure 5.8: He3-S: $F_{HF} = 35.2$ MJ m^{-2} $s^{-1/2}$, 100 pulses. 2000X and 5000X magnification. The He-induced fuzz layer is partially removed in the centre (l) and at some isolated spots (r).

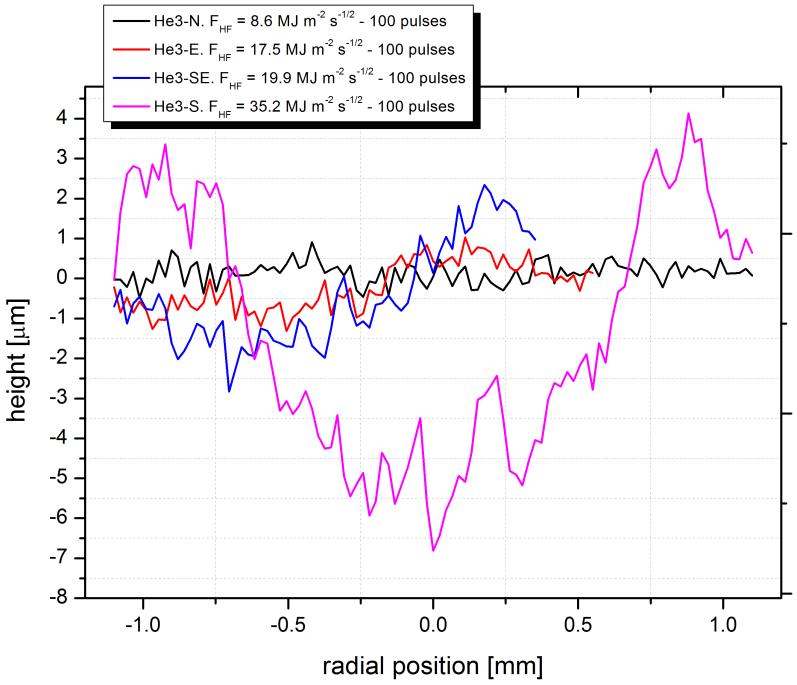

Figure 5.9: Line scan through the centre of the laser spot on the He-induced surface of sample He3. Loading at $F_{HF} = 8.6$ MJ m^{-2} $s^{-1/2}$ does not affect the fuzz layer whereas removal down to 5 μm is found for loading at $F_{HF} = 35.2$ MJ m^{-2} $s^{-1/2}$.

Surface morphology after applying high pulse numbers on tungsten exposed to high helium fluence/high base temperature (sample He3) are shown in figures 5.10 and 5.12. At such high pulse numbers, roughening due to swelling and contracting of the sub-surface continuous. Delaminated and protruded grains are observable even at a moderate heat load of 19.5 MJ m^{-2} $s^{-1/2}$. In the case of 10.000 applied pulses (fig. 5.12), a dense crack network has originated. Surprisingly, He-induced structures are still existing on horizontal surfaces and at sharp edges adjacent to cracks.

A line scan through the centre loaded to 1000 pulses at $F_{HF} = 19.5$ MJ m^{-2} $s^{-1/2}$ is shown in figure 5.11. A decrease in thickness of the fuzz layer on this sample of 4-5 μm was found along with a narrow pit down to $\sim$11 μm which is likely to be a small crack, as it is a much deeper than the estimated fuzz thickness prior to laser impact. The increase in pulse number seems to enhance

the decrease in thickness of the fuzz layer upon comparing with the data shown in figure 5.9.

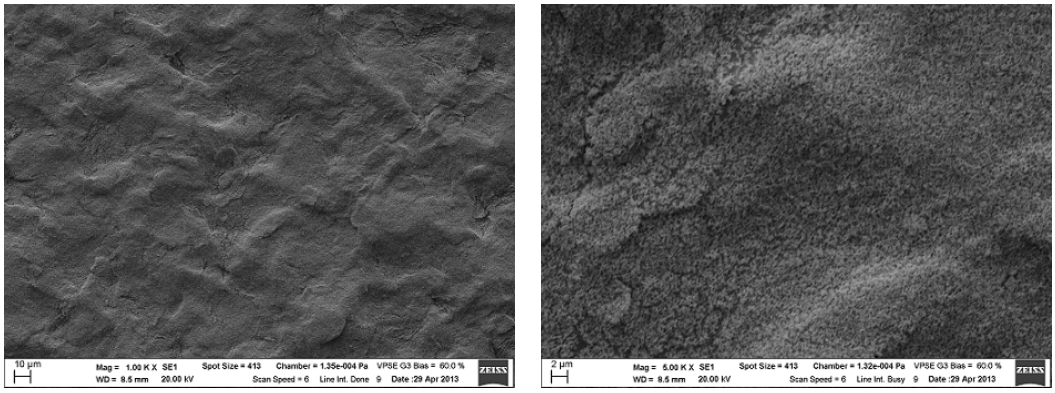

Figure 5.10: SEM images of He3-SW: $F_{HF} = 19.4$ MJ m^{-2} $s^{-1/2}$, 1000 pulses. 1000X and 5000X magnification. No cracking is observed.

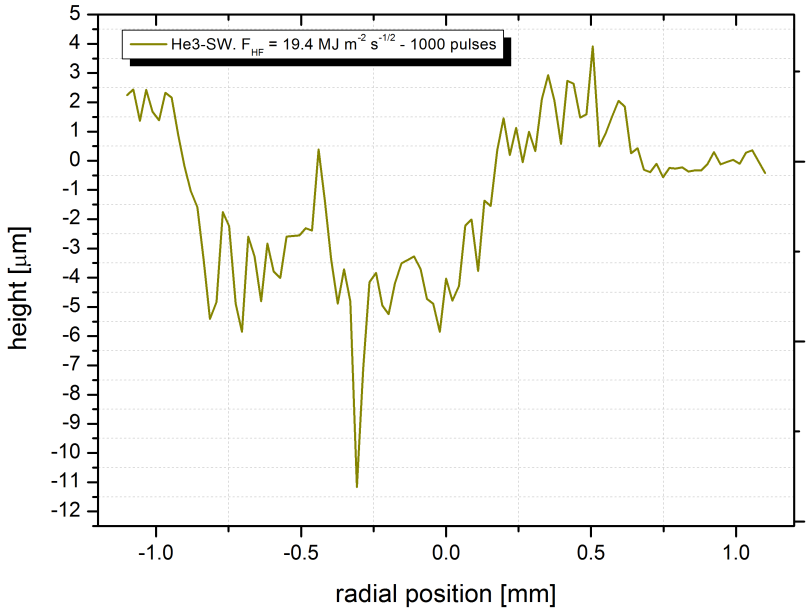

Figure 5.11: Line scan through the centre of the laser spot on the He-induced surface of sample He3 exposed to 1000 pulses at $F_{HF} = 19.4$ MJ m^{-2} $s^{-1/2}$.

Surface damage on sample He4, exposed to a lower fluence and base temperature as mentioned before, is investigated likewise. SEM/BSD results from the performed power scan are presented in figures 5.13-5.16. Similar effects as in the case of sample He3 can be seen, although the boundaries of individual grains containing fuzz are better visible here. The sub-surface roughening increases in proportion with the applied heat load, hereby keeping the fuzz largely intact as seen from the top-views. As in the previous case, it is only removed on isolated grains (not explicitly shown). Morphology changes due to 1000 and 10.000 are shown in figures 5.15 and 5.16 respectively. The onset of cracking is visible as a results of 1000 pulses and, like on sample He3, a dense crack network is found after applying 10.000 pulses (5.16). It is interesting to see the resemblance of

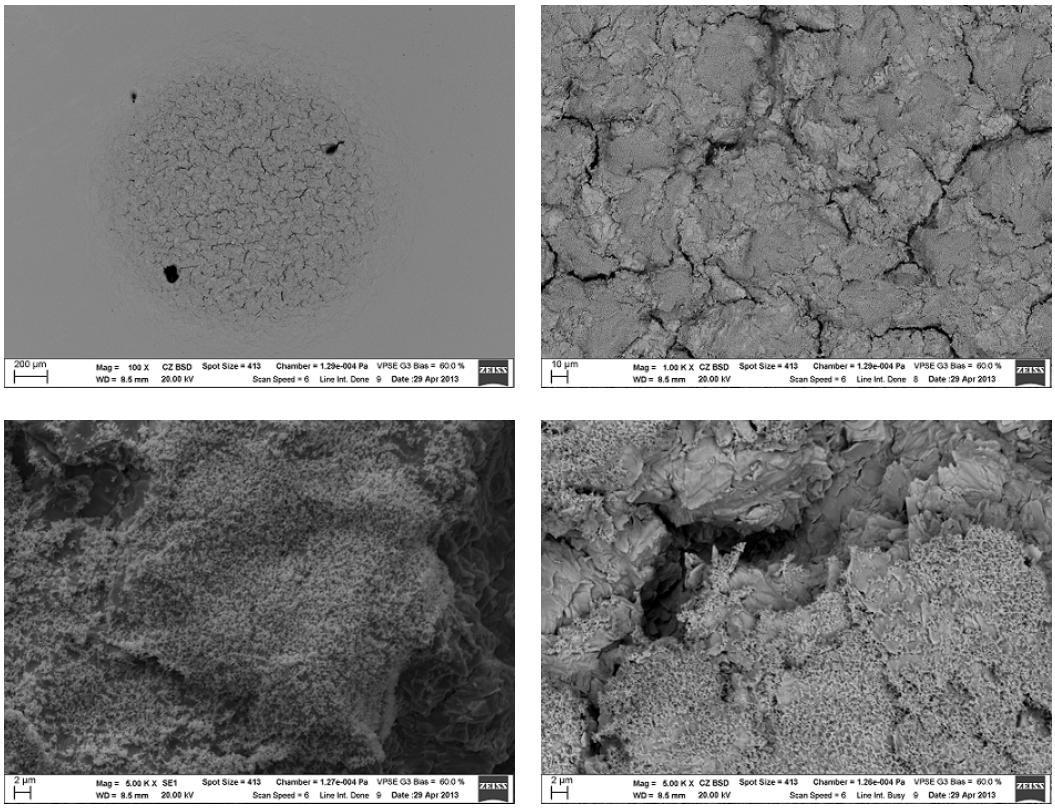

Figure 5.12: He3-W: $F_{HF} = 19.5$ MJ m^{-2} $s^{-1/2}$, 10.000 pulses. 100X, 1000X and 5000X magnification respectively. The formation of a dense crack network is visible, hereby retaining fuzz on sharp ridges. The propagation of damage with pulse number continues at this relatively low heat load parameter.

such crack networks with cracks obtained from electron beam loading [6]. As stated before, the fuzz layer can be viewed as a highly porous W surface, hereby exhibiting effectively a larger irradiated area by the laser than a pristine surface. With this, the laser power density is lowered at given input energy which lowers the temperature gradient in the top (fuzzy) surface. This may prevent the columnar structures from being destroyed. Viewed in this way, the fuzz layer may serve as a guiding channel that spreads the heat uniformly to the sub-surface, keeping its structure intact but leads to additional swelling/roughening of the sub-surface as is found from laser profilometry measurements.

When comparing the arithmetic roughness parameter (R_a) of pristine W subjected to a power scan of 100 laser pulses (fig. 4.14) with the measured R_a of sample He3 containing fuzz after comparable loading conditions, roughness is found to be significantly higher on the He pre-exposed sample in all cases. Results on this are shown in figure 5.17. Local changes in thickness of the fuzz layer depending on the positions within the laser loaded area, for instance at the edge and centre, is not known at this point. Deviations in this may contribute strongly to the increase in roughness compared to a pristine W surface.

Besides, by comparing surface morphologies assessed by SEM after 1000 pulses between both the plasma pre-exposed samples He3 and He4 (figures 5.10 and 5.15), it is notable that the latter seems to be damaged more severely, even at a lower applied heat load on this sample. This is contrasting the observations revealed by surface profilometry from sample He3 and pristine W: as sample He4 exhibits smaller nanostructures, it is likely to behave more like a pristine sample with less surface modifications. As R_a is a measure for the average vertical displacement, it does not take the density of surface modifications into account. It seems that the surface irregularities of He4

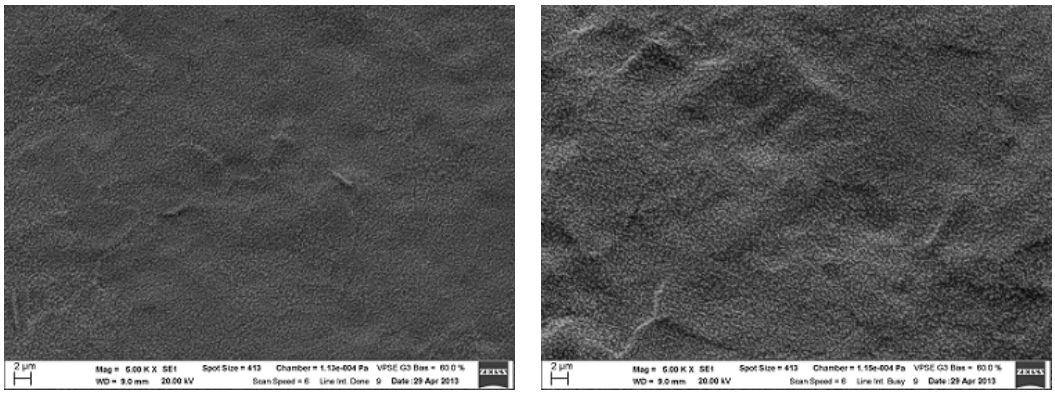

Figure 5.13: SEM/EBSD image of He4-NE: $F_{HF} = 18.2$ MJ m^{-2} $s^{-1/2}$, 100 pulses. 5000X magnification (l). He4-N: $F_{HF} = 22.5$ MJ m^{-2} $s^{-1/2}$, 100 pulses. 5000X magnification (r).

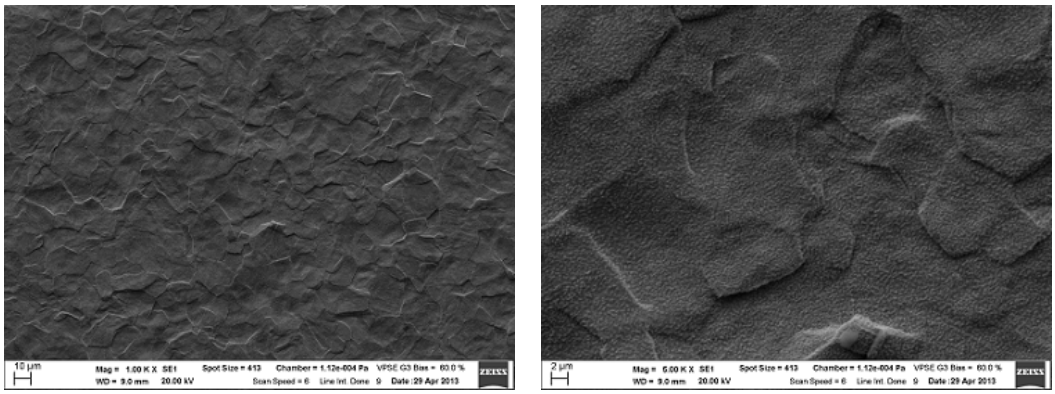

Figure 5.14: He4-SE: $F_{HF} = 32.8$ MJ m^{-2} $s^{-1/2}$, 100 pulses. 1000X and 5000X magnification.

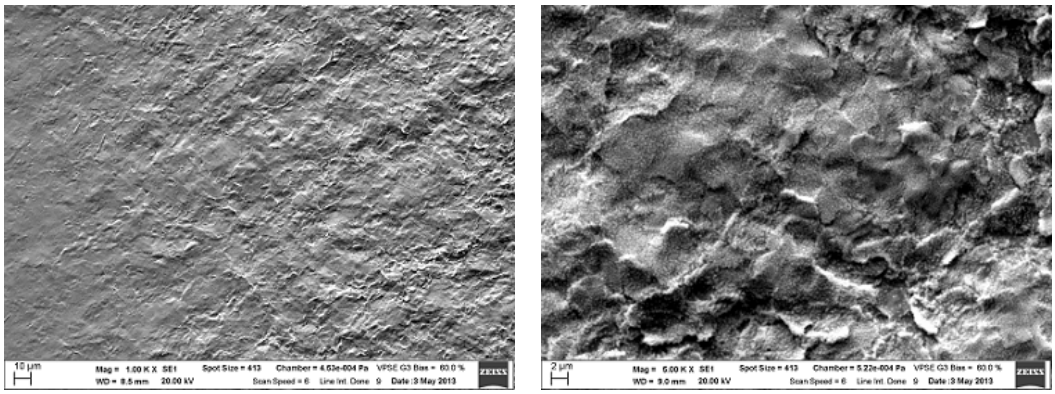

Figure 5.15: He4-SW: $F_{HF} = 15.5$ MJ m^{-2} $s^{-1/2}$, 1000 pulses. 1000X and 5000X magnification. A gradual increase of roughening from the outside towards the centre is visible (l) and remained fuzz is vaguely observable (r). Due to thermal cycling at this high pulse number, grains are protruding and increasingly delaminating.

are of a denser nature than those of sample He3, although exhibiting smaller vertical displacement (hence smaller R_a).

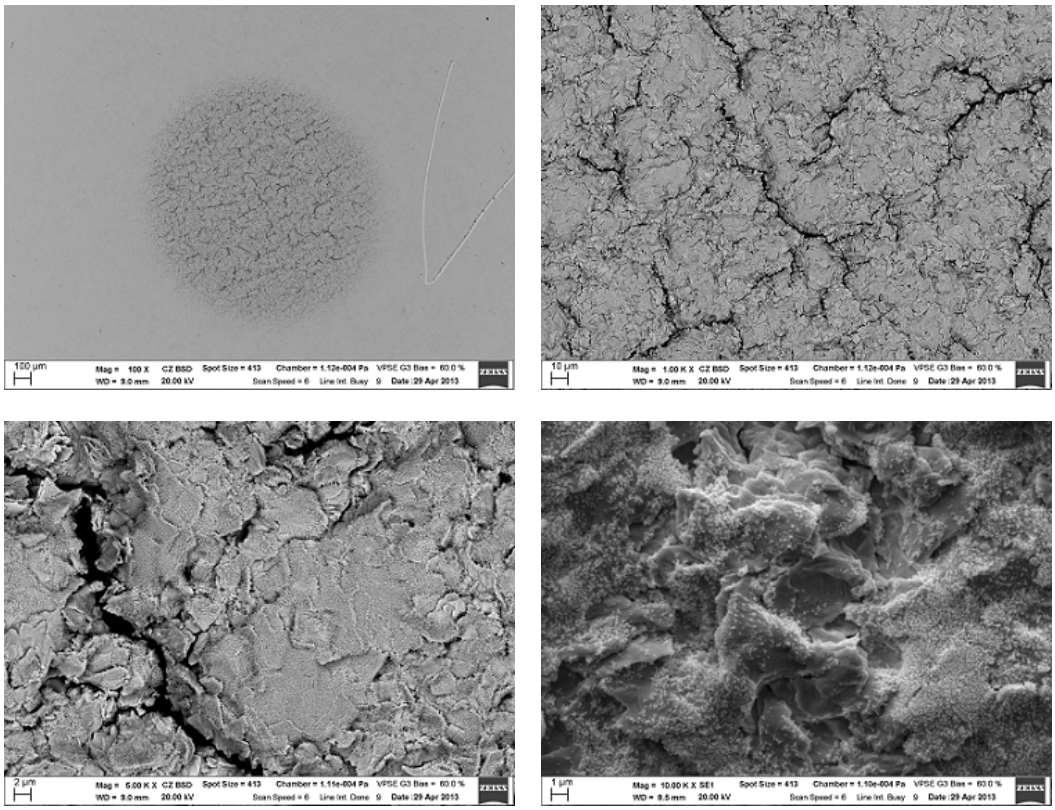

Figure 5.16: SEM/EBSD images of centre of laser loaded area He4-SE, damaged by 10.000 pulses at $F_{HF} = 16.2$ MJ m^{-2} $s^{-1/2}$at 1000X and 5000X magnification. Although less pronounced as on sample He3, fuzz is largely retained on severely roughened sub-surface despite the high pulse number. In the case of 10.000 pulses, the surface shows a rather dense crack network. Nanostructures are retained on sharp edges but disappear on protruded underlying grains.

5.2.2 Power handling

Similar as in the case of loading on pristine samples, power handling of the present fuzz layers is studied. The fractional change in ΔT between first and subsequent pulses for a set of 90 pulses are shown in figure 5.18. The first 10 pulses are omitted in order to make a valid comparison with the pristine case, hereby evading the first pulse on the fuzz surface which causes a much higher temperature than following pulses. It can be seen that ΔT decreases with the succession of pulses for all but the lowest applied heat load of 8.6 MJ m^{-2} $s^{-1/2}$ (fig. 5.18a). Since ΔT is constant for this condition, it is assumed that absorptivity and emissivity is constant for subsequent pulses. In the other cases, the decrease in ΔT can be explained by a gradual shift from unity absorptivity towards $\sim$0.5 of pristine W along with at shift in emissivity. Fuzz is found to be partly annealed in the case of loading at $F_{HF} = 35.2$ MJ m^{-2} $s^{-1/2}$and is completely retained in all other case. Therefore, finding realistic values of the change in emissivity and absorptivity after a set number of pulses is complex. Additional experiments to verify changes in emissivity and absorption of the fuzz layer are necessary in order to completely understand power handling.

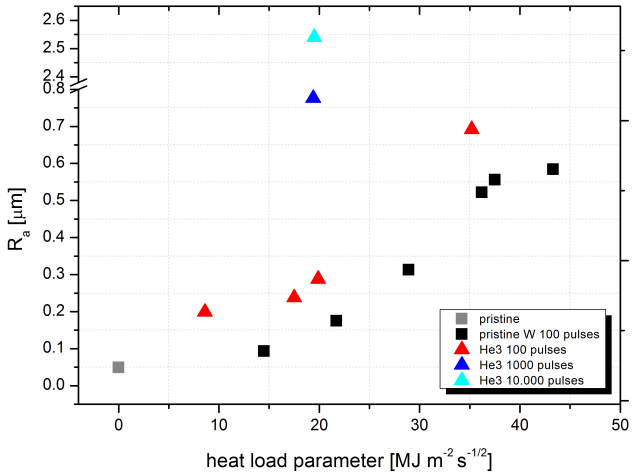

Figure 5.17: Roughness parameter R_a of pristine samples and pre-exposed sample He3 as function of applied heat load. Points indicating roughness of pristine samples for 1000 and 5000 pulses are omitted for clarity but shown in figure 4.14. Samples containing a nanostructured surface exhibit a larger R_a upon laser loading than pristine samples at all conditions. R_a increases linearly with heat load parameter for both laser loading on pristine samples and samples containing a He-induced surface. Furthermore, R_a increases progressively with pulse number at a fixed heat load.

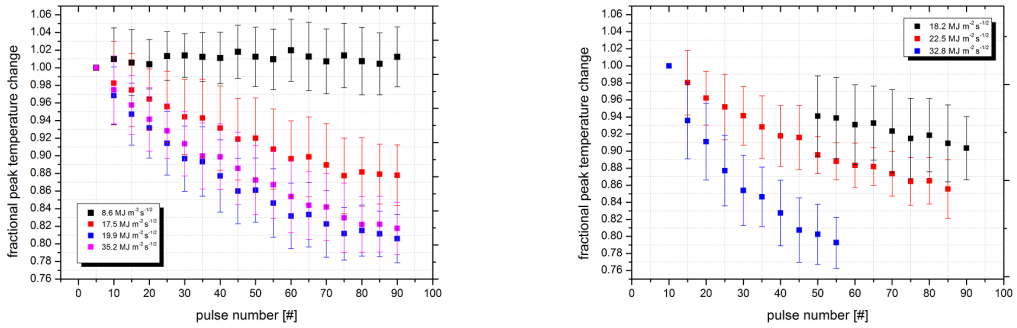

(a) Sample He3.

(b) Sample He4.

Figure 5.18: Change in peak temperature with the succession of 90 pulses, normalized to the first set of 10 for He3 (a) and He4 (b) at fixed emissivity of 0.8 and unity absorptivity. Loading at F_{HF} >16 MJ m^{-2} $s^{-1/2}$ leads to a decrease in ΔT for progressing pulses. This is explained by a decrease in absorptivity of the fuzz layer and a shift in emissivity to lower values.

5.3 Conclusions and discussion

This chapter dealt with the thermal response to pulsed heat loads of targets pre-exposed to deuterium and helium plasmas. Deuterium exposed samples, containing blisters, were found increasingly susceptible to the occurrence of damage compared to pristine W. For heat loads up to 16.9 MJ m^{-2} $s^{-1/2}$, blisters were retained within the irradiation zone and were found to expand as function of fluence. The onset of melting decreased to loading at $F_{HF} = 28.2$ MJ m^{-2} $s^{-1/2}$ and the occurrence of deep cracks at $F_{HF} = 33.6$ MJ m^{-2} $s^{-1/2}$ for only 100 pulses confirmed diminished strength along grains. Although being a small effect, an increase in surface modifications

assessed by SEM with increasing fluence at fixed laser power and pulse number was observed.

Helium induced nanostructures have been created at the surface of W samples after exposing to high fluences at surface temperatures >1100 °C. Laser loading studies have been conducted on these surfaces leading to the main conclusion that the fuzz layer thickness is decreasing proportional to the applied heat load, whereas increasing pulse number has only a small effect. Complete removal of the initial fuzz was only observed on isolated positions upon loading 100 pulses at $F_{HF} = 35.2$ MJ m^{-2} $s^{-1/2}$.

Furthermore, the sub-surface W is found increasingly roughened in proportion to both the applied heat load and pulse number, leading eventually to the formation of a dense crack network after 10.000 pulses at $F_{HF} = 15.5$ MJ m^{-2} $s^{-1/2}$. Cracking can be explained by a fatigue effect due to swelling and cool-down of sub-surface grains during thermal cycling at high pulse numbers, keeping the nanostructured surface largely intact.

Moreover, additional damage due to presence of the fuzz layer compared to a pristine surface is confirmed. The arithmetic roughness of He-induced surfaces is found to be higher for all loading conditions (fig. 5.17). This is in line with the observation that the surface temperatures reached on the fuzz layer is much higher for the first pulse applied. As fuzz is largely retained despite the high temperature, it is responsible for an enhanced absorptivity of the laser light, leading to additional sub-surface modifications. Next to this, as the columnar structures can be regarded as a porous top W surface, the power density at this layer is lowered at given laser power which prevents the structures of being destroyed. High peak temperatures may lead to annealing which decreases the thickness of the layer over time. Changes in absorptivity and emissivity with progressing pulses is verified by analyzing the evolution of ΔT with the succession of pulses (fig. 5.18). However, finding the exact values in order to asses power handling capabilities of the fuzz layer is not possible at this point.

Due to a very limited data set on the effect of laser loading on low-temperature He pre-exposed surfaces is a direct comparison with Deuterium pre-exposed samples not possible at this point. However, the average peak temperature after loading 100 pulses at $F_{HF} = 17$ MJ m^{-2} $s^{-1/2}$ was $\sim$1440 °C which exceeds the predicted temperature from the 1D heat conduction model (eq. 2.2) by almost 500 °C. Further experiments are to be conducted to investigate the thermal response of a low-temperature He-induced W surface.

Chapter 6

Simultaneous hydrogen plasma and pulsed laser exposure

In ITER, transient heat- and particle fluxes will be imposed on top of steady state heat fluxes striking the divertor. As is mentioned before, synergistic effects between transient events and the pre-existing steady state plasma are expected. In order to imitate these conditions as close as possible, experiments were carried out by exposing W samples to pulsed laser heat loads combined with a simultaneous high flux hydrogen plasma. A typical temperature evolution obtained from IR imaging is presented in figure 6.1. Apart from interactions between plasma species and the W

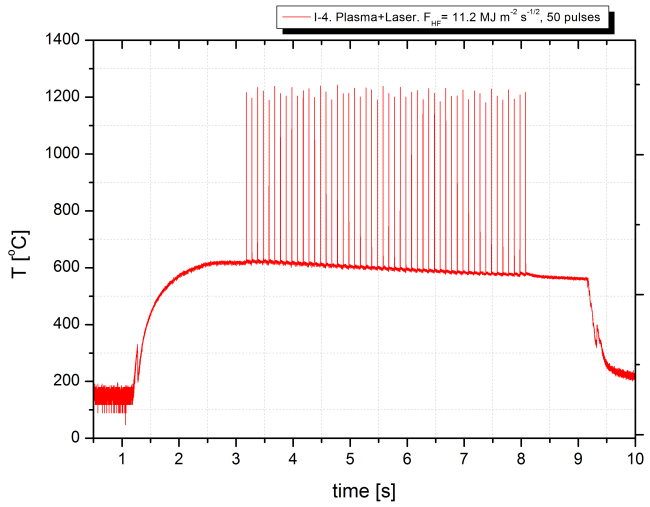

Figure 6.1: Typical temperature evolution of simultaneous plasma and pulsed laser exposure. The total shot lasts 10s were 50 ELMs are loaded within 5s (10 Hz).

surface, the existing heat flux during exposure leads to an elevated base temperature of several hundred °C. Because of this, the surface temperature is above DBTT during the applied transients and is only crossed during the start-up and cool-down phase of the plasma. Since W behaves in a ductile way during the applied transients, the thermal response is different from the case of loading on samples held at room temperature (as described in chapters 3 and 4). To be able to distinguish between the effect caused by particle-surface interaction and the effect caused by an elevated base temperature on damage formation, experiments on a heated sample in absence of plasma were carried out.

Experimental conditions such as laser power density, heat load parameter, pulse number and base temperature (due to plasma) are stated in table 6.1. All targets were actively cooled and biased to -38 V. The total hydrogen fluence that is received by the sample at the laser spot area is found in table 6.2. By applying a poor thermal contact between the sample and cooling structure, high base temperatures above 1500 °C were reached on samples 9 and 10. In this way, a shallow contiguous melt layer is formed as a consequence of laser impact. Results and a discussion on this topic can be found as an appendix.

sample	**P [GW m^{-2}]**	**F$_{HF}$** [MJ m^{-2} $s^{-1/2}$]	**pulse number**	**T$_{base}$** [°C]
I-6	0.16	13.9	100	240
I-7a	1.02	32.2	100	240
I-4	0.35	11.2	100	450
I-5	0.80	25.2	100	450
II-2b	0.34	10.6	1000	300
II-2a	0.47	15.0	1000	300
II-1c	0.17	5.4	1000	600
II-1b	0.33	10.6	1000	600
II-1a	0.48	15.1	1000	600
9 (shallow melting)	0.90	30.7	120	1560
10 (shallow melting)	1.00	39.8	45	1940

Table 6.1: Laser loading conditions and base temperature during simultaneous plasma and laser exposures. All targets were actively cooled and a bias voltage of -38 V is applied. The laser pulse duration and frequency were 1 ms and 10 Hz respectively (except for sample 10: 1.5 ms and 5 Hz). Experiments on samples 9 and 10, subjected to high laser power during high base temperature are described in the appendix.

sample	**fluence [H$^+$/m^{-2}]**
I-4	$1.37*10^{25}$
I-5	$1.24*10^{25}$
I-6	$3.86*10^{24}$
I-7a	$4.6*10^{24}$
II-1b	$1.26*10^{25}$
II-1a	$1.16*10^{25}$
II-1c	$1.48*10^{25}$
II-2b	$8.46*10^{24}$
II-2a	$1.47*10^{25}$
9 (shallow melting)	$9.12*10^{25}$
10 (shallow melting)	$7.62*10^{25}$

Table 6.2: Total hydrogen fluence received by the sample at the location of the laser spot.

6.1 Surface morphology

6.1.1 SEM results

SEM results of samples I-6, I-7a, I-4 and I-5, exposed to simultaneous plasma and 100 laser pulses, are presented in figures 6.2-6.5. Although the effect of plasma presence is not directly visible from

these images, traces of melted areas within the irradiation zone (figures 6.3 and 6.5) at moderate heat fluxes of $F_{HF} = 32.2$ MJ m^{-2} $s^{-1/2}$ and $F_{HF} = 25.2$ MJ m^{-2} $s^{-1/2}$ reveal a different damage mechanism at work. Individual grains having reduced thermal conductivity due to surface modifications are observed to melt where the average peak temperature at the surface is ∼2100 °C which is far below the melting threshold of tungsten (3422 °C). Although this effect is observed on pristine samples in absence of plasma as well, the temperature threshold of localized melting is found to be lowered as a consequence of simultaneous plasma exposure during laser loading.

This effect is apparent when comparing surface modifications of the spot on the pristine sample without plasma loaded at $F_{HF} = 36.2$ MJ m^{-2} $s^{-1/2}$ (fig. 4.12) to surface modifications caused by loading in presence of plasma (fig. 6.3), as these positions developed equal peak temperatures at the surface and were loaded with the same number of pulses. Both targets were heated up to ∼2100 °C during the first pulse. In the course of 100 pulses, the peak temperature increased to 2350 °C for the pristine case and to 2440 °C in the case of simultaneous plasma presence. The areas that melted on the sample loaded only to laser pulses where limited to a few isolated grains of typically ∼20 μm. For the sample that was simultaneously exposed to plasma, the melted area formed a consecutive patch of ∼100 μm diameter. As the plasma exposed target is additionally subjected to a steady-state heat flux, the cool-down time of the surface is found to be increased compared to the case without plasma. In addition to that, the relative temperature rise in ΔT between first and last pulse is ∼30% higher for the plasma exposed sample. These two factors are expected to contribute to the increase of the melted area. It is imaginable that a synergistic effect of the plasma presence affects grain kinetics connected with the phase transition next to this, but conclusions on this are not within reach at this point.

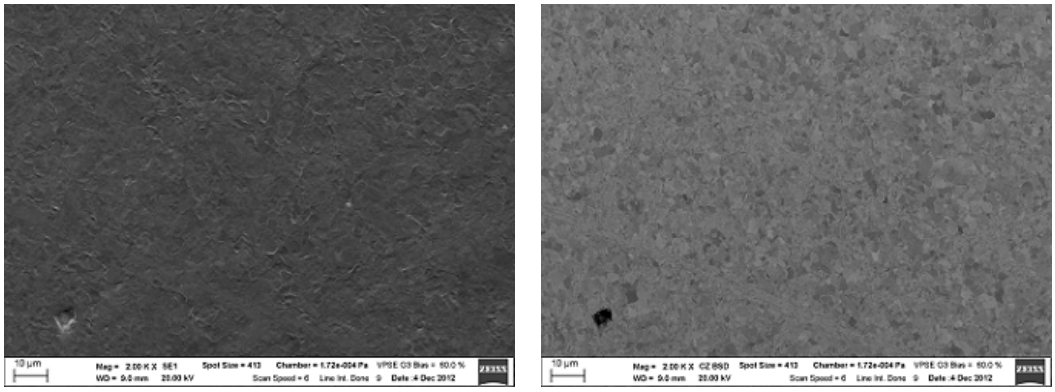

Figure 6.2: Secondary electron image (l) and backscattered electron image (r) of laser spot position after 100 pulses combined with plasma at $F_{HF} = 13.9$ MJ m^{-2} $s^{-1/2}$ and $T_{base} = 240$ °C. No difference from the case of laser only irradiation is identified. Average peak temperature: 1033 °C.

SEM results of sample II-2a, subjected to 1000 pulses at $F_{HF} = 15.0$ MJ m^{-2} $s^{-1/2}$ and $T_{base} =$ 300 °C is shown in figure 6.6. In contrast to the case of 100 pulses without plasma for the same heat load (fig. 4.9) where barely any morphology changes are discernable, the irradiated zone here shows a dense region of small deformed structures. Despite the fact that the base temperature is well above DBTT, strong surface irregularities have been formed due to thermal cycling at this high pulse number. Sample II-2b, exposed to 1000 pulses at $F_{HF} = 10.2$ MJ m^{-2} $s^{-1/2}$ and similar plasma conditions, showed only marginal surface modifications compared to the pristine case and is therefore not explicitly shown.

In contrast to previous samples, the influence of the plasma is clearly visible for the samples at $T_{base} = 600$ °C by the formation of blisters of typically 1-5 μm. The blisters that are shown in figure 6.7 are observed at the edge of the laser irradiated zone of II-1a and are assumed to be equally distributed in size and number at equal radial distances from the plasma column. Therefore, blisters are expected to have been formed likewise at the centre of the laser irradiated zone but could not be detected in all cases due to surface roughening after laser loading.

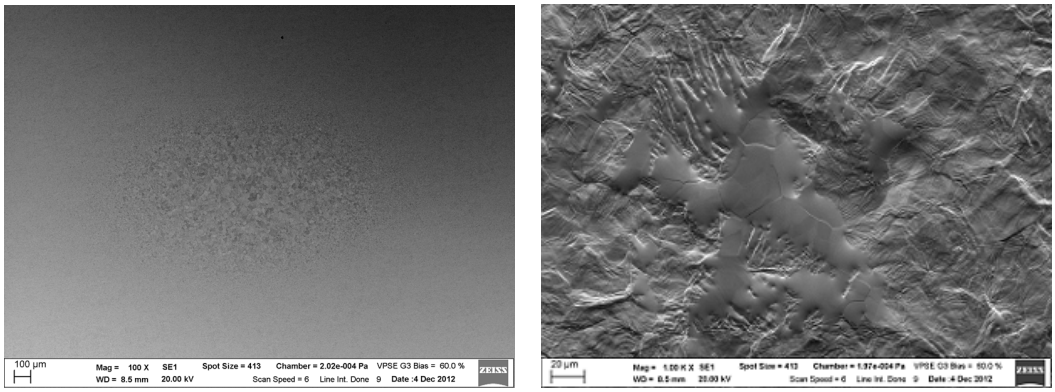

Figure 6.3: Surface morphology after 100 pulses at $F_{HF} = 32.2$ MJ m^{-2} $s^{-1/2}$ and $T_{base} = 240$ °C with simultaneous plasma exposure. A strong gradient in grain size from the edge towards the centre can be observed (l). The onset of melted grains is visible (r). Average peak temperature: 2257 °C.

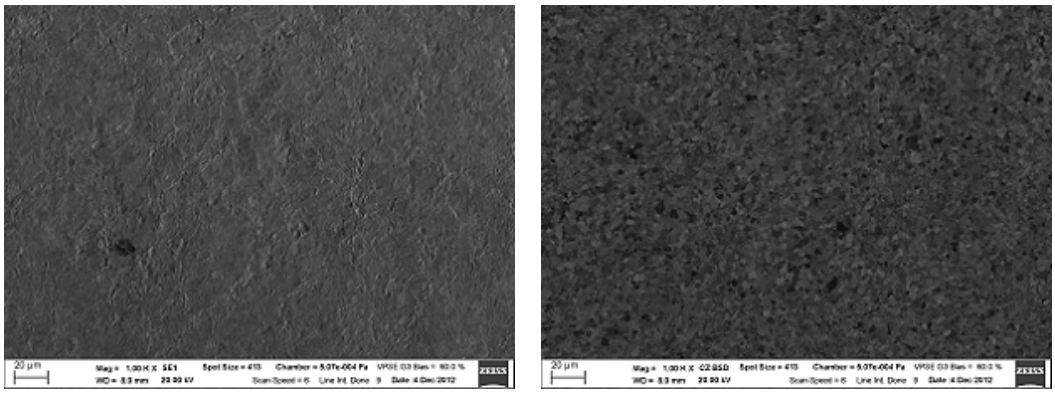

Figure 6.4: 100 pulses at $F_{HF} = 11.2$ MJ m^{-2} $s^{-1/2}$ and $T_{base} = 450$ °C. Only slight roughening is observed and no difference to the laser only case is observed. The average grain size is found to be equal to the pristine case (r). Average peak temperature: 1218 °C.

For 1000 pulses at $F_{HF} = 10.6$ MJ m^{-2} $s^{-1/2}$, the surface is only slightly roughened, hereby maintaining some of its blisters after laser impact (fig. 6.8). Although the surface roughening is only small, it is of a different scale compared to laser only loading where hardly any irregularities are visible by SEM at this heat load condition (fig. 4.9). The roughness after applying 1000 pulses with simultaneous plasma exposure as shown in figure 6.8, might be attributed to overheated blisters that leads eventually to bursting. It is interesting to see that some blisters are maintained during laser loading, even within the centre of the irradiation zone. Also, these blisters might have been formed near the end of the plasma exposure phase.

The surface morphology after 1000 pulses at $F_{HF} = 15.1$ MJ m^{-2} $s^{-1/2}$ is revealed in figure 6.9. Due to the roughened surface visible here, it is not clear whether the blisters that are found at the edge of the laser loading area (fig. 6.7), are maintained upon laser loading. Nevertheless, these sub-surface bubbles of pressurized gas seem to affect power handling. This effect is further explored in a later section of this chapter, dealing with measured surface temperature evolution.

6.1.2 Recrystallization kinetics

When measuring the size of grains in the centre of the loaded area that is exposed to plasma and laser simultaneously, a distribution proportional to the peak temperature similar to the case of

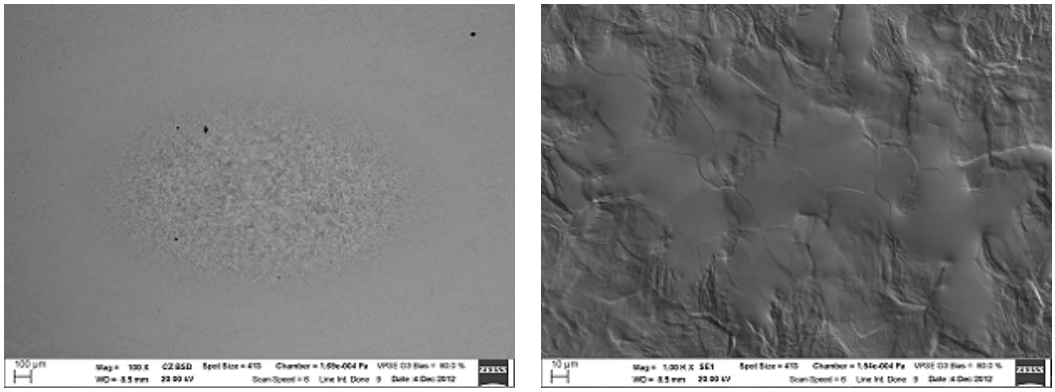

Figure 6.5: 100 pulses at $F_{HF} = 25.2$ MJ m^{-2} $s^{-1/2}$ and $T_{base} = 450$ °C. Average peak temperature: 2439 °C. The distribution of larger grains in the centre compared to the surrounding area (l) and a region of melted grains (r). In the case of only laser irradiation (compare fig. 4.11), no melting is observed at this moderate heat flux which shows the effect of the plasma presence on the onset of melting.

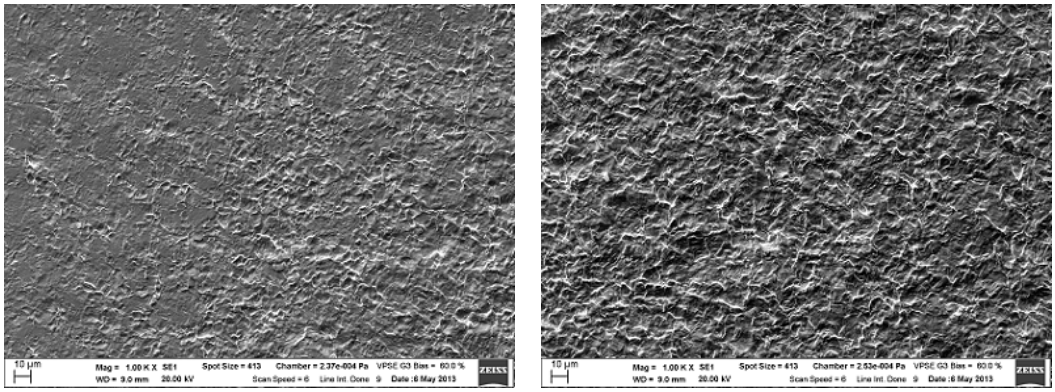

Figure 6.6: Surface morphology from SEM imaging after 1000 pulses and plasma at $F_{HF} = 15.0$ MJ m^{-2} $s^{-1/2}$ and $T_{base} = 300$ °C. No growth of grains and recrystallization are observed. Increased roughening from the rim towards centre (l) and a dense zone of small surface deformations (r). Strong morphology changes to the case of 100 pulses of only laser loading are notable.

laser only irradiation is obtained (fig. 6.10). By including the grain size of the samples on which melting is induced (sample 9 and 10), this temperature dependance is clearly continued for higher temperatures. Grain growth occurs at a lower heat load parameter when the plasma is present than for laser only exposure since the base temperature is elevated in the first case. Apart from this, the presence of plasma does not seems to affect growth of grains.

At low heat loads, up to 15.0 MJ m^{-2} $s^{-1/2}$ causing a temperature rise of ∼1400 °C, no deviation in grain size from the pristine case is measured after applying 1000 pulses. This observation is independent of pulse number at these loading conditions. On the contrary, for the case of laser only pulses at $F_{HF} = 37.5$ MJ m^{-2} $s^{-1/2}$, there is a strong increase in grain size with pulse number starting from the first pulse (fig. 4.16). The difference must be attributed to the higher peak temperature in the latter case of ∼2350 °C which is well above the recrystallization threshold. As the surface temperature is above this threshold for a longer duration at high pulse numbers, grain growth sustains. Summarizing, resizing of grains is a function of temperature and time (pulse number), preceded by recrystallization and found to start at temperatures >1500 °C.

The evolution of roughness with peak temperature (heat load parameter) shows a similar behaviour as is observed for grain growth, although deviation from the pristine case sets in at a lower

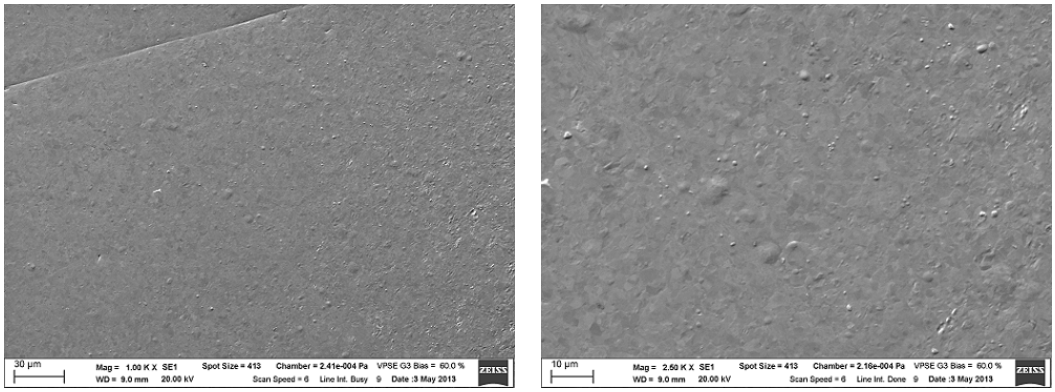

Figure 6.7: Blistering at the edge of the laser irradiated zone of II-1a at 1000X magnification (l) and 2500X magnification (r). Blisters are assumed to be created likewise at the centre of the irradiated area and are 1-5 μm in size.

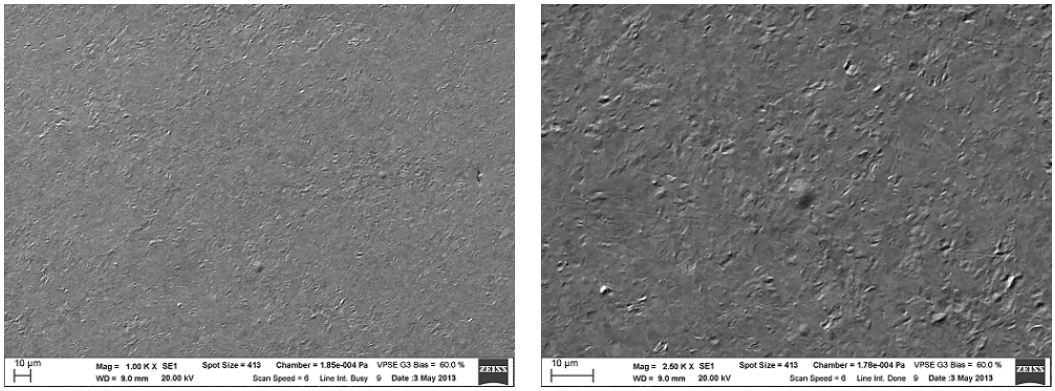

Figure 6.8: Surface morphology after 1000 pulses at $F_{HF} = 10.6$ MJ m^{-2} $s^{-1/2}$ and $T_{base} = 600$ °C (sample II-1b). The surface is only slightly roughened after loading. Some blisters are maintained upon laser loading or have been formed at the end of plasma exposure.

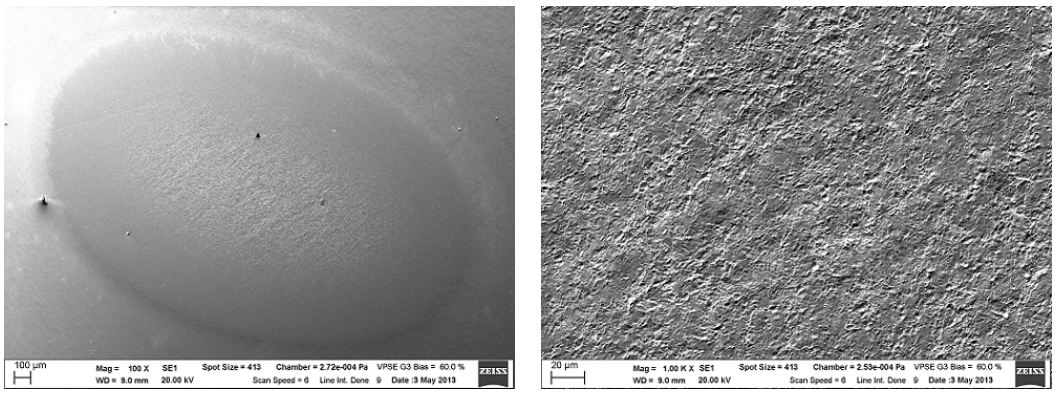

Figure 6.9: Surface morphology after 1000 pulses at $F_{HF} = 15.1$ MJ m^{-2} $s^{-1/2}$ and $T_{base} = 600$ °C (sample II-1a). Full irradiation zone (l) and 1000X magnification of roughened centre (r). No grain growth and recrystallization are measured. Blisters are not detected in the roughened irradiation zone after loading but still visible at the rim. Therefore, blisters in the centre are assumed to be disappeared due to laser impact.

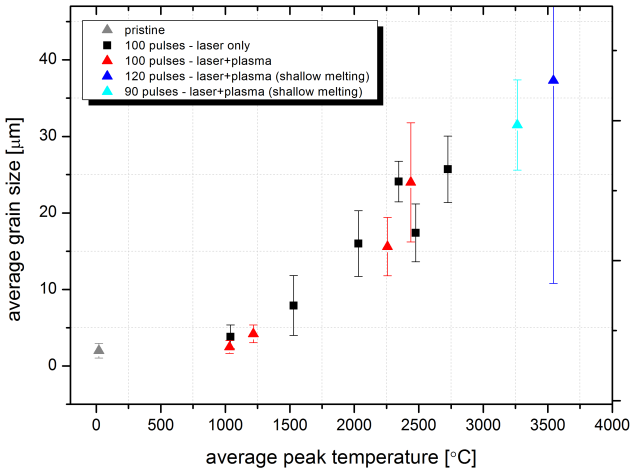

Figure 6.10: Average diameter of grains after simultaneous plasma and laser exposure shown in combination with laser only loading for about 100 pulses. For this number of pulses, grains grow linearly with peak temperature for transients >1500 °C. The average grain size after applying 1000 pulses is not shown since no change in size is measured at the applied heat loads.

temperature. For transients that elevate the surface temperature >1100 °C, roughening starts to increase linearly with increasing temperature. Grain growth continuous on the re-orientation of grain boundaries for temperatures >1500 °C, depending on the duration of this elevated temperature. For strongly roughened surfaces, protruding grains that exhibit local reduced thermal conductivity can reach the melting threshold where the average surface temperature is below this, as is described in chapter 4 (fig. 4.12). A comparison of the arithmetic roughness parameter between laser only loading on a heated sample at 450 °C and laser loading combined with plasma exposure at a range of base temperatures is shown in figure 6.11 as a function of peak temperature of the transients. The data point showing roughness of ∼0.35 μm after 1000 pulses around 1200 °C is explained by an experimental failure: during the set of 1000 pulses, 200 pulses were applied after the plasma exposure which caused enhanced roughening as the base temperature was below DBTT. Taking this into account, the effect of an increase in pulse number on roughening is not found for the peak temperatures reached during the exposures to 1000 pulses which were all below 1500 °C. Furthermore, when comparing R_a of loading on a heated sample with simultaneous plasma and laser loading at equal base temperature, the latter configuration seems to be responsible for slightly higher R_a. Further experiments need to be performed on a heated sample without plasma at higher laser powers in order to make a reliable comparison with simultaneous plasma and laser exposed samples.

Samples mounted on a external heater exposed to heat loads <15 MJ m^{-2} $s^{-1/2}$ did not develop any visual damage at all and were therefore not measured by profilometry. The overall damage development, (obtained from SEM, profilometry and reflectivity measurements) as a consequence of the different loading methods including the exposure of heated samples without plasma, are compared in the next chapter.

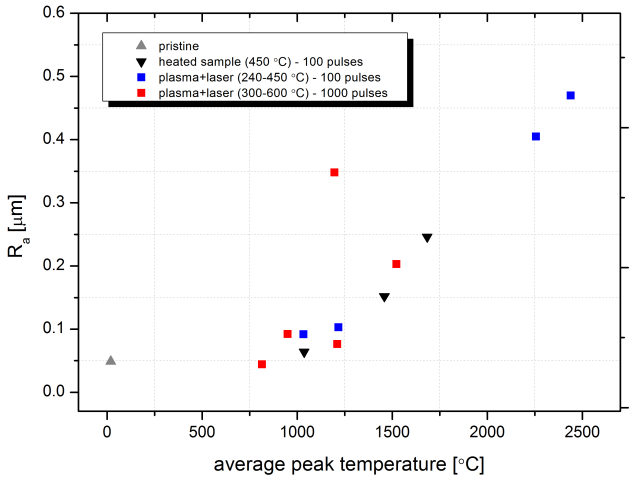

Figure 6.11: Mean roughness (R_a) of laser loaded area exposed to simultaneous plasma and 100/1000 laser pulses as a function of average peak temperature are shown together with R_a of laser only experiments on a heated sample at 450 °C. By comparing these, R_a is found to be only marginally higher as a consequence of plasma presence. Roughness starts to increase from the pristine roughness for temperatures >1100 °C.

6.2 Power handling - synergistic effects

As observed in during laser only exposures, a change in surface power handling as function of pulse number and surface temperature is also observed in some cases during experiments with simultaneous plasma presence. The fractional temperature change (average ΔT of 10 pulses normalized to the first set of 10) with the succession of pulses for a total of 100 pulses for these conditions are shown in figure 6.12. Both sample I-5 and sample I-7a reveal a fractional increase in ΔT over this range of pulses. Sample I-7a was loaded at $F_{HF} = 32.2$ MJ m^{-2} $s^{-1/2}$ where the plasma presence gave rise to an average base temperature of 240 °C, yielding an average peak temperature of 2257±79 °C. For sample I-5, loaded at $F_{HF} = 25.2$ MJ m^{-2} $s^{-1/2}$ with base temperature of 450 °C, the average peak temperature is 2438±63 °C. The average peak temperatures for sample I-6 and I-4 are respectively: 1033±21 °C and 1218±26 °C. This confirms the observation found before that peak temperatures above the recrystallization threshold seem to cause an increase in peak temperature for subsequent pulses.

Like in the case of laser only, ellipsometry measurements have been carried out on the samples exposed to 100 pulses (stated in table 6.1) in order to quantify the change in absorptivity for a damaged surface relative to the pristine case for light at a wavelength of 1064 nm. The relative change in absorptivity was measured to be 3% maximum in the case of sample I-5. The change in absorptivity compared to the pristine state is negligible in all other cases. The heat load parameter scales linearly with ΔT and hence likewise with absorptivity of the laser light (eq. 2.2). Correcting the increase in ΔT for increased absorptivity in the run of 100 pulses at $F_{HF} = 25.2$ MJ m^{-2} $s^{-1/2}$ still yields a fractional increase of ∼7%. This is comparable to 5% increase in ΔT for the high heat load exposure of the target at a base temperature of 240 °C. Regarding the small value found for the change in absorption upon simultaneous plasma and laser loading, the increase in fractional temperature of sample I-7a and I-5 (fig. 6.12) is attributed to a progressing deterioration of power handling capabilities of the surface during exposure. For the case of laser only loading, a fractional temperature increase after correcting for increased absorptivity is only found for $F_{HF} > 36.2$ MJ m^{-2} $s^{-1/2}$.

The hypothesis that a reduction of power handling sets in at lower applied heat loads if the

plasma is present compared to the case of laser only, is further strengthened by analyzing the change in ΔT for exposures on the heated sample. The sample exposed to pulses at $F_{HF} = 26.5$ MJ m^{-2} $s^{-1/2}$ whilst externally heated does not show an increase in ΔT with progressing pulses although the measured peak temperatures are within the recrystallization regime: ∼1700 °C. No notable change in ΔT connected with pulse number is found for other exposures performed on heated samples without plasma. These observation are in agreement with the results from laser only experiments for comparable heat loads at room temperature (fig. 4.19).

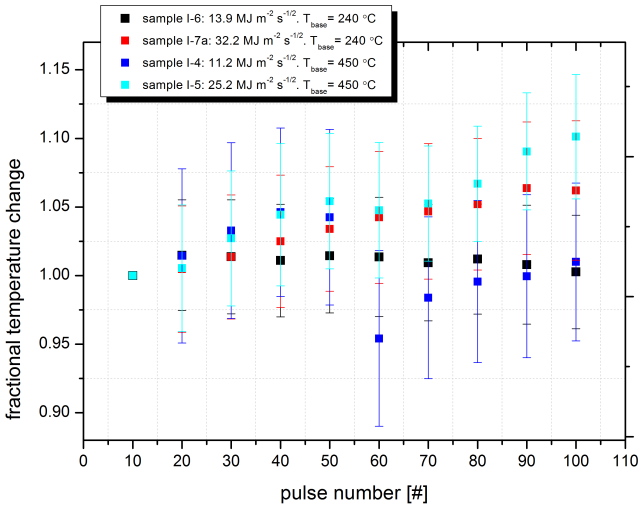

Figure 6.12: Fractional increase of ΔT over 100 pulses for a range of heat loads during simultaneous plasma and laser exposure at 240 °C (black and red) and at 450 °C (blue and cyan). A relative change in laser light absorptivity due to roughening of 3% is found in the case of I-5. No change in absorptivity is measured for other loading locations. Therefore, power handling is affected for samples I-5 and I-7a with the succession of pulses and increasing plasma fluence.

The same analysis on transient peak temperatures is performed for 1000 pulses and a maximum heat load parameter of 15.1 MJ m^{-2} $s^{-1/2}$ (fig. 6.13). As can be seen, applying pulses of $F_{HF} =$ 15.1 MJ m^{-2} $s^{-1/2}$ in combination with the plasma leads after approximately 300 pulses to a rising ΔT with the succession of pulses. It is interesting to see that deviation of the initial ΔT takes place after this number of pulses and that it is constant during the first 100 pulses. This is in line with the unchanged ΔT of loading 100 pulses at a comparable heat load of $F_{HF} = 13.9$ MJ m^{-2} $s^{-1/2}$ and lower base temperature of 240 °C (fig. 6.12), as previously discussed. During the first 300 pulses at $F_{HF} = 15.1$ MJ m^{-2} $s^{-1/2}$, the average peak temperature increases gradually 1400-1500 °C, just at the recrystallization threshold. An increase up to 1800 °C is observed in the remaining 700 pulses. A connection between the increased surface temperature and recrystallization is expected, although grain growth is absent. The peak temperature is apparently too low to generate significant resizing of grains. Furthermore, the arithmetic roughness parameter of II-1a is 0.203 μm whereas sample II-2a (black points in fig. 6.13) exhibits $R_a = 0.348$ μm. Since the latter shows no change in ΔT for the range of 1000 pulses while exhibiting a higher R_a, it is likely to assume that a possible change in absorptivity due to surface roughening is small. As is said before, the surface of II-1a is heated up to 600 °C at the laser spot position and blisters are created (fig. 6.7). As no recrystallization or grain growth is observed for the samples loaded to 1000 pulses and plasma, it is expected that the fractional temperature increase is at least partly to be explained by a synergistic effect between the impacting plasma particles and the pulsed laser. A surface temperature of 1700 °C was measured on the heated sample exposed to 100 pulses at $F_{HF} = 26.5$ MJ m^{-2} $s^{-1/2}$ without plasma and ΔT was found constant. Meanwhile, during high flux plasma exposure, the formation of bubbles

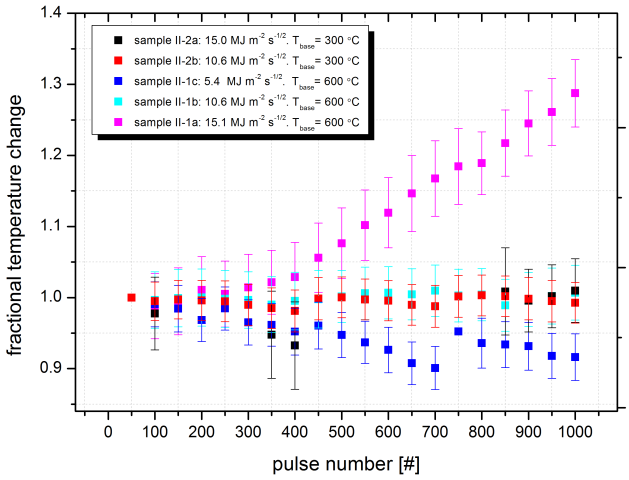

Figure 6.13: Fractional change of ΔT over 1000 pulses for a range of heat loads during simultaneous plasma and laser exposures. The hydrogen fluence increases with progressing pulse number. Base temperature was 300 °C and 600 °C during exposure.

of pressurized gas in the near surface is known to occur down to 30 nm. As the penetration depth of the laser is in this regime, it is likely that such effects lead to a change in thermal properties. Furthermore, the presence of gas in the near surface might affect thermal conductivity between adjacent grains, leading to an increase of surface temperature upon laser loading with increasing fluence.

6.3 Conclusions and discussion

Simultaneous loading of millisecond laser pulses and high flux hydrogen plasma gives rise to a lowered threshold for melting to occur at the surface, compared to the exposure of plasma and laser sequentially. The main difference is the elevated base temperature (240-600 °C) as a consequence of plasma exposure on which the transients are imposed, leading to a higher peak temperature and consequently melting at rather low heat fluxes >25 MJ m^{-2} $s^{-1/2}$ at $T_{base} = 450$ °C and >32.2 MJ m^{-2} $s^{-1/2}$ at $T_{base} = 240$ °C. On top of this, the size of the melted area was found to be higher in the case of simultaneous plasma presence compared to the case of laser irradiation only. This effect is explained by both an increase in cool-down time and ΔT with pulse number if the plasma is present.

As opposed to loading on pristine and pre-exposed samples which are all executed at room temperature, no cracking is observed in any of the simultaneous experiments were similar loading conditions were applied (tab. 6.1). This observation is explained by the fact that all samples were above DBTT during loading allowing for ductile response to swelling and cool-down of the top surface.

The formation of blisters is observed for targets exposed at 600 °C during simultaneous laser and plasma loading. Blisters are maintained upon loading of 1000 pulses at $F_{HF} = 10.6$ MJ m^{-2} $s^{-1/2}$ but not discernable after loading at $F_{HF} = 15.1$ MJ m^{-2} $s^{-1/2}$ due to intense surface roughening. Since the plasma exposure conditions were similar for the latter case, blisters are assumed to have been formed likewise. The higher applied heat load might have caused burst blisters. SEM images of higher magnification are to be made in order to confirm this statement.

Grain growth is found to increase linearly with transient peak temperature >1500 °C (fig. 6.10), as in the case of laser only loading. No recrystallization and grain growth is found for the

conditions related to 1000 pulse exposures, since peak temperatures (<1500 °C) are below the recrystallization threshold. In this temperature regime, no dependance between pulse number and grain growth is found.

The arithmetic roughness parameter (R_a) is found to increase linearly with transient peak temperature in the range 1100-2500 °C. The onset of increased roughness is just below the recrystallization threshold. Moreover, a small additional increase in roughness as a consequence of synergistic effects between the laser pulses and high-flux plasma is revealed by comparing the arithmetic roughness of modified surfaces due to simultaneous plasma and laser to surface modifications of targets at equal base temperature without plasma presence. As the number of data points connected to damage on the heated sample is small, further experiments of loading at high laser power on a heated sample have to be performed in order to make a valid comparison with the experiments of simultaneous plasma and laser exposure.

Furthermore, the maximum shift in absorptivity of laser light during the course of 100 pulses is found to be 3%. Taking this into account, a fractional increase in temperature of 5% relative to the first 10 pulses is found after applying 100 pulses at $F_{HF} = 32.2$ MJ m^{-2} $s^{-1/2}$ at $T_{base} = 240$ °C. For the case of $F_{HF} = 25.2$ MJ m^{-2} $s^{-1/2}$ at 450 °C, the fractional increase is found to be 7%. This reduction in power handling capabilities with pulse number is likely to be attributed to the high peak temperature of the transients which were >2100 °C in both cases. Recrystallization and grain growth which occurs at this temperature seems to alter the thermal properties of the surface, leading to an increase in ΔT over time.

Without accounting the corrected absorptivity, a fractional increase up to 30% is found after loading 1000 pulses at 15.1 MJ m^{-2} $s^{-1/2}$ (fig. 6.13). The change in absorptivity is expected to play a marginal role here, indicating reduced local power handling capabilities, as in the case of the fractional ΔT rise after 100 pulses. Due to a rather low surface temperature of 1400 °C, modest roughening and no recrystallization and grain growth is observed at this sample. Furthermore, no change in ΔT with pulse number is found when loading a sample at $F_{HF} = 26.5$ MJ m^{-2} $s^{-1/2}$ on an externally heated sample in absence of plasma at 450 °C where the peak temperature was 1700 °C. Since blister and bubble formation is observed on the plasma exposed sample, a synergistic effect is advocated to play a role in the reduction of power handling capabilities with increasing pulse number and plasma fluence.

Chapter 7

Final conclusion

ITER-like ELMs have been replicated by using a pulsed millisecond laser. Tungsten samples are loaded with pulse numbers ranging from a single pulse up to 10.000 at heat load parameters ranging 5-40 MJ m^{-2} $s^{-1/2}$. Three exposure methods have been distinguished: laser only loading, laser loading on pre-exposed targets to a deuterium- and helium plasma and ultimately simultaneous plasma and laser exposures. A reduction of the melting threshold is observed for the latter case. The occurrence of cracking depends on both pulse number and heat load parameter and is only observed after exposures performed at room temperature. By performing experiments on a heated sample in absence of plasma, changes in temperature rise per laser pulse for higher pulse numbers as a consequence of synergistic effects between the plasma and the pulsed laser has been verified. A comparison of created damage by the different loading methods is described hereafter.

7.1 Comparison of damage

Damage creation, qualitatively classified based on SEM and profilometry measurements, for all experiments in which 100 pulses have been applied is summarized in figure 7.1. As can be seen, the difference in damage between laser loaded pristine samples and samples exposed to a deuterium plasma is rather small. A sample pre-exposed to a high deuterium fluence ($\sim 4*10^{26}$ m^{-2}) cracked after applying 100 pulses at 28.2 MJ m^{-2} $s^{-1/2}$, as described in the work of B. Hensen. This contrasts to laser irradiated pristine samples where no cracking is found. Likewise, the onset of melting is lowered for D-exposed samples which occurred at $F_{HF} =$ 28.2 MJ m^{-2} $s^{-1/2}$ versus 36.2 MJ m^{-2} $s^{-1/2}$ of pristine samples.

Helium pre-exposed samples, containing a surface which is heavily modified due to near-surface bubble formation, were also prone to develop roughness to a greater extent than pristine samples for similar loading conditions. The nanofuzz present is largely maintained after laser loading and causes enhanced absorptivity which leads to increased damage. Applying a large number of pulses (10.000) at moderate power density leads to the formation of a dense crack network, as opposed to a few large cracks in the case of 1000 pulses on a pristine sample at $F_{HF} =$ 37.5 MJ m^{-2} $s^{-1/2}$. The resemblance between the crack network of the helium pre-exposed samples and crack networks observed after electron beam loading [6] is notable.

Besides, one of the main findings when comparing simultaneous exposure conditions of plasma and laser to these sequentially is that the threshold of W melting is reduced. This is for instance observed after 100 pulses at heat loads >25.2 MJ m^{-2} $s^{-1/2}$. Since the base temperature is elevated during plasma exposure, the transient peak temperature is equally higher. Apart from this, the plasma presence during laser loading has an additional effect on damage creation as observed when comparing these results with the damage of loaded samples that are externally heated in absence of plasma. For $T_{base} =$ 450 °C and $F_{HF} \approx$ 25 MJ m^{-2} $s^{-1/2}$, targets exposed to laser and plasma simultaneously suffered from melting where only roughening occurred for heated targets. Likewise, applying pulses at heat loads of ~10 MJ m^{-2} $s^{-1/2}$ at $T_{base} =$ 450 °C led to

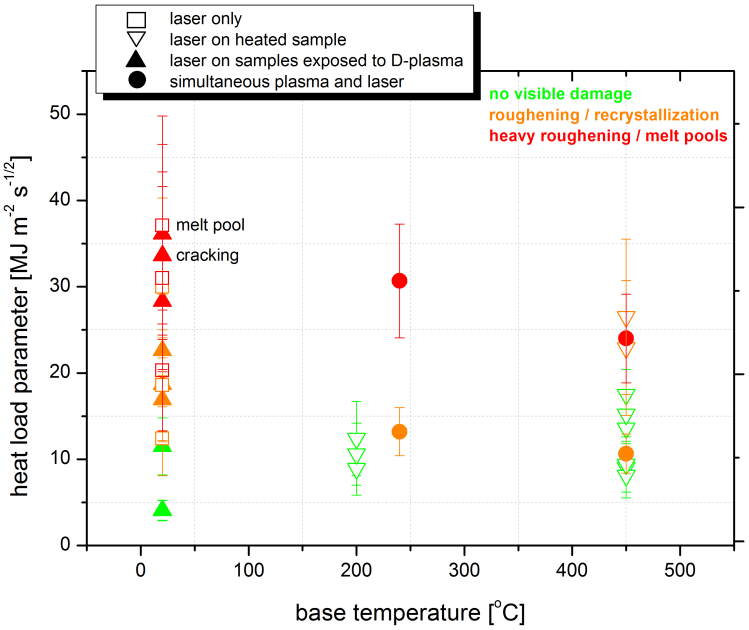

Figure 7.1: Qualitative classification of damage for all loading methods described in this thesis. Data points in red indicate severe roughened surfaces accompanied by melting of a few grains up to a contiguous melt pool and the formation of cracks. Surfaces that show pronounced modifications from the pristine case, such as recrystallization and grain growth, are depicted in orange. Data points in green indicate absence of any surface modifications up to very marginal roughening.

a strongly modified surface due to combined plasma and laser where experiments on the heater caused negligible surface modifications. In addition to the observation that the necessary ELM energy density to reach melting is reduced if a plasma is present simultaneously, the size of the melted area was found to be roughly a factor 5 larger in the case of plasma presence compared to laser only irradiation if peak temperatures of the first pulses are similar in both cases.

Both grain growth and the occurrence of surface roughness was found to develop linearly proportional with peak temperature of the applied transients. Recrystallization and resizing of grains occurs for temperatures >1500 °C whereas roughness deviates from pristine roughness at temperatures >1100 °C. The observations are similar for each loading method as is shown in figure 7.2.

Simultaneous plasma and laser exposures at high base temperatures (1560-1940 °C) led to the formation of a shallow melt layer of 30-45 μm thickness (Appendix). As a consequence, recrystallization and grain growth extended down to 330 μm, hereby affecting the heat removal capabilities of the surface and was found to increase in proportion to pulse number as inferred from cross-section SEM images. The cool-down duration was found to increase with pulse number for targets subjected to ELM-induced melting experiments. The melted zone is slightly depressed in the centre, hereby pushing melted material outside. No splashing or droplet ejection is observed.

Summarizing, regarding the absence of cracking, ELM (laser) loading in presence of plasma is found beneficial compared to plasma exposure and laser loading performed sequentially. On the other hand, a reduction in transient power density to achieve melting of W as in the case of plasma presence, leads to increased risk of embrittlement and reduced power handling capabilities with the succession of pulses. On top of this, the occurrence of synergistic effects between the plasma and laser pulses, causing a significant rise in transient temperature per laser pulse, are responsible for an additional damage effect which is not present in sequential experiments.

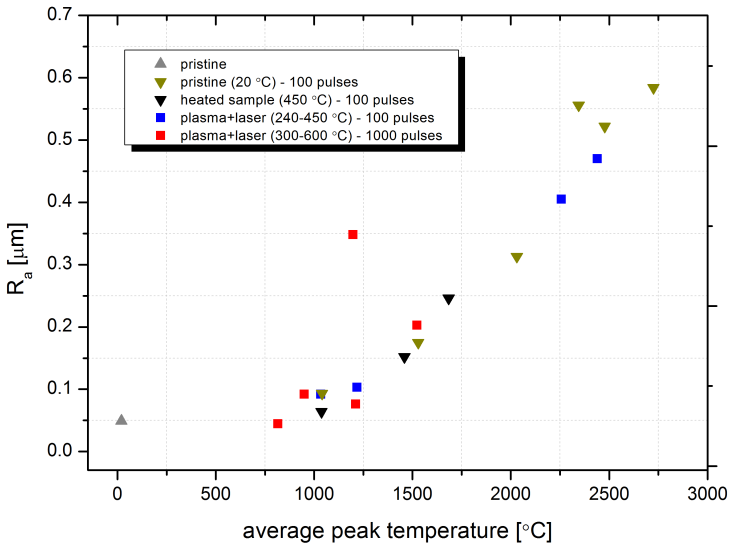

Figure 7.2: The arithmetic roughness parameter (R_a) as function of peak temperature averaged over 100 pulses for each exposure method. Roughness is found to increase linearly with temperature >1100 °C. The presence of plasma does not have a strong effect.

7.2 Implications for ITER

In the early stage of ITER operation, it is crucial to demonstrate a low-density plasma start-up with control of transients such as ELMs and disruption in a satisfactory way. After many debates, it is decided that ITER will be equipped with a full-W divertor from the start. During this phase, the highest heat loads entering the divertor will be striking the the monoblocks of the lower part of the vertical targets. Especially during nuclear phase of ITER, ensuring substantial lifetime of tungsten PFCs is essential for the successful operation of the machine. From a report concerning the status and physics basis of the ITER divertor published in 2009, it was stated that transient loads, neither uncontrolled ELMs nor major disruptions were expected to deposit sufficient energy density at lower current to cause W melting. Next to this, only slow downward vertical displacements events (VDEs) impacting the W baffle are expected to provoke melting [27]. Despite these rather positive expectations, the exact heat loads, frequency and number of repetitive heat loads in ITER are highly uncertain at this point.

From ELM-simulation studies with a pulsed millisecond laser as described in this thesis, a number of possible dangers can be pointed out. It is assumed that cracking of PFCs is hazardous to a lesser extent than melting, as cracks perpendicular to the surface are still capable of guiding heat to the underlying cooling structure whereas the thermal transfer capabilities of a melted surface are greatly reduced. Whether cracking is preceded by melting or not is depending on the grade and fabrication history of the metal. From experimental findings presented in this thesis focused on rolled polycrystalline tungsten (different from the ITER-grade), crack formation is preceded by melting in all cases. Melting leads to strong grain growth after resolidification causing increased embrittlement on its turn. On the other hand, on targets where the onset of melting is observed (F_{HF} >25.2 MJ m^{-2} $s^{-1/2}$ at $T_{base} = 450$ °C), heat transfer capabilities of the surface, measured by the time for the surface to cool down, are found unchanged. This parameter is found to increase only for pulse numbers >1000 and F_{HF} >37.5 MJ m^{-2} $s^{-1/2}$, where melting was accompanied by crack formation and in the case of ELM-induced melting at $T_{base} > 1500$ °C. Due to pre-heating above DBTT, easily reached by steady-state plasma exposure, major crack

formation is avoided for 1000 pulses up to $F_{HF} = 15.1$ MJ m^{-2} $s^{-1/2}$ whereas fatigue cracks resulting from numerous repetitive loads are observed for similar power densities and 10.000 pulses on He plasma pre-exposed targets at room temperature. However, it is expected that applying heat loads >32.2 MJ m^{-2} $s^{-1/2}$ for pulse numbers >100 will lead to the occurrence of microcracks, even at temperatures above DBTT. This is hazardous if efficient transport of heat of the PFC to its cooling structure is impeded.

As the maximum divertor PFC temperature during steady-state operation of ITER is predicted to be ∼800 °C [28], the tolerable power density of transients is limited in view of surface modifications that increase with temperatures >1100 °C as described in this thesis. As significant development of roughness starts at this temperature while being accompanied by grain growth for temperatures >1500 °C, the transient surface temperature rise at the PFC should preferably be limited to 300 °C. On top of this, as a consequence of the surface modifications that occurred on the tungsten grade under investigation here, reduction in power handling with the succession of pulses is found for peak temperatures >2000 °C. The maximum temperature rise at the PFC due to ELM impact is therefore limited to 1200 °C which is still within reach for predicted ELMs in ITER. Hence, controlling power density of transients is indispensable for stable operation in the long run.

Furthermore, during the D-T phase of ITER, interaction of W with helium could lead to bubble formation due to diffusion of helium in the target material. When a thick layer of He-induced W is present, increased peak surface temperature along with increased roughening with the succession of ELM number is found. Next to this, complete removal of the helium fuzz upon laser loading occurred only for heat loads >37.5 MJ m^{-2} $s^{-1/2}$. Although real ELMs which containing a high particle flux might have a different effect on the removal rate, minimizing the growth of a He-induced surface is most beneficial. Helium retention and migration by controlling the PFC base temperature is therefore of importance.

Apart from the issues mentioned before, a reduction of W power handling capabilities with progressing ELM number for certain conditions as discovered in experiments described in this thesis is problematic since it makes predictions of the PFC lifetime more complicated. It is found that transient temperatures >1500 °C cause significant surface modifications such as recrystallization and grain growth which affect power handling, even after applying a single ms pulse. A reduction in power handling capability of targets at room temperature is observed when applying pulses of heat loads >35 MJ m^{-2} $s^{-1/2}$. During plasma exposure of targets at an elevated temperature of 650 °C, this is effect is observed for pulse numbers >300 at $F_{HF} = 15.1$ MJ m^{-2} $s^{-1/2}$ where the transient peak temperature increases 1400-1800 °C. A gradual increase is acceptable as long as the PFC is not irreversibly damaged. As ELMs in ITER will be imposed on the steady state heat load striking the divertor, synergistic effects between surface modification from plasma exposure at high fluences and transient events are expected. Results as described in this thesis point in the direction of this intricate interplay as an additional source for damage of PFCs, but making actual predictions of this for ITER is complex as it is heavily dependent on the exact divertor environment.

Chapter 8

Outlook

As damage effects of polycrystalline rolled tungsten targets were mapped out under several laser loading configurations, comparing this to other tungsten grades and alloys in order to find the best candidate would be of interest. Some other suggestions for further research are discussed hereafter.

8.1 Change of decay time

A central observation during the performed experimental work was the spread in cool-down times (τ), defined as the time it takes before the surface temperature decays to 37 % of its peak temperature, between the different loading methods. The cool-down time was found to increase roughly a factor 2 when the plasma was present. In case of an externally heated sample, the effect was even larger. These observations were confirmed by ANSYS analysis. As the simulations in ANSYS did not take any particle flux into account but only a heat flux, the change in decay times was attributed to a change in temperature gradient at the location of the laser spot hereby affecting the cool-down time.

If control of the local temperature gradient for the total duration of laser loading can be ensured, measuring changes in τ with progressing pulse number could serve as a tool to asses the rate of heat dissipation at the surface. This is turn, could be an indication of changes in power handling. So far, the increase in τ is only observed at a pulse number >100 and $F_{HF} = 37.5$ MJ m^{-2} $s^{-1/2}$and by ELM-induced melting experiments at very high base temperatures. It would be interesting to repeat high pulse number shots during plasma exposure at steady state to see if correlations can be found between τ and different plasma parameters.

8.2 Thermal response of low-temperature He-induced W surface

As a low-temperature high-flux He plasma is expected to modify the sub-surface of W by the creation of bubbles without creating fuzz at the top surface, thermal response to transient heat loads may be changed. As found from preliminary experiments, the transient peak temperature was found to be much higher than expected. This is an effect to be explored more extensively by future experiments.

8.3 Simultaneous He plasma and laser loading

Results of laser loading on He-induced layers are described. It would be interesting to see how the formation of the fuzz layer is affected upon simultaneous exposure to laser and helium plasma.

Results on He pre-exposed targets described in this thesis can serve as a benchmark to damage evolution and fuzz layer synthesis of simultaneous experiments.

8.4 Synergistic effects

8.4.1 Blister/bubble formation

A reduction of surface heat transfer capabilities is measured after applying a high pulse number at $F_{HF} = 15.1$ MJ m^{-2} $s^{-1/2}$ during plasma exposure. The formation of blisters have been observed just outside the centre of the laser impact. As no recrystallization and grain growth occurred at this heat load but only moderate surface roughening, blister formation seems to affect the thermal response. From the obtained SEM images, burst blisters seem apparent but the magnification is too low to conclude. It would be useful to repeat these measurements and maximize the formation of blisters during laser loading, which was not the main goal for the experiments performed so far.

8.4.2 Investigating fluence effects

As previous studies have shown that large amounts of implanted ions during high flux plasma exposure are released in each laser pulse, changing the total implanted ions between subsequent pulses is expected to change the thermal resilience of the metal. To see if the hypothesis that the creation of bubbles and blisters in the near surface of the plasma exposed sample affects the W thermal shock response, an experiment can be performed in which the fluence between subsequent laser pulses is being varied. By adjusting the repetition rate of the laser while keeping laser power and plasma settings similar, the effect of the inter-pulse plasma fluence on power handling capabilities can be investigated.

Appendix A

Shallow melting experiments

In order to study melt layer stability during transients and steady state plasma, samples at high base temperature (1560/1940 °C) were subjected to laser loading with conditions as stated in table 6.1. With each transient, the surface temperature is elevated above the melting threshold, creating a shallow molten layer. No net mass loss is found by comparing the sample weight before and after loading. Neither is splashing observed from fast imaging. In order to understand recrystallization kinetics at a high base temperature and peak temperatures above the melting point, SEM images are obtained of the surface and of a cross-section through the melted region. In the centre of the loading zone of sample 9, exposed to 120 pulses at $F_{HF} = 30.7$ MJ m^{-2} $s^{-1/2}$ and $T_{base} = 1560$ °C, an average transient surface temperature of 3550 °C is measured. This led to enlarged grains up to a maximum of 80 μm in the centre of the resolidified surface. By comparing the secondary electron image of sample 9 in figure A.1, a resolidified layer with a slight depression in the middle is visible. By comparing the size of this region with the much larger area were recrystallization and grain growth has taken place (visible in the backscattered electron image of figure A.1), it is clear that a shallow molten layer has been formed during transient loading, leading to enlarged grains after resolidification. It is interesting to see that the grains in the melted region are approximately of equal size. Outside this region, the average grain size decreases with increasing distance from the centre. As no grain growth is found outside the irradiation zone of the laser, no recrystallization by the plasma solely is observed.

By comparing the cool-down times of pulses on sample 9, a gradual increase is measured. This indicates a barrier to heat conduction at the surface is progressively created, hindering efficient heat removal. Recrystallization processes, extending to hundreds of μm, is clearly affecting thermal properties.

A cross section view of sample 9 is shown in figure A.2. Recrystallization and grain growth extends up to ∼330 μm in depth. From this picture, no clear delineation is observed between the top layer which is melted and resolidified and the recrystallization zone below. However, the top layer of grains as visible in the bottom picture of A.2 are equiaxed as opposed to deeper layers and extend to about 30 μm. From the extended 1D model, describing heat diffusion in a solid that takes into account the phase shift from solid to liquid for a finite region (eq. 2.4 and 2.5), a melt layer thickness of ∼38 μm is found for the applied laser conditions and base temperature. This calculation confirms that the equiaxed top grains are resolidified from a transiently melted surface.

In order to reach even higher surface temperatures during transients, the base temperature of sample 10 was further increased by applying a very poor thermal contact with the cooling structure. In this way, an average base temperature of 1940 °C was achieved. Pulse duration was increased to 1.5 ms and the pulse repetition rate was set to 5 Hz, causing an average transient peak temperature of ∼4000 °C. The surface morphology after being loaded to 45 pulses at $F_{HF} =$ 39.8 MJ m^{-2} $s^{-1/2}$ has similar features as in the case of sample 9 and is shown in figure A.3.

SEM images of cleaves through the loaded centre of sample 10 is presented in figure A.4. By measuring grain size as function of depth, a deviation from the pristine grain size is found extending

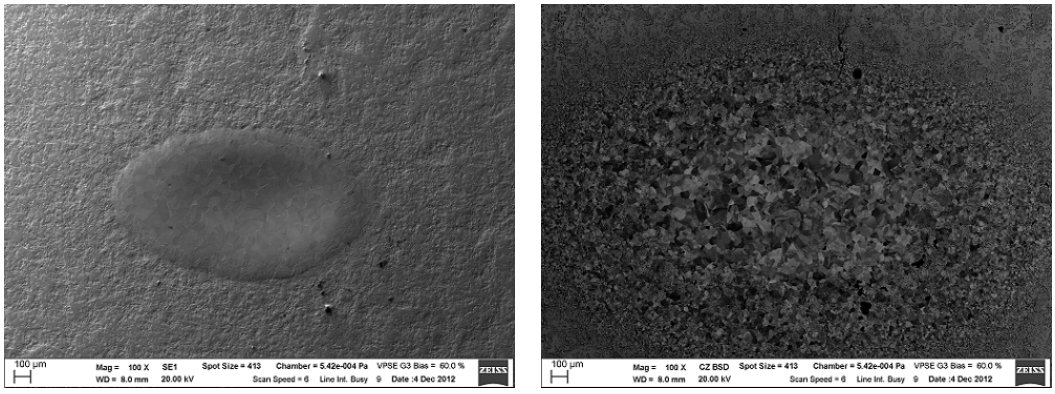

Figure A.1: sample 9, exposed to 120 pulses at $F_{HF} = 30.7$ MJ m^{-2} $s^{-1/2}$ and $T_{base} = 1560$ °C. 100X magnification of shallow melted region, depressed in the centre (l) and grain size distribution from a backscattering SEM image (r). Large grains up to 80 μm are observed in the centre. Grain growth stretches beyond central melted region.

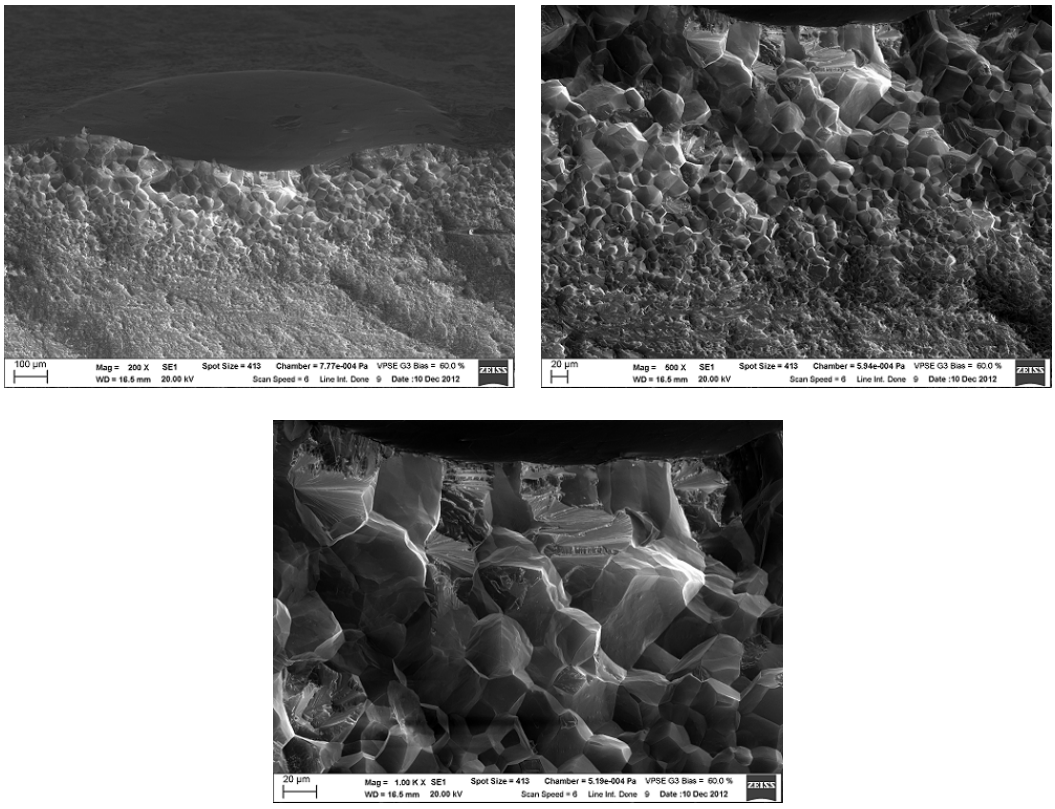

Figure A.2: SEM images of cross-section view of induced melt layer of sample 9 ($T_{base} = 1560$ °C) at 200, 500 and 1000X magnification. Grain growth extends to a depth of ∼330 μm. Equiaxed resolidified surface grains are visible in the bottom picture. The melt layer thickness is calculated to be ∼38 μm.

to a depth of 250 μm. Although this depth is smaller than in the case of sample 9, the melt layer thickness obtained from calculations (2.4) is larger: ∼45 μm. This is expected as the peak surface temperature is higher.

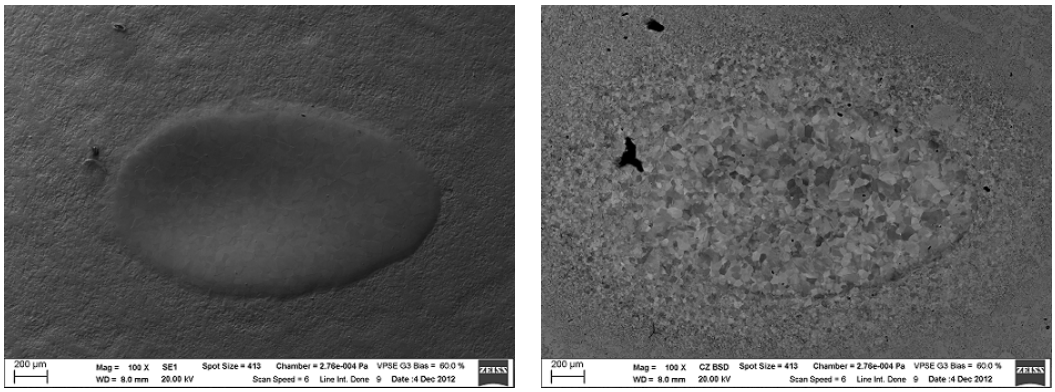

Figure A.3: sample 10, exposed to 45 pulses at $F_{HF} = 39.8$ MJ m^{-2} $s^{-1/2}$ and $T_{base} = 1940$ °C. 100X magnification of shallow melted region (l) and grain size distribution from a backscattering SEM image (r). Again, large grains up to 100 μm are observed in the centre. Beyond the resolidified centre, grain size decreases with distance from centre.

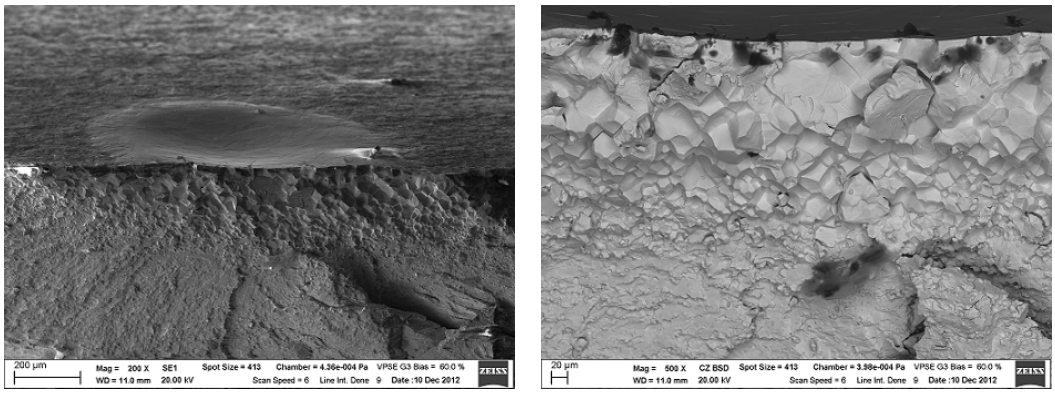

Figure A.4: SEM images of cross-section view of induced melt layer of sample 10 ($T_{base} = 1940$ °C) at 200 and 500X magnification. Grain growth extends to a depth of ∼200 μm. The melt layer thickness is calculated to be ∼45 μm.

Grain size as function of depth for both samples 9 and 10 is shown in figure A.5. In both cases, the melting depth is much smaller than the recrystallization depth. It is clear that the depth of recrystallization proceeds as a function of pulse number. However, the gradient is larger for higher pulse power density (and peak surface temperature). As no grain growth is found outside the loaded area, it is assumed that no recrystallization has taken place due to plasma exposure despite the base temperature of sample 10 being above the recrystallization threshold.

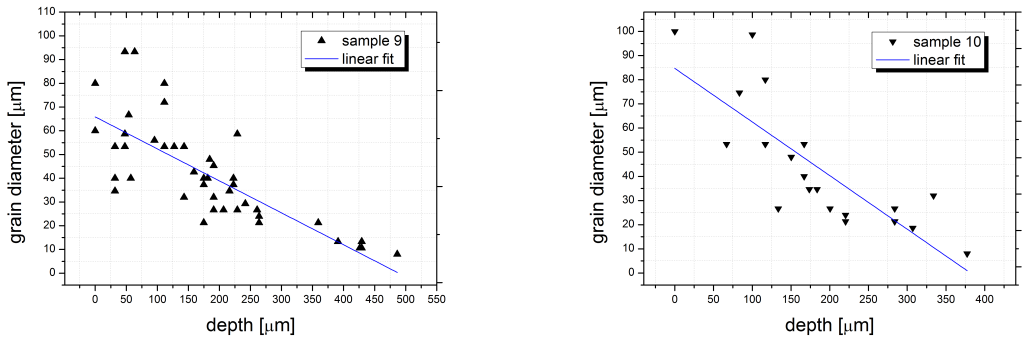

Figure A.5: Average grain diameter as function of depth at the centre of the exposed region for sample 9 exposed to 120 pulses (l) and sample 10 exposed to 45 pulses (r). The dept of resizing of grains proceeds with pulse number. Near surface grain size increases with increased power density.

Bibliography

[1] "facts and figures". In: *ITER.org* ().

[2] G. Pintsuk. "Tungsten as a Plasma-Facing Material". In: *Elsevier Ltd.* (2012), pp. 552–576.

[3] K. Itami J. Lingertat A. Loarte T. H. Osborne W. Suttrop A. W. Leonard A. Herrmann. "The impact of ELMs on the ITER divertor". In: *Journal of Nuclear Materials* 266-269 (1999).

[4] R. Sartori G. Janeschitz Y. Igitkhanov A. Kukushkin M. Sugihara D. Coster A. Herrmann L. Horten J. Stober N. Asakura K. Itami H. Tamai G. Matthews R. Schneider D. Reiter A. Leonard G. Porter A. Loarte G. Saibene. "Predicted ELM Energy Loss and Power Handling in ITER-FEAT". In: *International Atomic Energy Agency* ().

[5] R. Sartori V. Riccardo P. Andrew J. Paley W. Fundamenski T. Eich A. Herrmann G. Pautasso A. Kirk G. Counsell G. Federici G. Strohmayer D. Whyte A. Leonard R. A. Pitts I. Landman B. Bazylev S. Pestchanyi A. Loarte G. Saibene. "Transient heat loads in current fusion experiments, extrapolation to ITER and consequences for its operation". In: *Physica Scripta* T128 (2007), pp. 222–228.

[6] T. W. Loewenhoff. "Combined steady state and high cycle transient heat load simulation with the electron beam facility JUDITH II." In: *PhD thesis* (2012).

[7] H. Maier et. al. "Tungsten coating for the JET ITER-like wall project". In: *Journal of nuclear materials* 363-365 (2007), pp. 1246–1250.

[8] N. Ohno S. Takamura S. Kajita D. Nishijima. "Reduction of laser power threshold for melting tungsten due to subsurface helium holes". In: *Journal of applied physics* 100 (2006).

[9] G. Tynan K. Umstadter R. Doerner. "Enhanced erosion of tungsten plasma-facing components subject to simultaneous heat pulses and deuterium plasma". In: *Journal of Nuclear Materials* 386-388 (2009), pp. 751–755.

[10] I.E. Garkusha et al. "The latest results from ELM-simulation experiments in plasma accelerators". In: *Physica scripta* T138 (2009).

[11] G. Pintsuk L. Singheiser M. Zlobinski M. Wirtz J. Linke. "Comparison of thermal shock damages induced by different simulation methods on tungsten". In: *Journal of Nuclear Materials* 438 (2013).

[12] A. Manhard J. You M. Balden S. Lindig. "Transient heat loads in current fusion experiments, extrapolation to ITER and consequences for its operation". In: *Journal of nuclear materials* 414 (2011), pp. 69–72.

[13] D. Nishijima S. Kajita S. Takamura N. Ohno. "Formation of nanostrucutred tunsten with arborescent shape due to helium plasma irradiation". In: *Plasma and fusion research* 051 (2006), pp. 69–72.

[14] B. Hensen. "Effect of transient heat loads on plasma-exposed tungsten surfaces". In: *Internship report* (2012).

[15] R.P. Doerner K. Umstadter R.S. Wagner D. Mathys M. Duggelin E. Meyer L. Marot G. De Temmerman. "Synergistic effects of hydrogen plasma exposure, pulsed laser heating and temperature on rhodium surfaces". In: *Journal of nuclear matter* 432 (2013), pp. 388–394.

[16] A. Hassanein. "Prediction of material erosion and lifetime during major plasma instabilities in tokamak devices". In: *Fusion engineering and design* 60 (2002), pp. 527–546.

[17] E. Lassner and W. D. Schubert. "Tungsten *Properties, Chemistry, Technology of the Element, Alloys, and Chemical Compounds*". In: (1999).

[18] R. Duwe A. Lodato H.-J. Penkalla M. Roedig K. Schoepflin J. Linke M. Akiba. "Material degradation and particle formation under transient hermal loads". In: *Journal of Nuclear Materials* 1102-1106 (2001).

[19] E. D. Palik. "Handbook of Optical Constants of Solids, Volumes I, II and III". In: *Elsevier Science, & Tech* (1985), p. 804.

[20] H. S. Carslaw and J.C. Jaeger. *Conduction of Heat in Solids*. Oxford Science Publications.

[21] A. Huber. "Investigation of the Impact on Tungsten of Transient Heat Loads induced by Laser Irradiation, Electron Beams and Plasma Guns". In: *Presentation during 3rd International Workshop on Plasma Material Interaction Facilities for Fusion (PMIF 2012), Tsukuba, Japan* (2012).

[22] "SEM specifications - IPP Czech republic". In: (). URL: `ipp.cas.cz/Mi/params`.

[23] M. Zlobinski. "Laserinduzierte Desorption an plasmaerzeugten Wandbeschichtungen". In: *Diplomarbeit* (2009).

[24] T. de Kruif. "ELM transient replication using pulsed plasmas in Magnum-PSI". In: *Master thesis* (2013).

[25] N. Ohno D. Nishijima H. Iwakiri N. Yoshida S. Kajita S. Takamura. "Sub-ms laser pulse irradiation on tungsten target damaged by exposure to helium plasma". In: *Nuclear Fusion* 47.1359-1366 (2007).

[26] J. Zielinski M. Balden G. Matern C. Arnas L. Marot G. De Temmerman K. Bystrov. "Nanostructuring of molybdenum and tungsten surfaces by low-energy helium ions". In: *Journal of Vacuum Science and Technology* A 30(4) (2012).

[27] A. Loarte A. Martin M. Merola C. E. Kessel V. Komarov M. Shimada R. A. Pitts A. Kukushkin. "Status and physics basis of the ITER divertor". In: *Physica Scripta* T138 (2009).

[28] R. P. Doerner A. Hassanein R. Nygren T. D. Rognlien D. Whyte J. N. Brooks J. P. Allain. "Plasma Surface Interactions Issues of an All-Metal ITER". In: *UAEA 22nd Fusion Energy Conference* (2008).